

Structure-Property Relationships in Clay/Polymer Dispersions: Characterizing Bulk and Nanoscale Changes

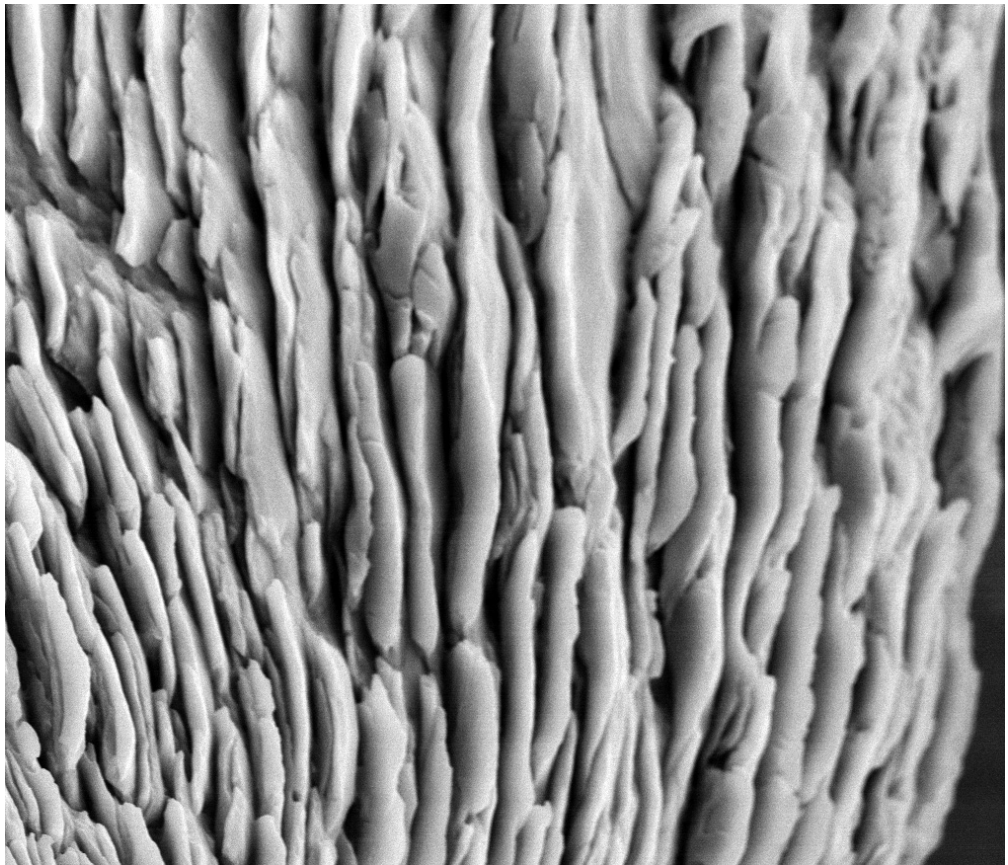
by

Kaajal Raj Juggernaut

A dissertation submitted in partial fulfillment
of the requirements for the degree of
Doctor of Philosophy
(Macromolecular Science and Engineering)
in the University of Michigan
2013

Doctoral Committee:

Professor Brian J. Love, Chair
Professor L. Jay Guo
Associate Professor Anton Van Der Ven
Professor Anthony Waas



© Kaajal Raj Juggernaut

2013

DEDICATION

To Frank Filisko, *In Memoriam*

ACKNOWLEDGEMENTS

The research contained in this dissertation could have never been completed without the guidance of my current advisor, Dr Brian Love who was willing to let me pursue this topic. His support and encouragement made the synchrotron SAXS experiments a reality. I would also like to acknowledge my committee members Professors Tony Waas, L. Jay Guo and Anton Van Der Ven for their time and availability

As I get ready to wrap this phase of my academic career, I would like to thank all those who have had a hand in making this happen. I would like to thank my first advisor, Dr Frank Filisko, who was a major influence in my early training and development as a scientist. His untimely passing changed the course of my academic career and his presence is sorely felt to this day. I would also like to acknowledge my undergraduate advisors during my time at Michigan Tech: Dr B. Pletka for taking a chance on a brand new freshman with no research experience, Dr J. Drelich, who first gave me the chance to work with an ultra-microtome and AFM as well as Dr P. Moran who broadened my horizons during my senior year. The experiences and mentorship they provided were key factors in preparing me for graduate school.

The microscopy work would not have been possible without the help and training provided by Dr John Mansfield, Dr. Kai Sun and Dr. Haiping Sun at the University of Michigan Electron Microbeam Analysis Laboratory (EMAL). Additional thanks go to Jeff Henderson at the University of Michigan Microscopy and Imaging Labs (MIL) Core facilities for his help and guidance were essential in preparing samples and conducting TEM imaging. Finally, some of the work I've done could not have been conducted without the help of Judy Poore from MIL for not batting an eye when I asked to microtome rubber samples instead of biological tissue!

Last but not least, this journey would not have been possible without the help and support of numerous friends and colleagues who have contributed in some way to the completion of this work through their support and friendship. Particular thoughts go to Norman and Kiersten in the Love group and their help during the long hours at the Beamline. Amy Gros was a great undergraduate student who contributed significantly to the study of the photorheology kinetics. Chris Moraes from the Takayama group made the lyophilization a reality. Melissa, Chris and Kyle were my hands on the rubber tire study project while Yi-Ting has been key to collagen photocrosslinking studies.

A special thanks to those who have listened to the complaining and frustration, provided insight on various projects and been willing to take coffee breaks: you know who you are! Finally, additional thanks go to Nonna Hamilton in particular for her help and encouragement over the years.

This work was made possible partially by the U.S. Department of Energy, Office of Science, Office of Basic Energy Sciences, under Contract DE-AC02-98CH10886 for work conducted at the National Synchrotron Light Source, Brookhaven National Laboratory. Steve Bennett's assistance was invaluable in setting up and running the room temperature and variable temperature experiments at Beamline X10A at Brookhaven National Labs.

Use of the Advanced Photon Source was supported by the U.S. Department of Energy, Office of Science, Office of Basic Energy Sciences, Division of Chemical Sciences, Biosciences and Geosciences, under contract No DE-AC02-06CH11357. A special thanks to Soenke Seifert for being willing to help and discuss SAXS data interpretation. I would also to acknowledge Sunsik Lee (12-BM) and Byeung doo Lee (12-ID,B) who were both helpful.

TABLE OF CONTENTS

DEDICATION	ii
ACKNOWLEDGEMENTS	iii
LIST OF FIGURES	viii
LIST OF TABLES.....	xii
CHAPTERS	
1. Introduction and Motivation	1
1.1. Introduction.....	1
1.2. Motivation and goals.....	1
1.3. Thesis scope and outline	2
1.4. References.....	4
2. Background.....	5
2.1. Dispersions and gels	5
2.2. Clay colloids	5
2.2.1. Laponite	6
2.2.2. Phases of Laponite	9
2.3. Pluronic Surfactant.....	11
2.4. Clay/polymer interactions	13
2.5. Small Angle X-ray Scattering (SAXS)	15
2.5.1. Basics of SAXS.....	15
2.5.2. SAXS experiments.....	16
2.5.3. SAXS data interpretation	16
2.6. Summary of thesis goals	20
2.7. References.....	22
3. Flow Properties of Aqueous Laponite/Pluronic F127 Dispersions	25
3.1. Chapter overview	25
3.2. Introduction.....	25
3.3. Experimental Methods	26
3.4. Results and Discussion	28
3.4.1. Dynamic Light Scattering (DLS) ²⁵	28
3.4.2. Differential Scanning Calorimetry (DSC)	29

3.4.3.	Rheology of pure Laponite dispersions	33
3.4.4.	Rheology of mixed Laponite/Pluronic F127 dispersions.....	38
3.4.5.	Microstructure in mixed dispersions.....	41
3.5.	Conclusions.....	49
3.6.	References.....	51
	APPENDIX 3-A: Images of dispersions.....	53
4.	Thermo-responsive Laponite/F127 dispersions: Gelation and structure	54
4.1.	Chapter overview	54
4.2.	Introduction.....	54
4.3.	Experimental Methods	55
4.4.	Results.....	57
4.4.1.	Variable temperature rheometry	58
4.4.2.	Structure in dispersions and gels.....	63
I.	Neat Laponite dispersions.....	63
II.	Thermo-responsive behavior of pure F127.....	64
III.	Mixed Laponite/F127 dispersions.....	67
IV.	Quantifying temperature induced changes in F127-Laponite from SAXS	70
A.	Low Laponite concentration regime (0.7wt%)	70
B.	High Laponite concentration regime (3wt%).....	77
4.5.	Conclusion	80
4.6.	References.....	82
	APPENDIX 4-A: Details of log –Boltzmann Sigmoidal mathematical fit.....	84
5.	<i>In situ</i> photogelation kinetics of Laponite nanoparticle-based photorheological dispersions	85
5.1	Chapter summary	85
5.2	Introduction.....	85
5.3	Experimental Methods	87
5.4	Results.....	89
5.4.1	Effect of composition and UV exposure on calorimetric behavior.....	89
5.4.2	Effect of solution formulation and UV intensity on gelation kinetics	93
5.4.3	Quantifying kinetics of gelation via photorheological studies.....	96
5.4.4	Photogelation mechanism, kinetics and structure	99
5.4.5	Microstructure and SAXS.....	104
5.5	Conclusion	107
5.6	References.....	109
	APPENDIX 5-A: UV intensity calibration at sample surface	111

APPENDIX 5-B: Illustration of Lorentz-corrected plots to determine structure	112
6. <i>In situ</i> time resolved UV-SAXS: Correlating bulk and nanoscale changes during photogelation	113
6.1 Chapter Summary	113
6.2 Introduction.....	113
6.3 Experimental Methods	114
6.4 Results.....	117
6.4.1 Photogelation	117
6.4.2 NMR results	118
6.4.3 Microstructure changes	121
6.4.4 Time resolved simultaneous UV-SAXS	124
6.4.5 Structural rearrangement and bulk gelation	128
6.5 Conclusions.....	134
6.6 References.....	136
7. Summary and Future Work	138
7.1. Thesis Summary.....	138
7.2. Future Directions	139

LIST OF FIGURES

Figure 2.1 Idealized crystal structure for a smectite 2:1 clay. (adapted from Kroon <i>et al.</i> ⁵)	7
Figure 2.2 Schematic of clay dispersion gel formation in water.	8
Figure 2.3 Phase diagram for Laponite dispersions from (a) Tanaka <i>et al.</i> ¹⁴ (b) Ruzicka & Zaccarelli ¹⁵	10
Figure 2.4 Schematic of possible structures in a Laponite dispersion.....	11
Figure 2.5 Commercially available Pluronic Surfactants (© BASF).....	12
Figure 2.6 Pluronic F127 phase diagram. (adapted from Wanka <i>et al.</i> ³⁹)	13
Figure 2.7 Schematic of transmission SAXS experiment with 2D data collected showing isotropic scattering.	16
Figure 2.8 Typical scattering profiles from dilute solutions with particles of different shapes from Svergun <i>et al.</i> ⁶⁰	17
Figure 2.9 Schematic of experimental structure factor curves, $S(q)$, for the gel (dashed line) and glass (solid line) structures from Tanaka <i>et al.</i> ¹⁴	19
Figure 2.10 Graphs for $S(q)$ represented at Lorentz-corrected, $I(q).q^2$ plots from Paineau <i>et al.</i>	20
Figure 3.1 Hydrodynamic radii of aqueous dispersions from dynamic light scattering (DLS).	29
Figure 3.2 Typical DSC results for F127 and F127/Laponite dispersion.	31
Figure 3.3 Results of strain sweeps at different Laponite concentrations in water.	34
Figure 3.4 Dynamic viscosity at different Laponite concentration.....	35
Figure 3.5 Frequency dependent G' for different Laponite concentrations in the LVR... ..	35
Figure 3.6 Concentration dependence of maximum G' for aqueous Laponite dispersions.	36
Figure 3.7 Frequency dependence of G'' for different Laponite concentrations.	36

Figure 3.8 Frequency dependence of complex viscosity for different Laponite concentrations.	37
Figure 3.9 Room temperature frequency response for 3wt% Laponite with added F127. 38	
Figure 3.10 Summary of solution properties of 3.6wt% F127 with 3wt% Laponite.....	40
Figure 3.11 Microstructure of 3.6wt% F127 dispersions with increasing Laponite content.	43
Figure 3.12 High magnification SEM of lyophilized samples.	44
Figure 3.13 AFM from 3.6wt% F127 + 3wt% Laponite spin coated on freshly cleaved mica.....	45
Figure 3.14 Representative TEM from drop cast samples.....	47
Figure 3.15 Representative TEM micrographs from lyophilized gels.....	48
Figure 3- A Photographs illustrating 3wt% with various F127 concentrations.....	53
Figure 4.1 SAXS setup at Brookhaven National Labs.	57
Figure 4.2 Thermo-reversible liquid to gel transition for 3.6wt% F127 with 3wt% Laponite.	58
Figure 4.3 Temperature dependent G' for 3.6wt% F127 with Laponite.	59
Figure 4.4 Effect of small Laponite additions to (a) 10wt% and (b) 25wt% F127.....	60
Figure 4.5 Room temperature SAXS plots for three different Laponite concentrations in water.....	64
Figure 4.6: Summary of concentration and temperature effects on pure F127 solutions. 66	
Figure 4.7 <i>In situ</i> temperature dependent SAXS for different Laponite/F127 dispersions.	69
Figure 4.8 Schematic of Laponite/F127 core-shell structure.....	71
Figure 4.9 Variable temperature SAXS spectra after removing 0.7wt% Laponite scattering contribution.	74
Figure 4.10 Fit results using a core-shell cylinder model.....	75
Figure 4.11 Schematic of changes in structure during thermal gel formation.....	77
Figure 4.12 Experimental structure factor in neat Laponite dispersions.	78
Figure 4.13 Temperature dependent characteristic spacing.for 3wt% Laponite with 3.6wt% F127.....	79

Figure 4- A Schematic of the log Boltmann sigmoidal model curve showing the relevant parameters.	84
Figure 5.1 Schematic of photogelation mechanism (adapted from Sun et al. ¹⁴)	87
Figure 5.2 Representative DSC thermograms.	90
Figure 5.3 Summary of <i>in-situ</i> photogelation kinetics showing changes in complex viscosity.	94
Figure 5.4 G' (open) and G'' (filled) profiles as a function of UV exposure time.....	95
Figure 5.5 Gelation rate variations as a function of composition.	98
Figure 5.6 Final viscosity of the gels with different dispersions.	100
Figure 5.7 Schematic of proposed final gel structure at high F127 concentration.	101
Figure 5.8 Schematic of resulting gel as a function of Laponite particle concentration	103
Figure 5.9 Parameter space mapping for Laponite dispersion photogelation kinetics and final viscosity (UV intensity = 150 mW/cm ²).	104
Figure 5.10 Representative SEM images of lyophilized samples.....	105
Figure 5.11 Summary of temperature dependent SAXS results before and after UV exposure	106
Figure 5.12 Representative TEM of lyophilized gel after UV exposure.	107
Figure 5- A Schematic of positions used to calibrate UV intensity to ensure uniform UV exposure on sample.....	111
Figure 5- B Scattering data from 3wt% Laponite with 3.6wt% F127 as a function of temperature.	112
Figure 5- C Lorentz corrected from scattering data before UV exposure showing change in peak.....	112
Figure 6.1 Picture of setup used for simultaneous UV-SAXS at 12-ID at the Advanced Photon Source.	116
Figure 6.2 Photogelation profiles for dispersions containing of 5mM of PAG 1, 2, and 3.	117
Figure 6.3 ¹ H-NMR aromatic region as a function of UV exposure time for 5mM PAG in D ₂ O.	120
Figure 6.4 ¹ H-NMR aliphatic and sulfur regions for 5mM PAG 2 and PAG 3 in D ₂ O.	121

Figure 6.5 SEM images of lyophilized samples with 3wt% Laponite, 3.6wt% F127 and 5mM PAG 1.....	122
Figure 6.6 SEM images obtained 3wt% Laponite, 3.6wt% F127 and 5mM PAG 2.	123
Figure 6.7 SEM images 3wt% Laponite, 3.6wt% F127 and 5mM PAG 3.	123
Figure 6.8 Time resolved SAXS for 3.6wt% F127 with 3wt% Laponite and 5mM PAG.	126
Figure 6.9 Surface plot of time resolved data showing intensity variation.	127
Figure 6.10 3D and 2D Lorentz corrected plots for time resolved UV-SAXS results. ..	129
Figure 6.11 Contour plot illustrating time dependent changes in Lorentz corrected data.	131
Figure 6.12 Time dependent variation in structural spacing and bulk complex viscosity	133

LIST OF TABLES

Table 3.1 Summary of thermodynamic properties from DSC data.	32
Table 4.1 Summary of thermal gelation and fit parameters.....	61
Table 5.1 Summary of effect of additives on thermal behavior of the dispersions.	91
Table 5.2 Summary of sigmoidal fit results for gelation kinetics as a function of sample composition.....	97
Table 5.3 Summary of sigmoidal fit for different UV exposure intensity and PAG concentrations.	97
Table 6.1 Summary of photoacid generator (PAG) compounds used in this study.....	115

CHAPTER 1

1. Introduction and Motivation

1.1. Introduction

Why does paint flow when stirred or spread but stays on a wall after application? Why does toothpaste or honey flow when deformed? How is Jell-O® made by dissolving a powder into a liquid such as water? These are all phenomena that we have seen or experienced first-hand and are the subject of on-going study.

These materials are considered complex fluids with multiple components used to impart unique properties ^{1, 2}. Additives such as colloids and polymers are often used to control the structure as well as mechanical properties in numerous applications such as cosmetics, coatings, paints, personal care products and drilling fluids to name a few ^{1, 3-9}. Such systems exhibit interesting physics as a result of not only the solution conditions and preparation methods but also the interactions between the different components present in the system ¹⁰⁻¹². A better understanding of these interactions is therefore essential but remains a challenge despite advanced characterization techniques to study these materials.

1.2. Motivation and goals

Clays ^{10,13-17} and surfactants ^{8, 18-24} are common types of materials used as additives in a wide variety of industrially relevant applications. However, in the majority of current applications, there is no active control of the transition from the liquid to the gel state. The goal of this work is thus two-fold.

First, the basic properties as well as self-assembly behavior of model aqueous dispersions containing clay only or both clay and a polymer are studied to understand the type of basic interactions and structure-property relationships present in these composite materials. Second, given that individual components within dispersions are known to impart unique properties, I show that formulations based on a simple clay/polymer system with responsive on-demand sol-gel transitions can be achieved using an external stimulus such as heat or light. Since controlled gel formation in clay dispersions has not been studied extensively, the following work addresses the ability to control gelation and basic characterization of the material systems studied here.

1.3. Thesis scope and outline

The overall scope of this thesis is to conduct a comprehensive study of a gel forming aqueous nanocomposite system and focus on understanding how the structural arrangement of colloidal nanoparticles is related to bulk changes such as gel formation. This thesis focuses on the physical interactions occurring in aqueous clay/surfactant dispersions and uses a combination of rheology, microscopy and small angle x-ray scattering to study dynamic changes and structural rearrangement.

This dissertation is organized into chapters as follows:

- **Chapter 2** presents an introduction to the materials and methods used to conduct the bulk and time resolved structural studies throughout this work.
- **Chapter 3** introduces the basic properties of aqueous solutions of Laponite clay nanoparticles used as the main focus of this study. The basic rheology of these solutions and the effect of adding an amphiphilic surfactant, Pluronic F127, are shown.
- **Chapter 4** follows with a demonstration of heat induced changes in the Laponite/F127 dispersions. The temperature dependent properties are tracked using rheology. Chapter 4 also introduces the use of small angle x-ray scattering (SAXS) as a method of probing structural changes and rearrangement in these dispersions.

- **Chapter 5** provides an introduction to light controlled gels and the application of this method to Laponite systems. The influence of concentration, stimulus and composition on gel formation as well gelation rate is addressed here.
- **Chapter 6** focuses on the characterization of structural changes during formation. In particular, we demonstrate the use of small angle x-ray scattering to characterize the Laponite system structure and present a dynamic simultaneous study of structural evolution during UV exposure. Finally, the changes in structure from SAXS studies are compared to bulk rheology measurements to determine structure-property relationships in clay gels.
- **Chapter 7** summarizes the contributions of this dissertation and provides an outlook for future developments.

1.4. References

- (1) Larson, R. G. *The structure and rheology of complex fluids*; Oxford university press, New York, **1999**; Vol. 2.
- (2) Safran, S. A. and Clark, N. A. (eds) *Physics of Complex and Supramolecular Fluids*, Wiley New York, **1987**.
- (3) Wu, C.-J.; Gaharwar, A. K.; Schexnailder, P. J.; Schmidt, G. *Materials* **2010**, *3*, 2986-3005.
- (4) Loizou, E.; Porcar, L.; Schexnailder, P.; Schmidt, G.; Butler, P. *Macromolecules* **2009**, *43*, 1041-1049.
- (5) Gaharwar, A. K.; Rivera, C. P.; Wu, C.-J.; Schmidt, G. *Acta Biomater.* **2011**, *7*, 4139-4148.
- (6) Hammond, J. S.; Holubka, J. W.; deVries, J. E.; Dickie, R. A. *Corros. Sci.* **1981**, *21*, 239-253.
- (7) Mills, J. S. *Stud. Conserv.* **1966**, 92-107.
- (8) Levitz, P. E. *Comptes Rendus Geosci.* **2002**, *334*, 665-673.
- (9) Baghdadi, H. A.; Jensen, E. C.; Easwar, N.; Bhatia, S. R. *Rheol. Acta* **2008**, *47*, 121-127.
- (10) Trizac, E.; Bocquet, L.; Agra, R.; Weis, J. J.; Aubouy, M. *J. Physics: Condens. Matter* **2002**, *14*, 9339
- (11) Belloni, L. *J. Physics: Condens. Matter* **2000**, *12*, R549
- (12) Li, L.; Harnau, L.; Rosenfeldt, S.; Ballauff, M. *Phys. Rev.* **2005**, *72*.
- (13) Avery, R. G.; Ramsay, J. D. F. *J. Colloid Interface Sci.* **1986**, *109*, 448-454.
- (14) Philippe, A. M.; Baravian, C.; Imperor-Clerc, M.; De Silva, J.; Paineau, E.; Bihannic, I.; Davidson, P.; Meneau, F.; Levitz, P.; Michot, L. *J. Physics: Condens. Matter* **2011**, *23*.
- (15) Schmidt, G.; Nakatani, A. I.; Han, C. C. *Rheol. Acta* **2002**, *41*, 45-54.
- (16) Okay, O.; Oppermann, W. *Macromolecules* **2007**, *40*, 3378-3387.
- (17) Boucenna, I.; Royon, L.; Colinart, P. *J. Therm. Anal. Calorim.* **2009**, *98*, 119-123.
- (18) Tate, M. P.; Urade, V. N.; Gaik, S. J.; Muzzillo, C. P.; Hillhouse, H. W. *Langmuir* **2009**, *26*, 4357-4367.
- (19) Auvray, L.; Ayrat, A.; Dabadie, T.; Cot, L.; Guizard, C.; Ramsay, J. D. *Faraday Discuss.* **1995**, *101*, 235-247.
- (20) Alexandridis, P.; Alan Hatton, T. *Colloids Surfaces A: Physicochem. Eng. Asp.* **1995**, *96*, 1-46.
- (21) Rafai, S.; Sarker, D.; Bergeron, V.; Meunier, J.; Bonn, D. Superspreading: Aqueous Surfactant Drops Spreading on Hydrophobic Surfaces. *Langmuir* **2002**, *18*.
- (22) Kubies, D.; Jérôme, R.; Grandjean, J. *Langmuir* **2002**, *18*.
- (23) Cui, Y.; Pizzey, C. L.; Van Duijneveldt, J. S. *Philos. Trans. R. Soc. A: Math. Phys. Eng. Sci.* **2013**, *371*.
- (24) Chaibundit, C.; Ricardo, N. M. P. S.; Ricardo, N. M. P. S.; O'Driscoll, B. M. D.; Hamley, I. W.; Yeates, S. G.; Booth, C. *Langmuir* **2009**, *25*, 13776-13783.

CHAPTER 2

2. Background

2.1. Dispersions and gels

Dispersions and gels are widely used in a variety of industrial applications. The term “dispersion” here broadly refers to a system in which particles are distributed into a continuous phase of a different composition or state ¹. Examples of commonly encountered dispersions include solid particles in a fluid such as air or water (smoke, ink and paint), liquid droplets of one type distributed in another liquid (emulsions, milk and mayonnaise) or gas bubbles in a liquid (foams and creams). Gels, typically defined as a solid that does not flow under steady state ², can be obtained from a dispersion when the concentration of the dispersed phase is high enough to achieve percolation. At these concentrations, the dispersed phase forms a network capable of bridging and effectively trapping the continuous phase. Hence, solutions (“sols”) and gels can be obtained from the same components but by adjusting the overall composition. Dispersions and dispersion formulation science are therefore particularly important for commercial applications where flow behavior and functionality are intimately related.

2.2. Clay colloids

Clay minerals are ubiquitously present layered silicate materials. In nature, clay minerals exist in a wide variety of shapes and sizes with common examples including mica, kaolinite, talc and montmorillonite. Recent advances have led to the widespread use of synthetic clay particles which provide several advantages such as well controlled chemistry and narrow particle size distributions ^{3, 4}. Throughout this work, a particular type of synthetic clay, Laponite RD®, was used (RD stands for rapid dispersion).

2.2.1. Laponite

Laponite is a commercially available synthetic hectorite clay used as a rheological modifier in a variety of commercial products including toothpastes, paints and personal care products^{3, 4}. Laponite has the structure of a 2:1 phyllosilicate with an empirical formula of $\text{Na}^{+0.7}[(\text{Si}_8\text{Mg}_{5.5}\text{Li}_{0.3})\text{O}_{20}(\text{OH})_4]^{-0.7}$. It contains a central octahedral brucite-like sheet sandwiched between two tetrahedral silicate layers. Isomorphous substitution of magnesium with lithium results in a charge imbalance on the platelet that is compensated by sodium counter-ions present at the surface of the Laponite, in the spaces between platelets. Platelets of Laponite are 25nm in diameter on average, with a thickness of about 1nm, and contain on the order of 1000 sodium counter-ions per platelet (based on a cation exchange capacity of 0.55meq per gram, as specified by the manufacturer).

On mixing Laponite with water, the counter-ions responsible for charge balance dissociate and Laponite disperses readily to form a transparent mixture. Aqueous dispersions of Laponite are known to have thixotropic properties as well as demonstrate significant changes in rheological properties with time due to aging. Figure 2.1 shows a schematic of the idealized crystal structure while Figure 2.2 depicts the formation of an aqueous Laponite dispersion and gel.

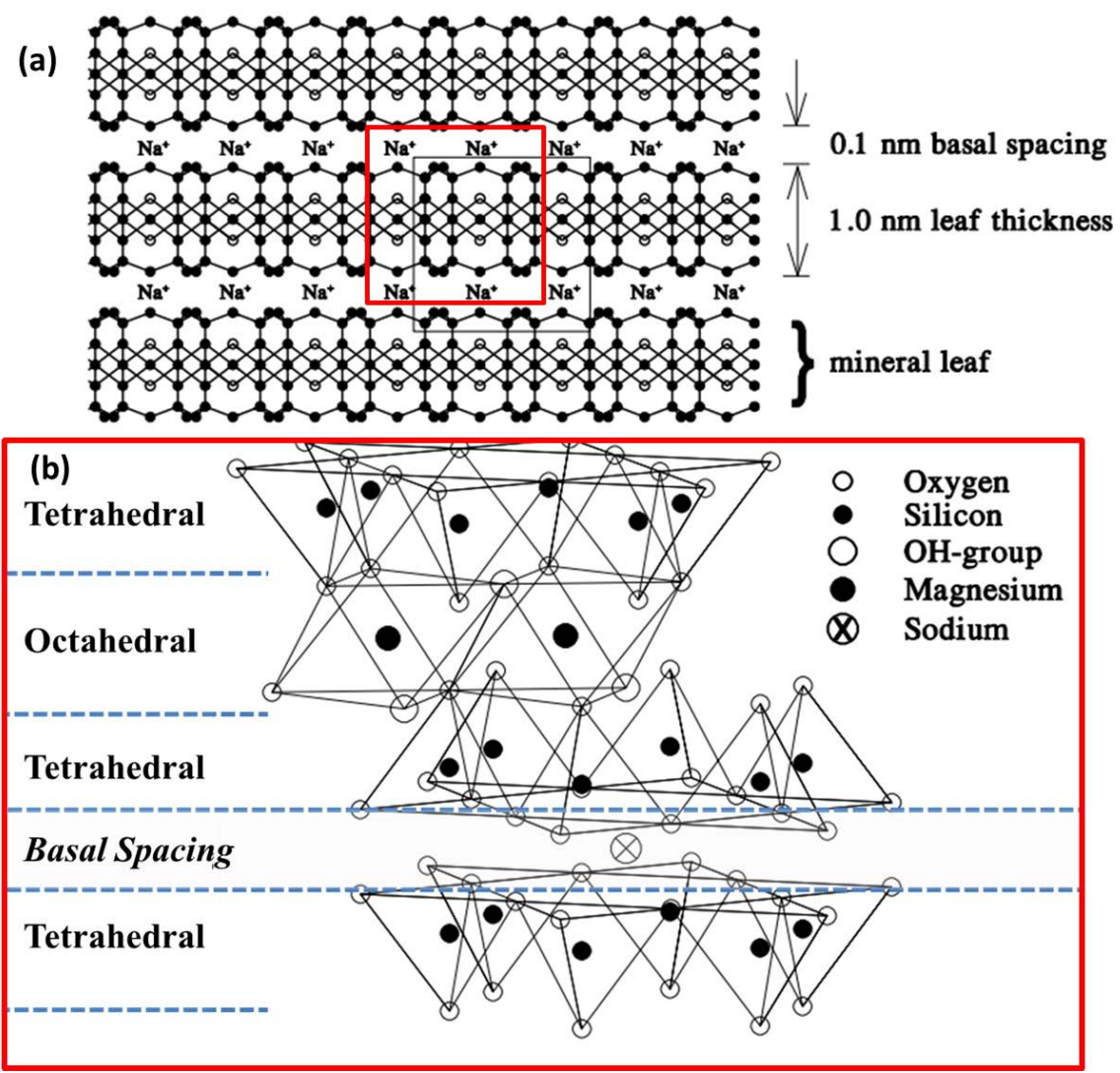


Figure 2.1 Idealized crystal structure for a smectite 2:1 clay. (adapted from Kroon *et al.* ⁵)

The arrangement of the mineral layers is depicted in (a) while (b) shows the atomic structure in each layer in the case of Laponite.

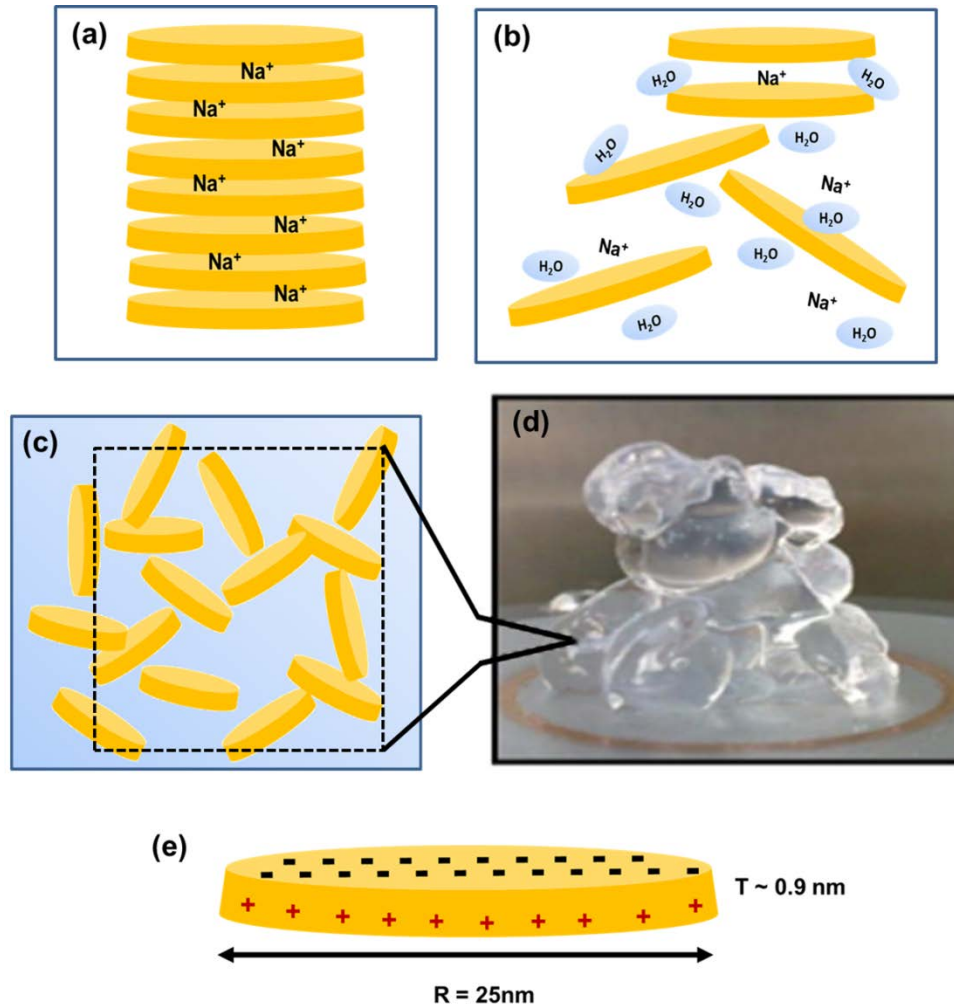


Figure 2.2 Schematic of clay dispersion gel formation in water.

Each images shows (a) schematic of dried clay discs stacked together (b) hydration of discs and dissolution of interlayer sodium cation (c) possible arrangement of exfoliated discs in water (d) photograph of a 5wt% Laponite gel in water (diameter of circle = 3cm) and (e) Schematic of an individual Laponite clay disc with 25nm diameter and 0.9nm thickness. The surface charges shown here are expected for Laponite in water at $\text{pH} < 8$.

2.2.2. Phases of Laponite

Laponite dispersions have been widely studied due to their rich physics and phase space. Pignon and coworkers showed that a connected fractal network of micron sized aggregates can be found in high ionic strength dispersions while Bonn *et al.* showed that, at pH of 10, no fractal network was evident. These dispersions have indeed been found to be sensitive to a variety of factors namely concentration, pH, ionic strength and age of dispersion^{4, 6-13}. Tanaka *et al.*¹⁴ proposed a phase diagram for aqueous Laponite dispersions as a function of concentration and ionic strength (Figure 2.3(a)) describing the possible phases of aqueous Laponite dispersions including gels and glassy isotropic networks. Recently, Ruzicka and Zacarrelli further expanded on the Laponite phase diagram by combining characterization methods and simulations from a number of studies¹⁵. The results of this are shown in Figure 2.3(b) where again the presence of gels and glassy networks was noted at high Laponite concentrations.

Here, the states of Laponite are differentiated based on the structure of the particles in the dispersion particularly in the high concentration regimes where the bulk material is a gel but the structure is that of either a glass or gel where both are disordered solid states, i.e. they do not flow under gravity and do not exhibit long range order. These are instead differentiated by their local structure. Gels typically occur at lower densities and are formed as the result of attractive interactions between the particles leading to a percolated network. Glassy structures on the other hand typically arise in dense fluids where the particles are trapped in a so-called cage effect by their nearest neighbors and cannot relax to their equilibrium state. The main difference between a glass and a gel are the characteristic length scales present: in a glass this is typically on the order of a particle size while in a gel due to the lower density, correlation lengths tend to be on the order of several particle sizes¹⁶⁻²¹.

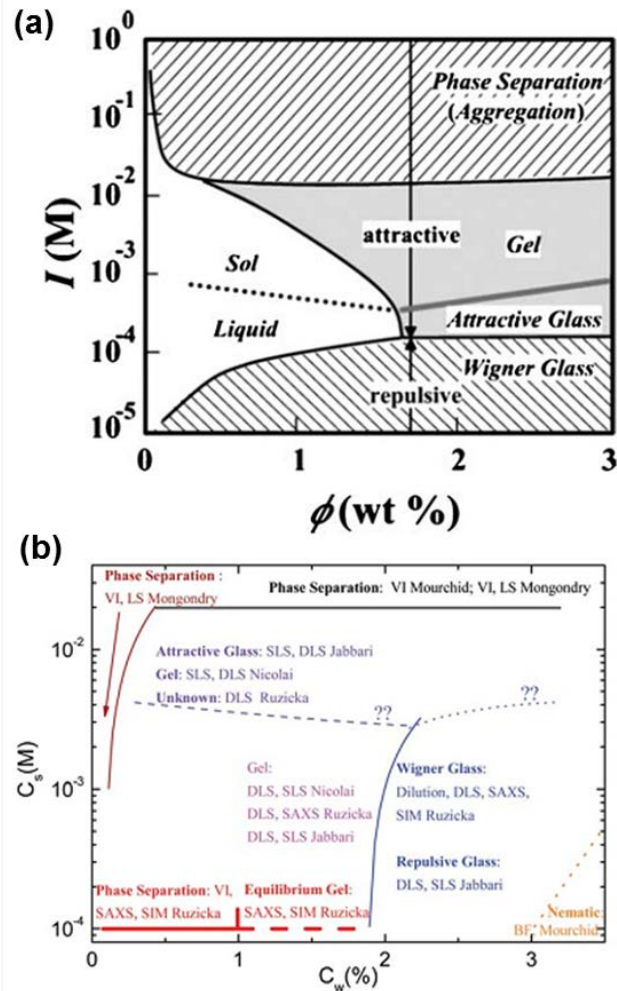


Figure 2.3 Phase diagram for Laponite dispersions from (a) Tanaka *et al.*¹⁴ (b) Ruzicka & Zaccarelli¹⁵.

It is also possible to obtain a glassy structure at low density in the absence of attractive forces. These are generally referred to as “Wigner glasses” where particles do not form a network but remain spatially disconnected as a result of electrostatic repulsions between particles preventing them from coming into contact. Typically in the glassy phase, the characteristic separation is on the order of the particle size. In the case of Laponite the existence of both gels and glassy structures has been demonstrated by various groups both experimentally and using simulations^{11, 16, 20-24}. A schematic of the typical structure of Laponite gels and glasses is shown in Figure 2.4.

Throughout this thesis, the term gel or soft solid will be used to describe the bulk state of the dispersions only and does not the particle arrangement. Since most commercial dispersions utilize Laponite combined with a number of different additives, we chose to use a commercially available surfactant, Pluronic F127, for the investigations reported here.

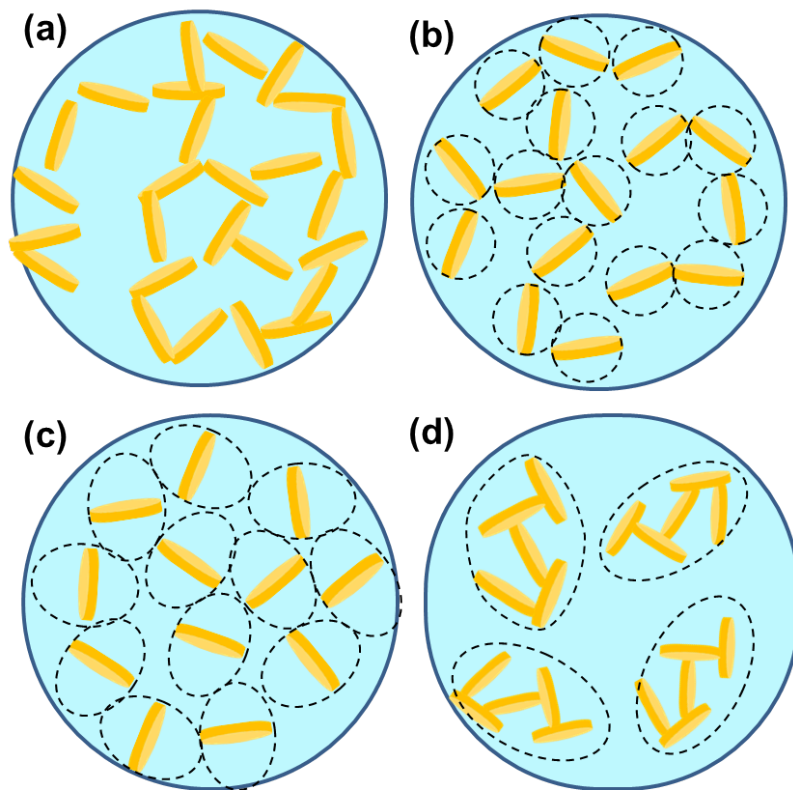


Figure 2.4 Schematic of possible structures in a Laponite dispersion.

(a) gel with percolating network of particles (b) attractive glass network (c) repulsive (Wigner) glass and (d) Wigner glass with clusters of interacting particles (Adapted from Tanaka *et al.*¹⁴). As shown here, only particles in the gel state are in direct contact with each other as attractive interactions dominated. In (b) attractive interactions affect the spatial distribution but repulsive interactions prevent the particles from coming too close to each other. In (c) and (d) repulsive electrostatic interactions dominate although (d) shows that attractive interactions can exist within individual clusters.

2.3. Pluronic Surfactant

Pluronic surfactants are commercially available amphiphilic triblock copolymers of polyethylene oxide-polypropylene oxide-polyethylene oxide (PEO-PPO-PEO). A variety of Pluronic surfactants are readily available, with differing block and arm lengths. These

can be arranged on what is known as the Pluronic grid (Figure 2.5). Pluronic surfactants are widely used in a variety of biomedical applications and as surfactants for food and personal care products^{25, 26}.

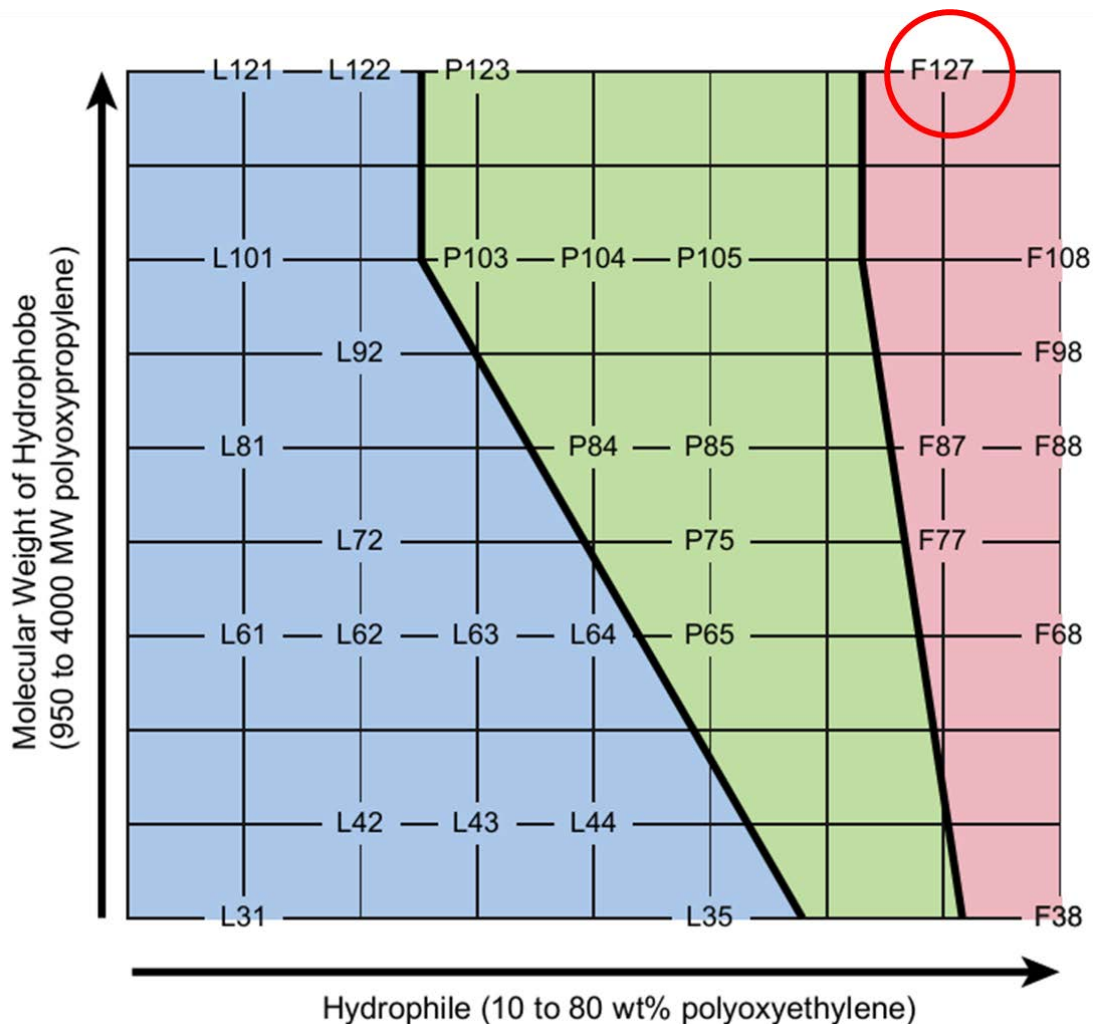


Figure 2.5 Commercially available Pluronic Surfactants (© BASF).

The first letter of each Pluronic surfactant, as well as the colors, indicate the phase of the pure surfactant at room temperature. Surfactants are liquids (L) in the blue region, pastes (P) in the green region, and solids (F) in the pink region. Pluronic F127 used in this thesis is circled.

These Pluronic surfactants are particularly interesting due to their ability to undergo a temperature dependent micellization process in aqueous solutions that, at high enough concentrations, leads to thermoreversible gel formation. Numerous studies have been conducted using a variety of techniques to determine the structure-property relationships

in these responsive gels leading to the development of various phase diagrams by several groups²⁷⁻³². Due to their widespread use with a number of additives, several studies on the changes in the solution properties have also been reported. Chaibundit *et al.*³³ demonstrated the effect of ionic surfactants such as SDS on micelle and gel formation while Meznarich *et al.*³⁴ reported on the effects of small pharmaceuticals on the thermo-physical properties of these dispersions using SAXS and rheology. Wu *et al.*³⁵ as well as Prud'Homme *et al.*³⁶ reported that high concentrations of Pluronic lead to a cubic lattice of micelles. These structures have been imaged directly with AFM and cryo-TEM^{37,38}.

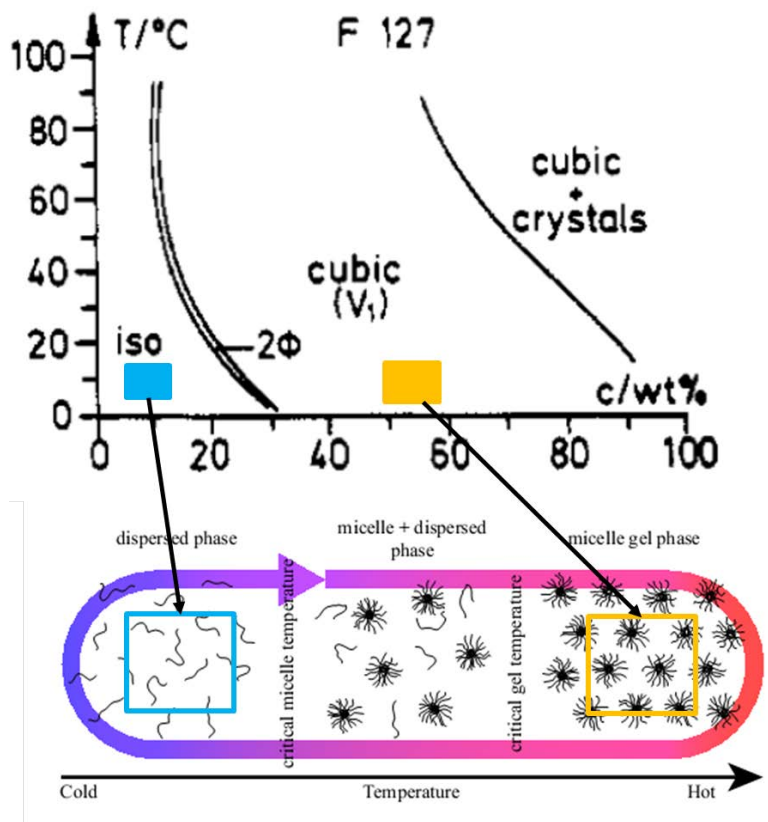


Figure 2.6 Pluronic F127 phase diagram. (adapted from Wanka *et al.*³⁹)

The schematic shows the temperature dependent transition from dispersed molecules (isotropic) to a cubic micelle gel phase.

2.4. Clay/polymer interactions

Clay incorporated with polymers has been the subject of intense study since the natural clay, montmorillonite, was used in the synthesis of a clay/nylon-6 nanocomposite by Toyota⁴⁰. Since then, the majority of the studies on clay/polymer systems have focused

on solid state nanocomposites with clays incorporated into various polymer matrices and several reports exist on property enhancements in polymer clay nanocomposites⁴¹⁻⁴⁸ and on the structural changes resulting from clay orientation^{49, 50}. Despite the commercial relevance of these materials, there exists however limited studies on the dispersions and particle/polymer or polymer/surfactant interactions in the fluid or gel states.

Several groups have recently investigated the effects of adding surfactants^{9, 51-58} on the phase diagram, gelation, aging behavior and structure of Laponite dispersions. The inter-particle interactions in dispersions of Laponite are however experimentally difficult to determine but the addition of surfactants such as poly(ethylene oxide) (PEO) has been shown to change the dynamics, structure and rheological properties of neat Laponite dispersions. Similar modification of rheological properties has also been seen with clay/surfactant systems.

A number of studies using methods such as light scattering, neutron scattering and x-ray scattering have provided some insight into the particle size and distribution in solution. Nelson and Cosgrove used contrast matched SANS to study the interactions between a surfactant such as PEO or Pluronic triblock copolymers and Laponite nanoparticles in solution^{51, 53}. Their results show that the surfactant molecules adsorb onto the Laponite surface in aqueous dispersions. At higher Laponite concentrations (2wt%), they found that repulsive interactions become more pronounced with the addition of smaller chains, most likely due to steric contributions.

As indicated above, while challenging, structural analysis in aqueous Laponite systems can be conducted using small angle scattering methods. Although neutron scattering has the advantage of being able to leverage the use contrast matching as a means of identifying scattering contributions separately, synchrotron small angle x-ray scattering (SAXS) was used throughout this thesis.

2.5. Small Angle X-ray Scattering (SAXS)

SAXS has the advantage of enabling time resolved measurements since scattering is determined by the interactions between the incident x-ray beam and the electrons of a material; neutron scattering on the other hand relies on interactions with the nucleus and as such requires long data collection times.

2.5.1. Basics of SAXS

Small angle scattering of x-rays (SAXS) and neutrons (SANS) provides a fundamental method for structural analysis in condensed matter and can be applied to a large variety of materials including metal alloys, polymers, biomolecules and nanoparticles to name a few.

SAXS methods were first developed in the late 1930s when Guinier noticed that scattering at very small angles close to the primary beam provided structural information on inhomogeneities in metallic alloys⁵⁹. This method has since been used to study biological molecules as well as particles in various solutions and suspensions where long range crystalline structure does not exist. SAXS and SANS can be used to determine the particle size and shape, aggregation behavior, phase changes as well as information on overall organization⁶⁰.

Although the details of the physical scattering mechanisms for x-rays and neutrons are different, both arise from interactions between the incident beam and various aspects of the material being probed. For SAXS, the x-ray beam interacts with electrons while in the case of SANS, the neutron beam interacts with the nuclei within the bulk of the sample. Consequently, a material with a high electron density such as an inorganic particle scatters x-rays strongly while a polymer consisting of hydrocarbons does not scatter as strongly. In the case of SANS, the amount of scattering can be tuned through the use of contrast matching agents typically achieved by either incorporating heavier isotope directly into the material or, in the case of aqueous solutions, by using mixtures of H₂O and D₂O to match the scattering from components not of interest. Despite the

advantage of contrast matching, SAXS was chosen to study the Laponite dispersions due to the added advantage of short data collection times enabling time resolved measurements to determine dynamic structural changes.

2.5.2. SAXS experiments

SAXS experiments in this thesis were all conducted using transmission mode using dispersions and by mounting the samples directly between the source and detector. Scattering occurs as the incident beam passes through and interacts with the material and the scattered intensity was collected by a 2D MarCCD detector with an image plate; a beam stop is used to block the direct high intensity collimated x-ray beam. A simple schematic of the experimental setup is shown in Figure 2.7.

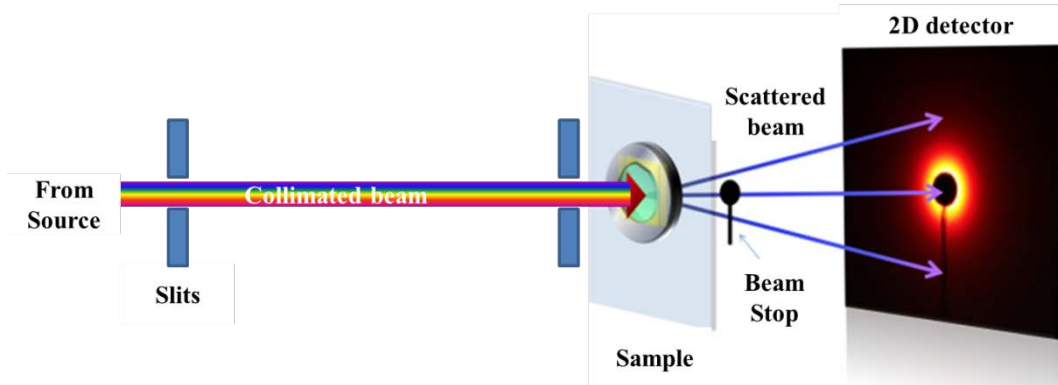


Figure 2.7 Schematic of transmission SAXS experiment with 2D data collected showing isotropic scattering.

2.5.3. SAXS data interpretation

SAXS scattering occurs as a result of interactions between the beam and sample. In its simplest form, the contributions to the overall scattering intensity, $I(q)$, is given by

$$I(q) = C_s S(q) P(q) \quad (2.1)$$

where C_s = sample concentration, q is the scattering vector defined as $q = 4\pi \sin \theta / \lambda$, λ is the scattering wavelength, θ is half of the scattering angle. $S(q)$ here represents the static structure factor while $P(q)$ describes the form factor.

The static structure factor, $S(q)$, represents the interaction between the scattering components and can be used to determine the overall structure or organization within the sample. On the other hand, the form factor, $P(q)$, depends solely on the shape and size of scattering components. In a dilute suspension for example, there is no interaction between the particles. Consequently, $S(q) \rightarrow 1$ and the scattering profiles depend solely on the shape of the particle. Figure 2.8 shows the scattering profile expected for dilute solutions of particles of different shapes.

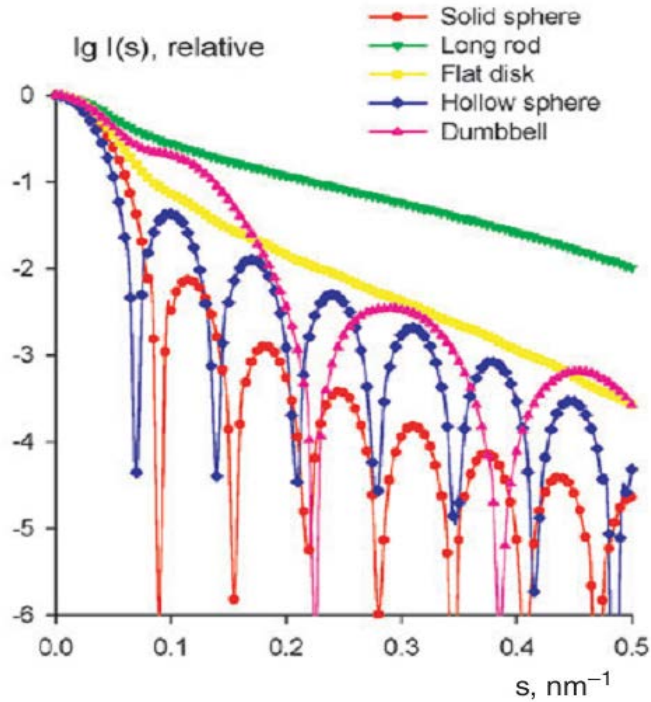


Figure 2.8 Typical scattering profiles from dilute solutions with particles of different shapes from Svergun *et al.* ⁶⁰.

For disk shaped particles as is the case of Laponite clay, the form factor $P(q)_{disk}$ ⁶¹ is given by

$$P(q)_{disk} \propto \left[\frac{\sin[qT\cos\alpha/2]}{[qT\cos\alpha/2]} \cdot \frac{J_1[qR_c\sin\alpha]}{[qR_c\sin\alpha]} \right] \quad (2.2)$$

where R is the radius of the disk, T is the thickness and α refers to the angle between the face of the disk and the incident beam. J_1 is the Bessel function of the 1st order. For low

concentrations, equation 2.2 can be applied to experimentally determine the average dimensions of the dispersed particles as discussed later in Chapter 4.

Since at low concentrations, $I(q)_{dil} = P(q)$ the structure factor for concentrated dispersions can be determined experimentally using⁶²

$$S(q)_{expt} = \frac{I(q)_{conc}}{I(q)_{dil}} = \frac{I(q)_{conc}}{P(q)} \cdot \frac{C_{dil}}{C_{conc}} \quad (2.3)$$

where the subscripts *dil* and *conc* refer respectively to the dilute and concentrated samples.

From this relationship, the length scales between scattering particles or clusters can in turn be determined. In general, when scattering objects interact with each other at a characteristic spacing, a plot of $S(q)_{expt}$ vs. q displays a strong correlation peak. For Laponite, the presence of this peak has been shown by Ruzicka *et al.* who also reported a change in the peak shape and position with aging time¹¹. Tanaka *et al.*¹⁴ further used the structure factor plots to differentiate between a gel and glassy phase (see Figure 2.9). Since these two states consist of different characteristic spacing where $D^*_{gel} < D^*_{glass}$, the peak position in a gel is typically observed at a higher q . More importantly, the gel state also displays a power law increase in $S(q)$ at very low q values such that

$$S(q)_{expt} \propto q^{-d_f} \quad (2.4)$$

d_f , in this case, represents the fractal dimension in the gel network.

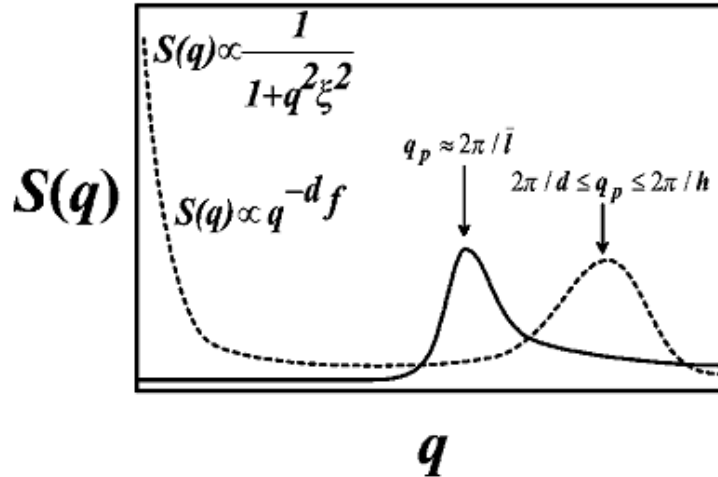


Figure 2.9 Schematic of experimental structure factor curves, $S(q)$, for the gel (dashed line) and glass (solid line) structures from Tanaka *et al.*¹⁴

The characteristic peak is shifted to higher q value for the gel structure and the graph exhibits a power law decay corresponding to the fractal dimension at very low q values. This also reflects the existence of the characteristic size of the growing network structure.

More recently, Paineau *et al.* studied structure in a variety of natural clay dispersions using SAXS⁶³. Rather than calculating an experimental structure factor as shown in equation 2.2, they use a simplified Lorentz corrected plot of $I(q) \cdot q^2$ vs. q where $I(q) \cdot q^2$ is used as an analogue to $S(q)_{\text{expt}}$ to describe the structure (Figure 2.10). Again, their results demonstrated a peak in the structure factor that is attributed to the characteristic inter-particle spacing in the system.

Using this peak position, Paineau and co-workers describe the decrease in the characteristic spacing as a function of increasing concentrations of a variety of natural clays such as beidellite (from Idaho) and 3 types of montmorillonite (from Arizona, Wyoming and Greece) with samples containing particle diameters ranging from 60nm to 350nm. Their results further show that as the volume fraction of clay increases and the samples undergo a sol-gel transition, a broadening of the maximum peak in $I(q) \cdot q^2$ can be observed.

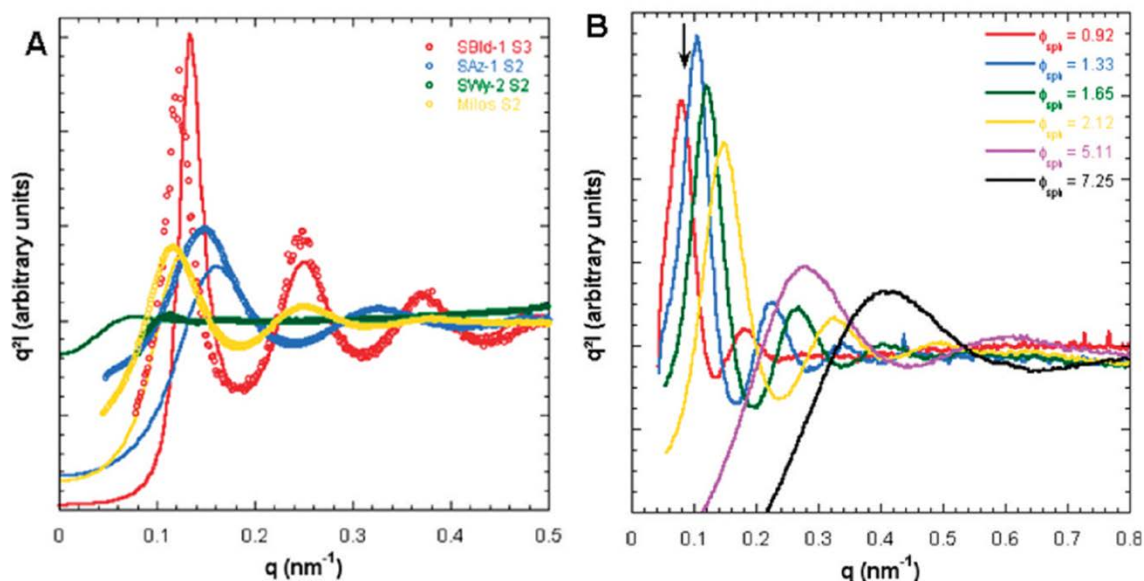


Figure 2.10 Graphs for $S(q)$ represented at Lorentz-corrected, $I(q).q^2$ plots from Paineau *et al.*

Graph (A) illustrates the results obtained at fixed ionic strength and clay volume fraction for 4 different natural clays with $\sim 200\text{nm}$ particle size while (B) shows the effect of increasing the clay volume fraction at constant ionic strength for Arizona montmorillonite and the arrow represents the sol-gel transition.

2.6. Summary of thesis goals

This thesis focuses on studying aqueous Laponite suspensions and the effect of adding a thermoresponsive triblock copolymer on both the bulk and nanoscale structure. SAXS and rheology are used to separately probe the structure and bulk properties as well as dynamic changes in the presence of F127 as a function of both temperature and UV light exposure.

For the purposes of this thesis, 3 types of SAXS experiments were conducted to study the structural rearrangement of the Laponite particles as well as dynamic changes in responsive systems. The experiments include

- Room temperature SAXS from pure Laponite
- Variable temperature SAXS with pure F127 and Laponite/ F127
- Simultaneous time resolved UV-SAXS of Laponite/F127/PAG systems.

For each set of experiment conducted, data processing was carried out in the same manner. First, a background subtraction was conducted using scattering from pure water to remove noise from the data. The 2D images were then integrated azimuthally to obtain 1D graphs of $I(q)$ vs. q . For all experiments, the samples were sealed with either Kapton (Brookhaven National Labs) or flame sealed wax when using capillaries (Argonne National Labs).

The main goal of this thesis is to determine how structure and bulk properties in the Laponite/F127 dispersions can be related to each other. The experiments and collected data are discussed in more detail within the following chapters in the thesis. Equation 2.3 was used to determine the changes in particle arrangement and structure of 3wt% Laponite with F127 dispersion as a function of temperature. On the other hand due to the complexity of the photo induced reaction described in Chapters 5 and 6, the method described by Paineau and coworkers for natural clays was applied to the time resolved data.

While the SAXS data collected in each section was essential to obtain information about the structural arrangement, the dispersions were further characterized using several other methods including

- a) light scattering to measure particle sizes
- b) differential scanning calorimetry to address thermo-physical changes particularly in the micellization behavior as a function of formulation
- c) rheology to address the flow properties and the effect of adding different components on the material. *In situ* thermal and photo rheology were also conducted to analyze the effect of temperature changes and UV exposure on the sol-gel transitions for responsive fluids
- d) microscopy (optical, SEM, AFM and TEM) to analyze changes in the microstructure and organization within the gels.

2.7. References

- (1) Israelachvili, J. N. *Intermolecular and surface forces: with applications to colloidal and biological systems (Colloid Science)* **1992**.
- (2) Ferry, J. D. *Viscoelastic properties of polymers*; Wiley New York, **1980**; Vol. 3.
- (3) Cummins, H. Z. *J. Non-Crystalline Solids* **2007**, *353*, 3891-3905.
- (4) Thompson, D. W.; Butterworth, J. T. *J. Colloid Interface Sci.* **1992**, *151*, 236-243.
- (5) Kroon, M.; Vos, W. L.; Wegdam, G. H. *Phys. Rev.* **1998**, *57*.
- (6) Mouchid, A.; Delville, A.; Lambard, J.; LeColier, E.; Levitz, P. *Langmuir* **1995**, *11*.
- (7) Mouchid, A.; Lécolier, E.; Van Damme, H.; Levitz, P. *Langmuir* **1998**, *14*.
- (8) Mouchid, A.; Levitz, P. *Phys. Rev.* **1998**, *57*.
- (9) De Bruyn, J. R.; Pignon, F.; Tsabet, E.; Magnin, A. *Rheol. Acta* **2008**, *47*, 63-73.
- (10) Ruzicka, B.; Zulian, L.; Ruocco, G. More on the Phase Diagram of Laponite. *Langmuir* **2005**, *22*.
- (11) Ruzicka, B.; Zaccarelli, E.; Zulian, L.; Angelini, R.; Sztucki, M.; Moussaïd, A.; Narayanan, T.; Sciortino, F. *Nat. Mater.* **2010**, *10*, 56-60.
- (12) Ruzicka, B.; Zulian, L.; Ruocco, G. *Philos. Mag.* **2007**, *87*, 449-458.
- (13) Bonn, D.; Tanaka, H.; Coussot, P.; Meunier, J. *J. Physics: Condens. Matter* **2004**, *16*.
- (14) Tanaka, H.; Meunier, J.; Bonn, D. *Phys. Rev.* **2004**, *69*.
- (15) Ruzicka, B.; Zaccarelli, E. *Soft Matter* **2011**, *7*, 1268-1286.
- (16) Ruzicka, B.; Zulian, L.; Zaccarelli, E.; Angelini, R.; Sztucki, M.; Moussaïd, A.; Ruocco, G. *Phys. Rev. Lett.* **2010**, *104*.
- (17) Cardinaux, F.; Zaccarelli, E.; Stradner, A.; Bucciarelli, S.; Farago, B.; Egelhaaf, S. U.; Sciortino, F.; Schurtenberger, P. *J. Phys. Chem. B* **2011**, *115*.
- (18) Zaccarelli, E.; Andreev, S.; Sciortino, F.; Reichman, D. R. *Phys. Rev. Lett.* **2008**, *100*.
- (19) Toledano, J. C. F.; Sciortino, F.; Zaccarelli, E. *Soft Matter* **2009**, *5*, 2390-2398.
- (20) Tanaka, H.; Jabbari-Farouji, S.; Meunier, J.; Bonn, D. *Phys. Rev.* **2005**, *71*.
- (21) Bonn, D.; Kellay, H.; Tanaka, H.; Wegdam, G.; Meunier, J. *Langmuir* **1999**, *15*.
- (22) Ruzicka, B.; Zulian, L.; Ruocco, G. *Phys. Rev. Lett.* **2004**, *93*.
- (23) Ruzicka, B.; Zaccarelli, E.; Zulian, L.; Angelini, R.; Sztucki, M.; Narayanan, T.; Sciortino, F.; Ruocco, G. *Nat. Materials*, **2011**, *10*, 56-60.
- (24) Jabbari-Farouji, S.; Tanaka, H.; Wegdam, G. H.; Bonn, D. *Phys. Rev.* **2008**, *78*.
- (25) Matthew, J. E.; Nazario, Y. L.; Roberts, S. C.; Bhatia, S. R. *Biomaterials* **2002**, *23*, 4615-4619.
- (26) Sosnik, A.; Cohn, D. *Biomaterials* **2005**, *26*, 349-357.
- (27) Alexandridis, P.; Holzwarth, J. F.; Hatton, T. A. *Macromolecules* **1994**, *27*, 2414-2425.
- (28) Alexandridis, P.; Alan Hatton, T. *Colloids Surfaces A: Physicochem. Eng. Asp.* **1995**, *96*, 1-46.
- (29) Wanka, G.; Hoffmann, H.; Ulbricht, W. *Colloid Polym. Sci.* **1990**, *268*, 101-117.
- (30) Bohorquez, M.; Koch, C.; Trygstad, T.; Pandit, N. *J. Colloid Interface Sci.* **1999**, *216*, 34-40.
- (31) Mortensen, K.; Batsberg, W.; Hvidt, S. *Macromolecules* **2008**, *41*, 1720-1727.

- (32) Yu, G.-E.; Deng, Y.; Dalton, S.; Wang, Q.-G.; Attwood, D.; Price, C.; Booth, C. *J. Chem. Soc., Faraday Trans.* **1992**, *88*, 2537-2544.
- (33) Chaibundit, C.; Ricardo, N. M. P. S.; Ricardo, N. M. P. S.; O'Driscoll, B. M. D.; Hamley, I. W.; Yeates, S. G.; Booth, C. *Langmuir* **2009**, *25*, 13776-13783.
- (34) Meznarich, N. A.; Juggernaut, K. A.; Batzli, K. M.; Love, B. J. *Macromolecules* **2011**, *44*, 7792-7798.
- (35) Wu, G.; Chu, B.; Schneider, D. K. *J. Phys. Chem.* **1995**, *99*, 5094-5101.
- (36) Prud'homme, R. K.; Wu, G.; Schneider, D. K. *Langmuir* **1996**, *12*, 4651-4659.
- (37) Wu, C.; Liu, T.; White, H.; Chu, B. *Langmuir* **1999**, *16*, 656-661.
- (38) Mortensen, K.; Talmon, Y. *Macromolecules* **1995**, *28*, 8829-8834.
- (39) Wanka, G.; Hoffmann, H.; Ulbricht, W. *Macromolecules* **1994**, *27*, 4145-4159.
- (40) Okada, A.; Kawasumi, M.; Usuki, A.; Kojima, Y.; Kurauchi, T.; Kamigaito, O. *MRS Proceedings*; **1989**; Vol. 171.
- (41) Okay, O.; Oppermann, W. *Macromolecules* **2007**, *40*, 3378-3387.
- (42) Haraguchi, K.; Farnworth, R.; Ohbayashi, A.; Takehisa, T. *Macromolecules* **2003**, *36*, 5732-5741.
- (43) Haraguchi, K.; Li, H.-J.; Song, L.; Murata, K. *Macromolecules* **2007**, *40*, 6973-6980.
- (44) Boucenna, I.; Royon, L.; Colinart, P. *J. Therm. Anal. Calorim.* **2009**, *98*, 119-123.
- (45) Ashby, N. P.; Binks, B. P. *Phys. Chem. Chem. Phys.* **2000**, *2*, 5640-5646.
- (46) Chang, C.-W.; Van Spreeuwel, A.; Zhang, C.; Varghese, S. *Soft Matter* **2010**, *6*, 5157-5164.
- (47) Haraguchi, K.; Masatoshi, S.; Kotobuki, N.; Murata, K. *J. Biomater. Sci. Polym. Ed.* **2011**, *22*, 2389-2406.
- (48) Majumdar, D.; Blanton, T. N.; Schwark, D. W. *Appl. Clay Sci.* **2003**, *23*, 265-273.
- (49) Bihannic, I.; Michot, L. J.; Lartiges, B. S.; Vantelon, D.; Labille, J.; Thomas, F.; Susini, J.; Salome, M.; Fayard, B. *Langmuir* **2001**, *17*, 4144-4147.
- (50) Schmidt, G.; Nakatani, A. I.; Butler, P. D.; Karim, A.; Han, C. C. *Macromolecules* **2000**, *33*, 7219-7222.
- (51) Nelson, A.; Cosgrove, T. *Langmuir* **2005**, *21*, 9176-9182.
- (52) Nelson, A.; Cosgrove, T. *Langmuir* **2004**, *20*, 10382-10388.
- (53) Nelson, A.; Cosgrove, T. *Langmuir* **2004**, *20*, 2298-2304.
- (54) De Lisi, R.; Lazzara, G.; Lombardo, R.; Milioto, S.; Muratore, N.; Liveri, M. T. *Phys. Chem. Chem. Phys.* **2005**, *7*, 3994-4001.
- (55) De Lisi, R.; Gradzielski, M.; Lazzara, G.; Milioto, S.; Muratore, N.; Prévost, S. *J. Phys. Chem. B* **2008**, *112*.
- (56) De Lisi, R.; Lazzara, G.; Milioto, S.; Muratore, N. *J. Therm. Anal. Calorim.* **2007**, *87*, 61-67.
- (57) Baghdadi, H. A.; Jensen, E. C.; Easwar, N.; Bhatia, S. R. *Rheol. Acta* **2008**, *47*, 121-127.
- (58) Zebrowski, J.; Prasad, V.; Zhang, W.; Walker, L. M.; Weitz, D. A. *Colloids Surfaces A: Physicochem. Eng. Asp.* **2003**, *213*, 189-197.
- (59) Guinier, A. *Ann Phys* **1939**, *12*, 161-237.
- (60) Svergun, D. I.; Koch, M. H. *Reports Prog. Phys.* **2003**, *66*.
- (61) Fournet, G.; Guinier, A. *Small-angle Scattering of X-rays*; **1955**.
- (62) Saunders, J. M.; Goodwin, J. W.; Richardson, R. M.; Vincent, B. A Small-Angle

X-ray Scattering Study of the Structure of Aqueous Laponite Dispersions. *J. Phys. Chem. B* **1999**, *103*.

(63) Paineau, E.; Bihannic, I.; Baravian, C.; Philippe, A.-M.; Davidson, P.; Levitz, P.; Funari, S. S.; Rochas, C.; Michot, L. J. *Langmuir* **2011**, *27*.

CHAPTER 3

3. Flow Properties of Aqueous Laponite/Pluronic F127 Dispersions

3.1. Chapter overview

In this chapter, the basic properties of aqueous Laponite clay dispersions and the effects of adding Pluronic F127 are characterized. Dynamic Light Scattering (DLS) and Differential Scanning Calorimetry (DSC) were first used to probe the interactions between the particles and polymer molecules in the aqueous phase. The bulk properties were then determined using visual observation, tube inversion and parallel plate rheometry experiments. Changes in the structure were assessed using electron microscopy (SEM and TEM) as well as atomic force microscopy (AFM). The results presented in this chapter demonstrate that the added F127 molecules interact directly with Laponite nanoparticles in the aqueous dispersions and that these interactions lead to significant changes in the bulk properties measured, including the ability to form a viscoelastic gel at room temperature.

3.2. Introduction

Clay suspensions have generated a large amount of interest due to their use in a variety of commercial applications ranging from oil and gas, electronics, household cleaners, paints, cosmetics and pharmaceuticals¹⁻³. Typically, these dispersions are formulated with various polymeric additives incorporated as rheology modifiers or stabilizers where the steric effect provided by the adsorbed polymer layers and the interactions occurring between the polymers and particles in the dispersion⁴⁻⁹ has a significant effect on the dispersion properties.

The behavior of a polymer/clay suspension can differ significantly from pure solutions of either polymer or clay alone and understanding these changes remains a key factor in the development of new fluid phase applications. For example, natural clay particles in solution are known to form an irreversible bulk gel with a network of particles¹⁰⁻¹³. The addition of polymers to the system can be used to tailor the conditions under which gel formation occurs as well as to prevent unwanted gelation¹⁴⁻¹⁷. Consequently, understanding the polymer/clay interactions is a key step in designing fluid systems with specific functional properties.

This study focuses on dispersions containing Laponite, a synthetic clay mineral with disk-like nanoparticles that are 20nm in diameter and 1nm thick³. Commercially available Pluronic F127 amphiphilic triblock copolymers, consisting of PEO-PPO-PEO where PEO is poly(ethylene oxide) and PPO is poly(propylene oxide), are used as the polymer surfactant component. F127 has been shown to adsorb onto the surface of the Laponite nanoparticles via interactions of the hydrophobic PPO block with the nanoparticles to stabilize the particles in solution and ensure relatively uniform dispersion^{14, 18, 19}.

3.3. Experimental Methods

Formulation: Aqueous dispersions of Laponite and F127 were prepared by adding the desired masses of Laponite and F127 to deionized water (d-H₂O). In the case of Laponite suspensions, the appropriate mass of powder was added to the water while stirring to prevent agglomeration. The vials were then sealed and subject to vortex mixing for 2-3 minutes followed by sonication for 20-30min until clear transparent sample were obtained.

Pure F127 solutions were prepared by first making a high concentration stock by step-wise dissolution of F127 powder in cold water. The stock solutions were kept in the refrigerator for at least 1 week for homogenization and diluted to desired concentrations prior to use. The final Laponite concentrations used ranged from 0.5-5wt% and F127 concentrations of 0.5-10wt% were used. All samples were allowed to age at least 24 hrs

to minimize any contributions from aging as reported elsewhere²⁰⁻²³. To prepare the mixed Laponite/F127 dispersions, Laponite suspensions were prepared as described above followed by addition of the desired amounts of F127 powder.

DLS: Dynamic Light Scattering (DLS) experiments were conducted on an ALV compact goniometer system (Model ALV/SP-125, Langen, Germany) equipped with an ALV/SO-SIPD photon detector. Dilute solutions of F127 and Laponite were analyzed to investigate the interactions between the nanoparticles and F127 molecules within the dispersion by probing the changes in particle sizes. A 200mW power Innova 70C argon ion laser (Coherent Inc., Santa Clara, CA) with a wavelength of 488nm was used as the light source and data was collected for 60s per spectrum after equilibration at 30°C at a 90° fixed angle. Particle size distributions were calculated from the autocorrelation functions using a constrained regularized method (CONTIN)²⁴ built in the ALV fitting software.

DSC: Differential scanning calorimetry (DSC) was performed using a Q2000 series DSC (TA instruments, DE) and hermetically sealed aluminum pans to suppress evaporation endotherms. Since F127 undergoes a micellization process prior to gelation, DSC was used to probe the changes in the micelle formation behavior upon addition of Laponite to different concentration F127 solutions. The experiments were carried out at a heating rate of 2°C/min from 0°C to 50°C.

Bulk Rheometry: Rheometry experiments were carried out using an ARES rheometer (TA Instruments, DE) with a parallel plate geometry equipped with 25mm diameter plates. The linear viscoelastic regime (LVR) was first measured using fixed deformation frequency of 10rad/s at applied strains of 0.01-500%. Oscillatory shear experiments were then conducted within the LVR to determine the frequency response of the samples the range of 0.01-100 rad/s. In all cases, the samples were loaded into the rheometer and allowed to equilibrate for 30 min prior to taking any measurements to account for deformation and shearing during the loading process.

Microscopy: SEM imaging was done on a FEI Nova Nanolab SEM with 10 kV operating voltage. Samples imaged were prepared by either drop casting and drying the dispersion on freshly cleaved mica or by lyophilization prior to imaging. All samples were gold coated for 30s to minimize charging. AFM was also conducted on spin coated samples using a Bruker Dimension Icon AFM in tapping mode. Particle size distribution was determined using a Phillips CM-100 TEM operated at 60kV to minimize damage during imaging.

3.4. Results and Discussion

3.4.1. Dynamic Light Scattering (DLS) ²⁵

To investigate potential interactions between the Laponite nanoparticles and added F127 molecules, DLS experiments were conducted at low concentrations of both F127 and Laponite (0.72wt% F127 with 0.2-0.6wt% Laponite). A pure Laponite dispersion without any added F127 was also measured to determine the average nanoparticle size. Low concentrations were used in all cases to avoid effects arising from interactions between particles in higher concentration dispersions as well as to minimize absorption of light during the DLS measurements. The scattered intensity data for each case was analyzed to generate a plot of hydrodynamic radii, R_H . The results obtained for the particle size distributions are summarized in Figure 3.1.

In the case of the pure 1.0wt% Laponite dispersion, DLS results show that the average particle size in the dispersion was ~17nm, a value consistent with the reported size of the disk-like nanoparticles. These values also agree closely with prior work by Nelson and Cosgrove ²⁶ as well as Nicolai and Cocard ²⁷ for measured bare Laponite particle radius on the order of 20nm.

Addition of F127 causes an increase in the mean hydrodynamic radius from ~17nm for the bare particles up to ~36nm for Laponite/F127 dispersions as shown by the shift in the peak position in Figure 3.1. The increase in the average particle size observed is attributed to the formation of a polymer shell around the Laponite nanoparticles. These

results are consistent with prior work by Nelson and Cosgrove using DLS to first demonstrate a change in particle size followed by contrast matched SANS to show that Pluronic triblock copolymers can adsorb onto the surface of Laponite nanoparticles^{18, 26} to produce a larger effective particle size. In all cases, the broad peaks obtained indicate polydispersity within the sample and can be attributed to several factors such as incomplete platelet separation, flocculation and possible clustering via particle aggregation.

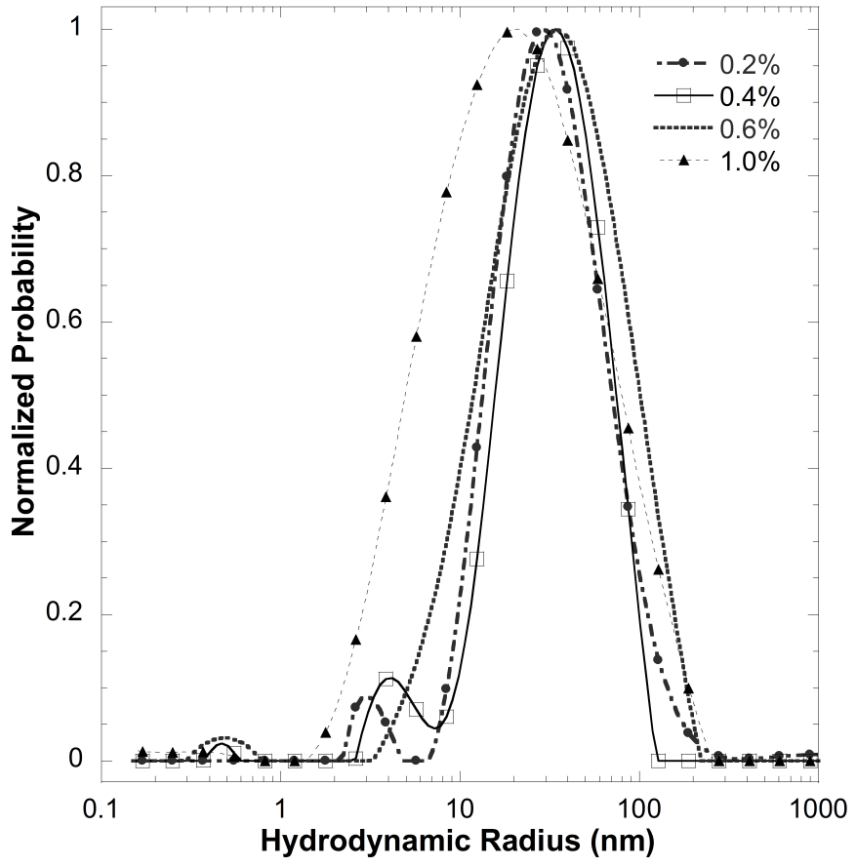


Figure 3.1 Hydrodynamic radii of aqueous dispersions from dynamic light scattering (DLS).

DLS data was collected at 90° for pure 1wt% Laponite dispersion and hybrid 0.72wt% F127 with 0.2wt%, 0.4wt% and 0.6wt% Laponite

3.4.2. Differential Scanning Calorimetry (DSC)

Based on the DLS results, the increase in average particle size indicates that F127 molecules can adsorb onto the surface of Laponite nanoparticles. This in turn results in a depletion of F127 molecules from the aqueous medium such that the concentration of

free molecules in the aqueous dispersion decreases. Since F127 in water has a well-known micelle forming behavior even at low concentrations²⁸, the adsorption of these molecules onto the Laponite and subsequent decrease of F127 concentration in solution is also expected to inhibit micelle formation since adsorbed molecules are no longer able to interact with each other. Consequently, DSC experiments probing the micellization thermodynamics was used to quantify this interaction and the depletion of F127 in solution. Two concentrations of 10wt% F127 and 25wt% F127 were initially used due to the presence of a large well studied micellization endotherm²⁸ at these values.

Figure 3.2(a) shows an example of the thermograms obtained for 10wt% F127 aqueous solution with small concentrations of Laponite. Figure 3.2(b) summarizes the effect of adding Laponite on the enthalpy of micelle formation, determined by the area of the micelle formation endotherm, for the two different F127 concentrations of 10wt% and 25wt% studied.

From Figure 3.2(a), at 10wt% F127 a clear endotherm corresponding to F127 micelle formation was obtained for all concentrations of added Laponite up to 1wt%. However, as the concentration of Laponite increases, three things are noted as summarized in Table 3.1:

1. The size of the micellization endotherm and hence enthalpy of micelle formation, ΔH_{mic} , decreases as the Laponite concentration increases
2. The temperature at which the micelle formation starts, T_{on} , exhibits a slight increase consistent with a lower F127 concentration in solution
3. The peak position of the endotherm, T_{peak} , occurs at slightly higher temperatures

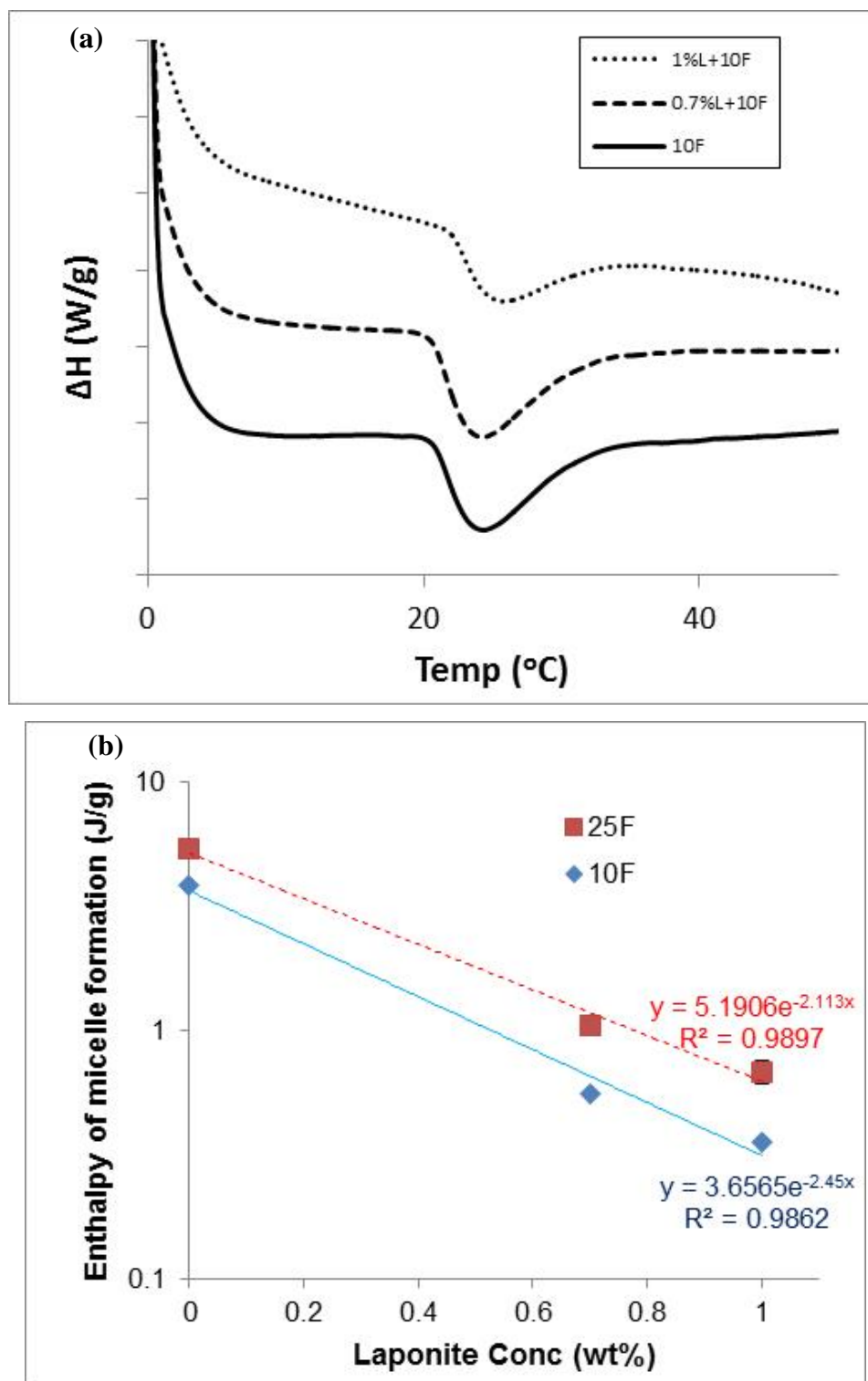


Figure 3.2 Typical DSC results for F127 and F127/Laponite dispersion.

(a) Typical DSC results obtained for 10wt% F127 with different Laponite concentrations. The graphs are shifted vertically for clarity (L = Laponite and F = F127). (b) Summary of the effect of adding small amounts of Laponite nanoparticles to the enthalpy of micelle formation at 10wt% and 25wt% F127.

Concentration (wt%)		T _{on} (°C)	T _{peak} (°C)	ΔH (J/g)
F127	Laponite			
10	0	15.08	18.63	3.85
	0.7	20.62	24.23	0.56
	1	21.99	25.63	0.35
25	0	12.04	15.42	5.39
	0.7	17.40	21.02	1.04
	1	19.27	22.78	0.68

Table 3.1 Summary of thermodynamic properties from DSC data.

Values shown are associated with the micelle formation process in F127 for 10wt% and 25wt% F127 with small amounts of added Laponite.

The decrease in the magnitude of ΔH , as well as the shifts in both T_{on} and T_{peak} are consistent with a lower effective polymer concentration present in the dispersion that can participate in micelle formation as the Laponite concentration in the system increases. As shown by the steeper slope for 10wt% F127 in Figure 3.2(b), the effect of small amounts of added Laponite is more pronounced at 10wt% F127 than at 25wt% F127 indicated by the larger slope. The difference in the extent to which the addition of Laponite affects the value of ΔH is attributed to the fact that for a given Laponite concentration, the depletion of F127 from solution due to surface adsorption is less significant with a high initial F127 concentration and the effects are less pronounced.

Interestingly, the results obtained differ from prior work by De Lisi *et al.*²⁹ and Boucenna *et al.*⁶ who both report that adding Laponite particles to 10wt% F127 in water has no effect on the micellization endotherm. We attribute this difference to the much slower heating rate used in the current experiment (2°C/min relative to 10°C/min from prior reports) which allows for better resolution of small changes as well as the increased sensitivity of the instrument used throughout this study.

The DSC and DLS results shown here, provide indications of significant interactions occurring between Laponite nanoparticles and F127 molecules in solution, most likely by

surface adsorption of F127 on Laponite. However, no direct evidence of bulk property changes was obtained from these measurements. To determine whether these polymer/particle interactions have significant impact on the bulk level behavior, a series of rheology measurements were conducted on both neat Laponite dispersions as well as Laponite/F127 systems of varying compositions. The results from these measurements are presented in detail throughout the rest of this chapter.

3.4.3. Rheology of pure Laponite dispersions

The room temperature rheological behavior of the different dispersions was probed first using strain sweeps at a fixed applied frequency of 10rad/s to determine the linear viscoelastic regime (LVR) followed by frequency sweeps at fixed strain within the LVR were then conducted to study flow characteristics. From the strain sweep data shown in Figure 3.3, both storage modulus, G' , and loss modulus, G'' , depend strongly on the Laponite concentration in the dispersion such that increasing the particle concentration causes both G' and G'' to increase. Several behavior regimes were observed:

1. At low applied strains ($\gamma < 10\%$) all samples behave linearly with $G' > G''$, a trend characteristic of linear viscoelastic materials with solid-like character, indicated by G' , dominating the flow behavior and confirming the existence of a weak bulk gel.
2. At larger applied strains, G' and G'' exhibit a general decrease with increasing γ such that for $\gamma > 10\%$, G'' exceeds G' . This transition is consistent with a shear thinning system where the material flows more readily with increased applied deformations (in this case, the applied strain, γ).
3. G'' exhibits a peak at a critical strain, γ_c , found to be $\sim 30\%$ for all concentrations. γ_c also corresponds to the point at which G' and G'' exhibit a crossover indicating a change in flow behavior from a solid like regime ($G' > G''$) to a liquid like behavior ($G' < G''$). This peak position in G'' represents a transition regime and corresponds here to the characteristic strain, γ_c , needed for the material to flow. Below this strain value, G' dominates and the material behaves similar to a viscoelastic solid while above this critical strain, G'' dominates and the material behaves more like a liquid.

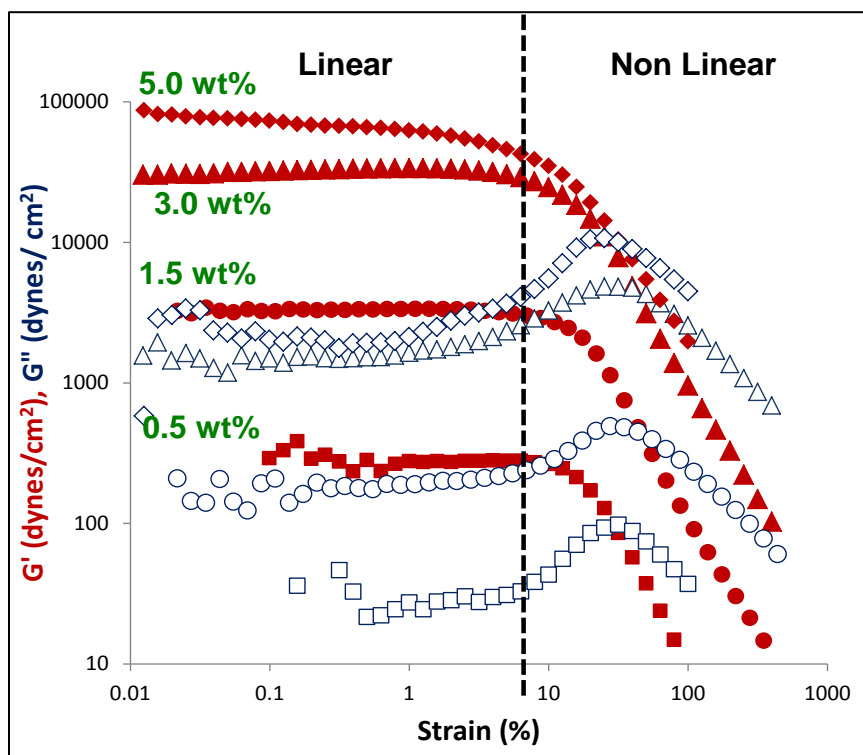


Figure 3.3 Results of strain sweeps at different Laponite concentrations in water.

(G' = solid and G'' = open)

The changes in the complex viscosity, η^* , at each Laponite concentration are shown in Figure 3.4 and correlate well with the expected flow properties as a function of deformation. The insets indicate the corresponding possible structure of particles within the dispersion. Results from the frequency response measurements conducted within the LVR are shown in Figure 3.5-Figure 3.8.

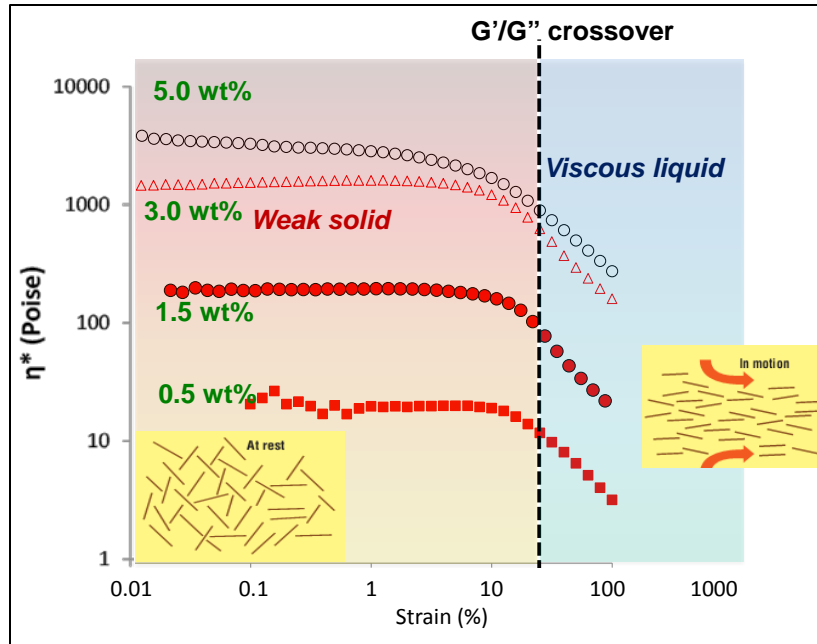


Figure 3.4 Dynamic viscosity at different Laponite concentration.

Data shows strain independent region (weak solid) and shear thinning region (viscous region). The insets illustrate the likely structure of particles in each region.

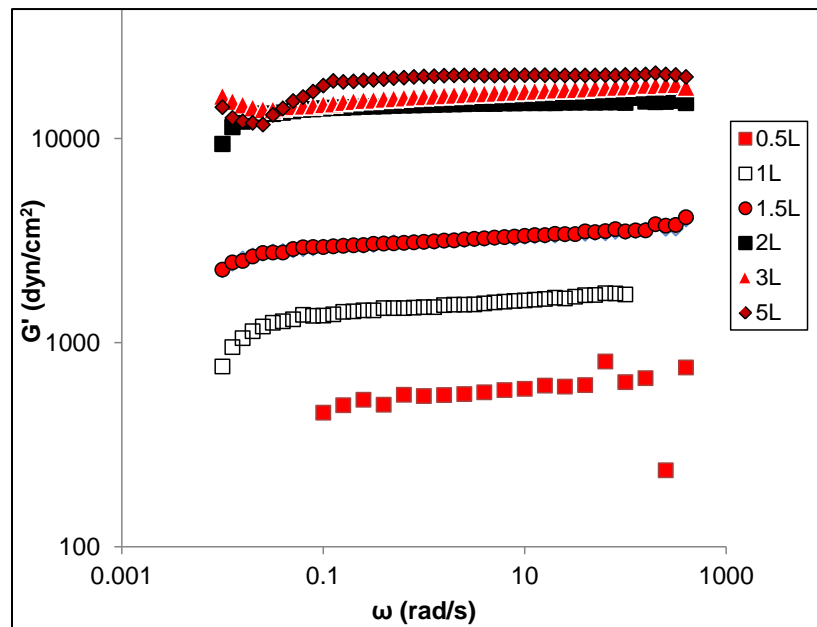


Figure 3.5 Frequency dependent G' for different Laponite concentrations in the LVR.

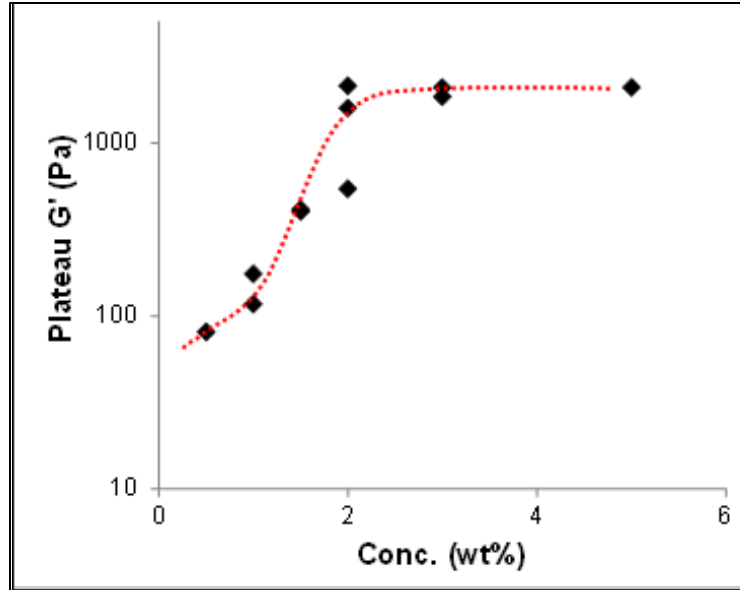


Figure 3.6 Concentration dependence of maximum G' for aqueous Laponite dispersions.

The dashed line is meant as a guide for the eye showing the change in G' as concentration of Laponite particles increases.

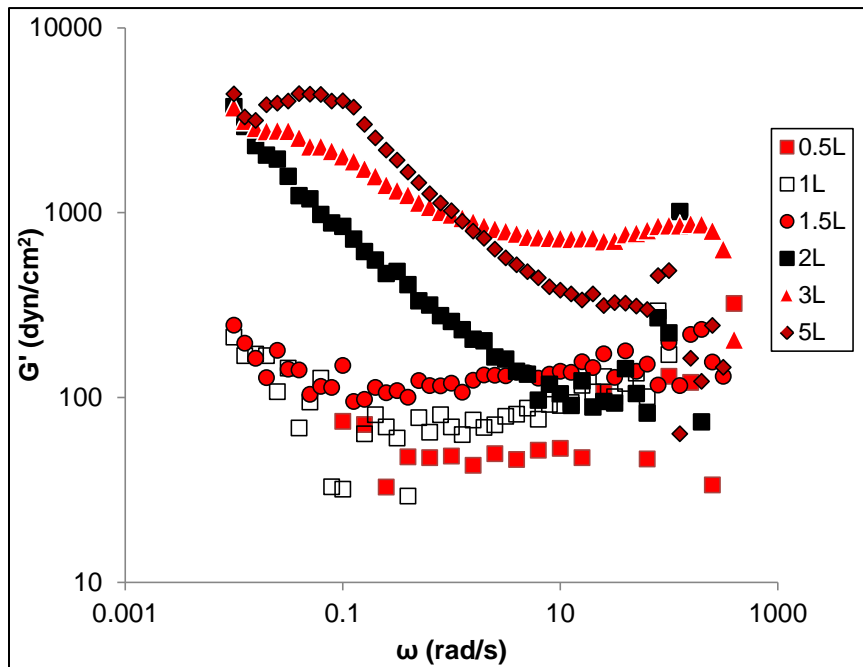


Figure 3.7 Frequency dependence of G' for different Laponite concentrations.

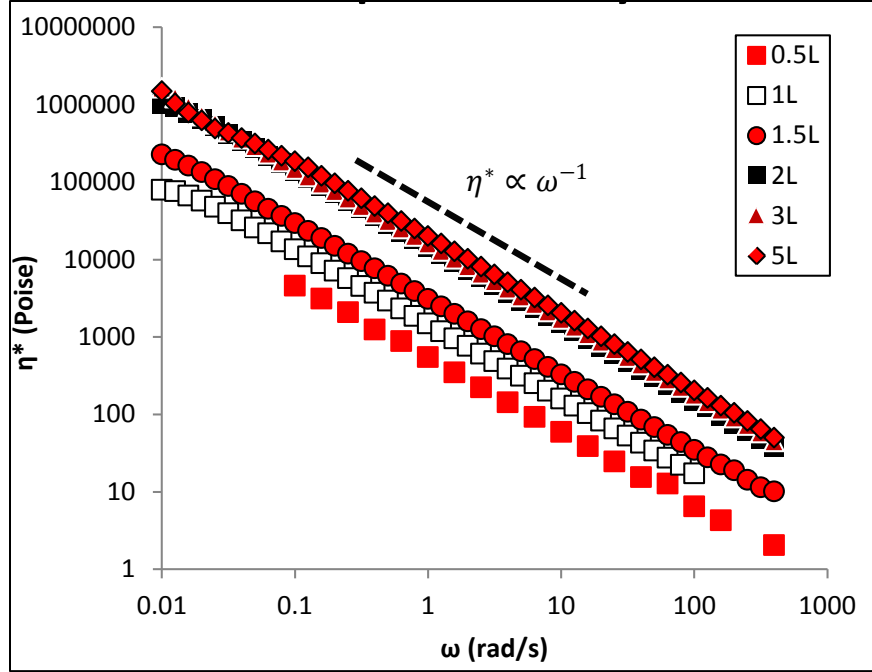


Figure 3.8 Frequency dependence of complex viscosity for different Laponite concentrations.

In all cases, the samples exhibit shear thinning characterized by a power law relationship with the power law exponent ~ -1 .

The storage modulus, G' , increases with increasing particle concentration reaching a maximum value achieved for concentrations $> 2\text{wt}\%$ Laponite. In all cases, dynamic rheology measurements show that G' is relatively frequency independent and exhibits a linear profile over the entire range probed. Since $G' > G''$ the solid-like behavior dominates and these samples are visually seen to be self-supporting gels. The increase in G' with increasing concentration indicates the formation of large elastic clusters. The formation of a plateau is consistent with possible saturation of elastic network junctions and indicates solid-like character within the physically associated network systems.

For all samples, the complex viscosity profiles, η^* , exhibit a shear thinning behavior with increasing deformation frequency, ω , as shown in Figure 3.8. This shear thinning character follows a power law relationship:

$$\eta^* = A\omega^{-k} \quad (3.1)$$

where A is a constant and $k \sim 1$. These results agree well with prior work by Mourchid *et al.*^{30,31} and Willenbacher³² for pure Laponite gels with a 3D network structure.

3.4.4. Rheology of mixed Laponite/Pluronic F127 dispersions

Since Laponite dispersions are often used in the presence of other components including polymers and surfactants, the effect of adding a commercially available triblock copolymer, Pluronic F127, on the bulk properties of aqueous Laponite dispersions was investigated. First the concentration of Laponite was kept fixed at 3wt% while F127 was added to the dispersion to achieve concentrations of up to 10wt% (picture of samples in Appendix 3A). The dynamic frequency response of each solution was probed at room temperature using 1% applied strain (previously found to be within the LVR) and the results are summarized in Figure 3.9.

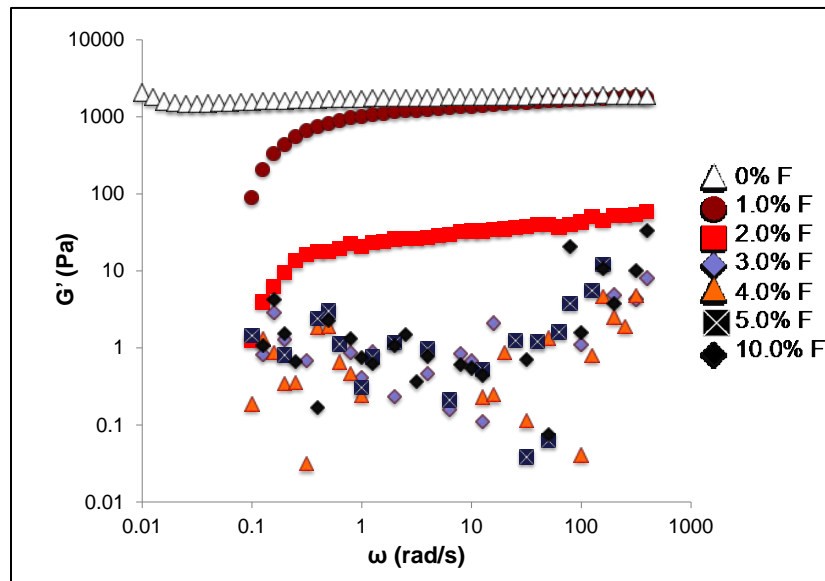


Figure 3.9 Room temperature frequency response for 3wt% Laponite with added F127.

From Figure 3.9, addition of F127 causes a progressive and significant decrease in the value of the storage modulus, G' . Above 2wt% F127, G' is no longer linear and well-defined but exhibits a noisy profile at very low G' value indicating that the sample behaves like a simple fluid at all probed frequencies. Since the gelation suppression upon adding small amounts of F127 is not instantaneous, the progressive loss of solid-like character with F127 addition indicates that a critical polymer/particle ratio is required to suppress the inter-particle interactions driving network (and subsequent gel) formation.

These effects were further probed at a fixed F127 concentration of 3.6wt% while changing Laponite content from 0-5wt%. These results are summarized in Figure 3.10.

Adding trace amounts of Laponite to 3.6wt% F127 has a negligible effect on the dynamic rheology. Instead, samples with less than 5wt% Laponite exhibit liquid-like character rather than that of a viscoelastic solid. At 5wt% Laponite concentration, the viscoelastic behavior was again observed with a correspondingly large increase in the value of G' . Figure 3.10(c) provides a direct comparison describing the effect of adding 3.6wt% F127 on the flow behavior of aqueous dispersions of 5wt% Laponite. As shown here, although the value of G' decreases in the presence of the F127, the sample retains viscoelastic behavior, indicating that adding F127 results in a weaker solid.

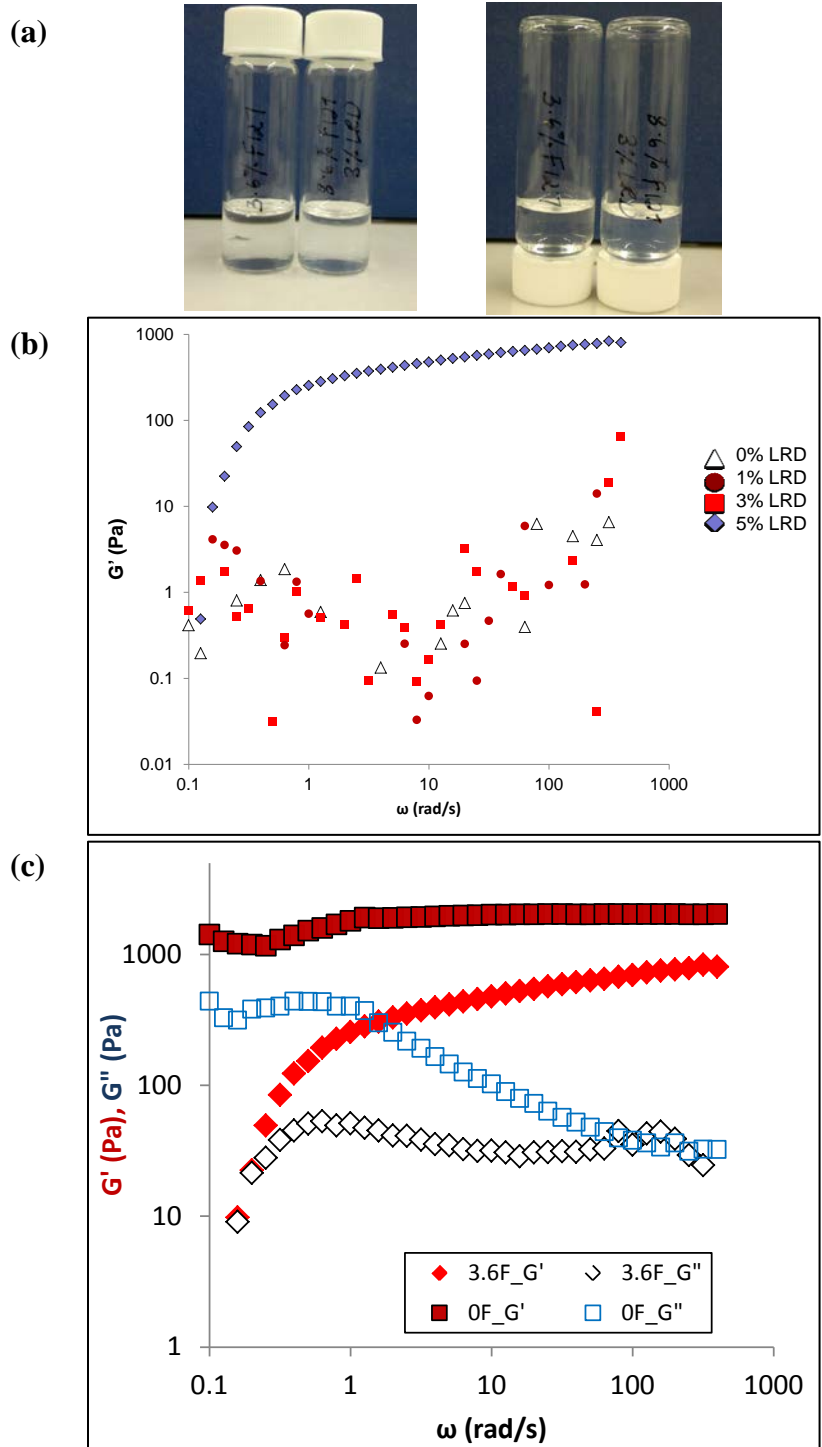


Figure 3.10 Summary of solution properties of 3.6wt% F127 with 3wt% Laponite

(a) photograph of 3.6wt% F127 with no particles (left) and with 3wt% Laponite (right). (b) Frequency response of G' as a function of increasing Laponite concentration at fixed 3.6wt% F127. Select curves are shown for clarity. (c) Comparing G' and G'' data for 5wt% Laponite with no added F127 (OF) and 3.6wt% F127 (3.6F).

Since neat Laponite gels are formed by inter-particle interactions where the pure dispersions exhibit a behavior characteristic of the presence of an elastic network of clusters, the decrease in G' with the presence of the F127 molecules is attributed to the screening of partial particle interactions. Here, due to the high particle to polymer ratio, these inter-particle interactions are not completely shielded resulting in an *effective* free particle concentration, C_{eff} where C_{eff} represents the concentration of particles that are still able to interact with each other to form elastic clusters responsible for the viscoelastic or gel-like behavior. Taking the screening effect into account and comparing G' values to Figure 3.6 for neat Laponite, we find that for the G' values measured in the case of 5wt% Laponite + 3.6wt% F127 dispersion, C_{eff} corresponds to ~1.5-2.0wt% Laponite particles. This value for C_{eff} indicates that the presence of 3.6wt% F127 in the dispersion efficiently interacts with and inhibits 3-3.5wt% of the particles Laponite initially present in the 5wt% dispersion from interacting with each other. These values indicate that complete shielding of particle/particle interactions and gel suppression is most likely to occur at Laponite to F127 ratio slightly less than 1; that is a slightly larger concentration of F127 must be present in the dispersion for effective shielding of inter-particle interactions. This expected behavior is consistent with the results shown in Figure 3.9 where complete suppression of viscoelastic character in 3wt% Laponite dispersions was observed for concentrations of $F127 \geq 3wt\%$.

3.4.5. Microstructure in mixed dispersions

In a mixed dispersion, interactions between the particles and polymer lead to significant changes in the fluidity of the sample as shown by the bulk rheology experiments. Since structure and properties are intimately related to each other, these changes indicate that changing the formulation composition results in significant changes in structure and arrangement. To probe the structural changes, microscopy experiments were conducted first on samples drop cast and dried on freshly cleaved mica. Representative micrographs are shown in Figure 3.11 (A1 – D1) illustrate the changes in morphology of 3.6wt% F127 with increasing amounts of Laponite.

With no added Laponite, the F127 film exhibits significant cracking upon drying while adding a small amount of Laponite results in a smooth and continuous film with little to no cracking. Further increase in Laponite content led to more evidence of agglomeration and micro-cracks (Figure 3.11, C1 and D1). This change in the morphology is attributed to aggregation of the Laponite particles into small domains at the higher concentration. The results here for 3.6wt% F127 and up to 3.0wt% added Laponite are typical of the morphology observed for dried films of polymer/clay and consistent with prior work by Pizzey *et al.*³³.

Drop casting and drying of the Laponite dispersion leads to a complete loss of three dimensional structure and arrangement responsible for the formation of a gel. To preserve the macroscopic arrangement, dispersions prepared at room temperature were instead lyophilized prior to imaging. Representative micrographs of these lyophilized samples obtained for 3.6wt% F127 with increasing Laponite concentration from 0wt% to 5wt% are shown in columns 2 and 3 of Figure 3.11 at low and high magnifications respectively. Figure 3.12 further depicts the morphologies of the lyophilized samples at high magnification in areas corresponding to the boxed regions of Figure 3.11.

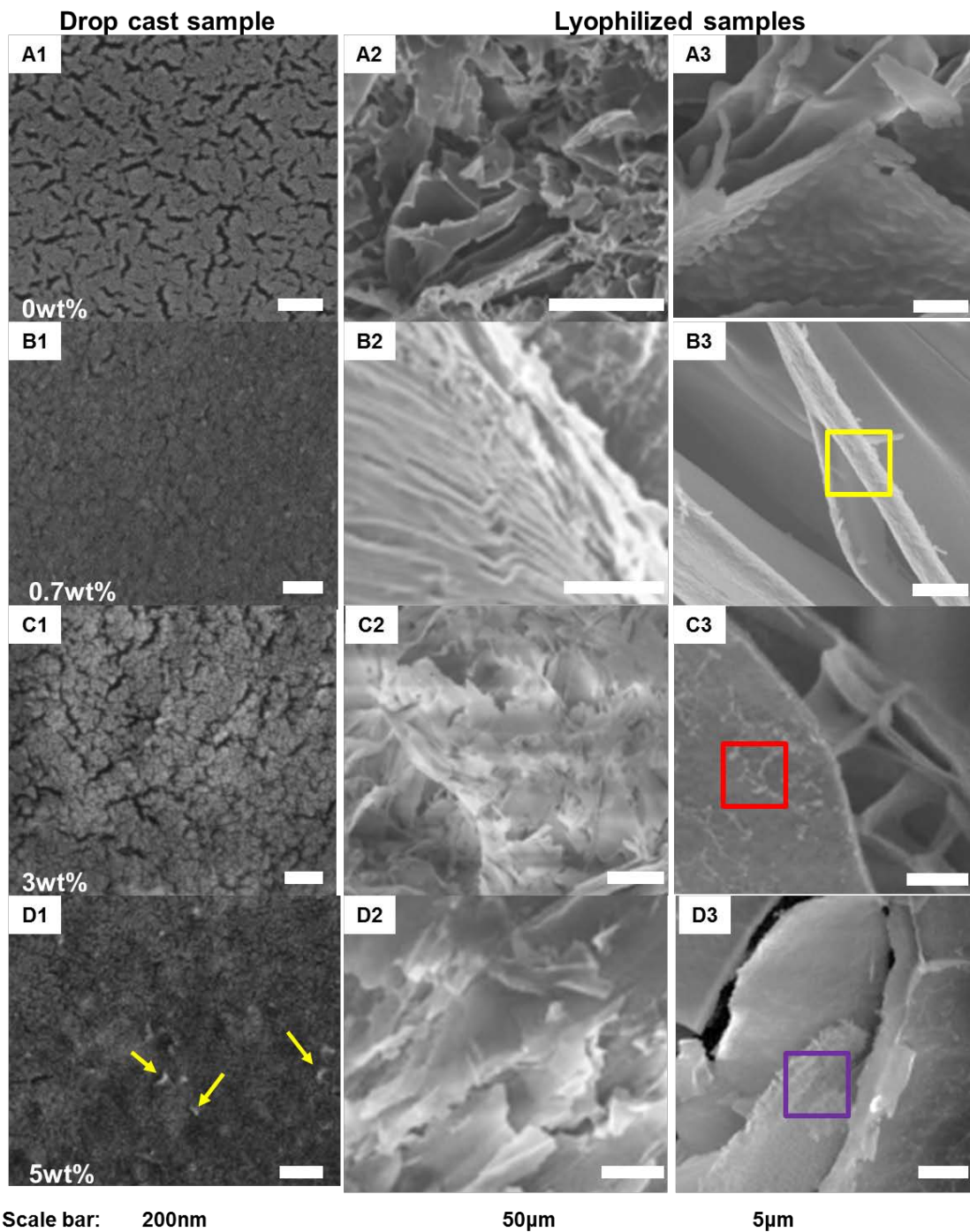


Figure 3.11 Microstructure of 3.6wt% F127 dispersions with increasing Laponite content.

A1-D1: Drop cast and dried samples result in films of different morphology while lyophilized samples (A2-D3) retain the structure for samples prepared at RT and show clear differences with added Laponite (top to bottom: 0wt%, 0.7wt%, 3wt% and 5wt%). The arrows in panel D1 highlight clusters showing aggregates obtained at high Laponite concentration.

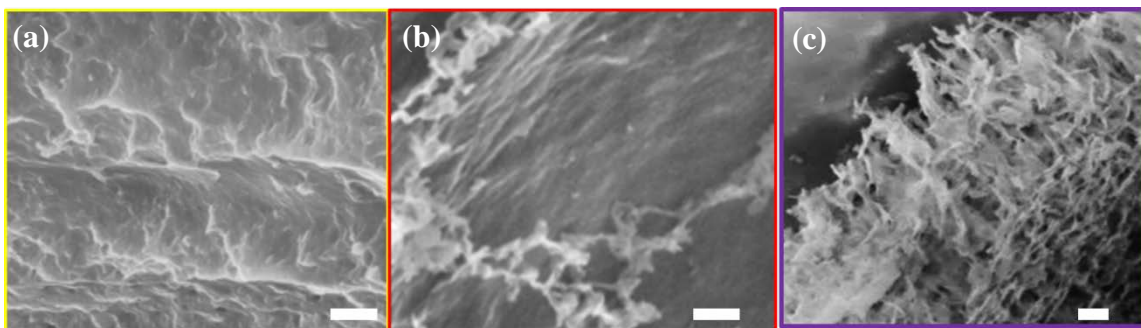


Figure 3.12 High magnification SEM of lyophilized samples.

3.6wt% F127 with 0.7wt (a), 3wt% (b) and 5wt% (c) Laponite (Scale bar = 400nm)

From Figure 3.11, as the Laponite content initially increases, the dried film and lyophilized structures both become more uniform and continuous with minimal cracks and little to no evidence of individual particles within the layered structure (Figure 3.11 B1-B3 and Figure 3.12 (a)). With further increase in Laponite content to 3wt%, the air dried films start showing evidence of agglomeration while the lyophilized samples on the other hand, exhibit an interconnected layered structure as seen in Figure 3.11 C3. Further increasing the particle concentration in turn leads to an interconnected network (Figure 3.12(b)). The morphologies shown here are typical of flexible natural clay platelets previously reported^{13, 33} and the network structure obtained is believed to be caused by a bridging network of particles.

Further increase in Laponite content to 5wt% showed particle aggregation. The arrows shown Figure 3.11 D1 highlight the presence of clusters noted on the drop-cast and air dried films. The cluster dimensions were found to be in the range of 65 ± 12 nm from these samples. In the case of the lyophilized 5wt% Laponite dispersions, areas consisting exclusively of a 3D network of bridge particles were also observed (Figure 3.12 (c)).

These morphology changes provide additional support to the rheology measurements indicating stabilization of particles at the particle/polymer ratio much larger than 1:1 and the 3D network formation is attributed to incomplete particle shielding such that these particles can interact with each other and arrange into 3D networks.

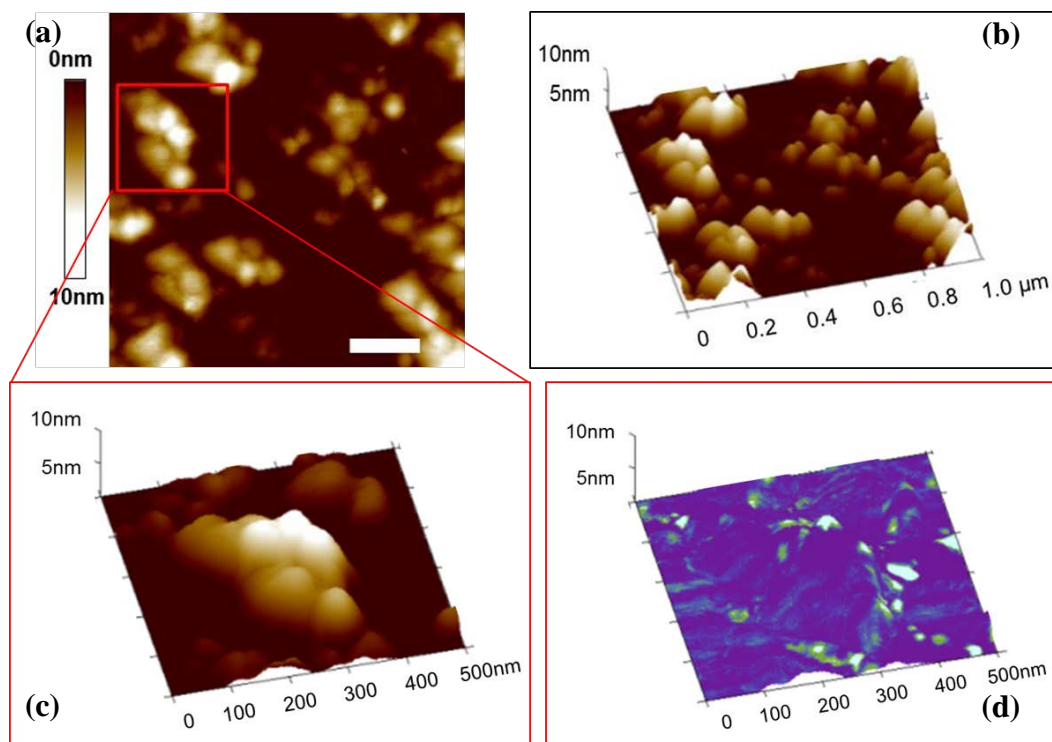


Figure 3.13 AFM from 3.6wt% F127 + 3wt% Laponite spin coated on freshly cleaved mica.

Top row: 1 μm x 1 μm scan topography maps ((a) 2D, (b) 3D); bottom row: 500nm x 500nm scan of “islands” ((c) = topography image; (d) = phase overlaid on topography image). Bright regions in the phase image shown in (d) are attributed to Laponite rich areas.

Figure 3.13 illustrates AFM images taken of a film of 3.6wt% F127 with 3wt% Laponite spin coated onto freshly cleaved mica. The film indicates significant topography with (a) and (b) showing the height changes on the sample surface; while significant topography was observed, individual particles were difficult to locate from the height images even at high magnification as shown in (c). Instead a phase image overlaid on the topography was used to highlight regions of different compositions as shown in Figure 3.13(d). The light colored areas seen here are caused by regions rich in Laponite although individual particles were not clearly observed likely due to aggregation and collapse of the overall particle network.

Further imaging was conducted using TEM to determine individual particle size and arrangement. Figure 3.14 shows images obtained for samples prepared by drop casting the aqueous dispersions directly onto a Cu grid and subsequent drying at room

temperature. Select images from neat 10wt% F127, neat 1wt% Laponite and a mixed dispersion of 10wt% F127 and 1wt% Laponite are shown.

From Figure 3.14(a) and (d) obtained for 10wt% F127 clearly show the presence of spherical micelles. Individual micelles were found to have diameter of $30\pm 3.9\text{nm}$ while aggregates of 2-4 micelles had diameters of $50\pm 5.2\text{nm}$. Figure 3.14(b) and (e) show images for 1wt% Laponite at low and high magnification respectively. Clusters of particles (Figure 3.14(b)) were noted on drying while higher magnification imaging reveals that individual particles with diameter $22\pm 4.3\text{nm}$ are present within the clusters (Figure 3.14(e)). The Laponite particles were found arranged in both a face-to-face configuration as well as face-to-edge configuration with cluster sizes of $\sim 50\text{-}70\text{nm}$.

In the case of the 10wt% F127 and 1wt% F127 dispersion, the sample dries into a relatively uniform film shown in Figure 3.14(c). Again, at higher magnification, individual particles were observed. The film from the F127-Laponite system exhibits a relatively uniform distribution of well separated particles with diameter $\sim 21\pm 3.7\text{nm}$. Interestingly, despite the high F127 concentration in the mixture, no evidence of micelle formation at room temperature in the presence of Laponite was observed.

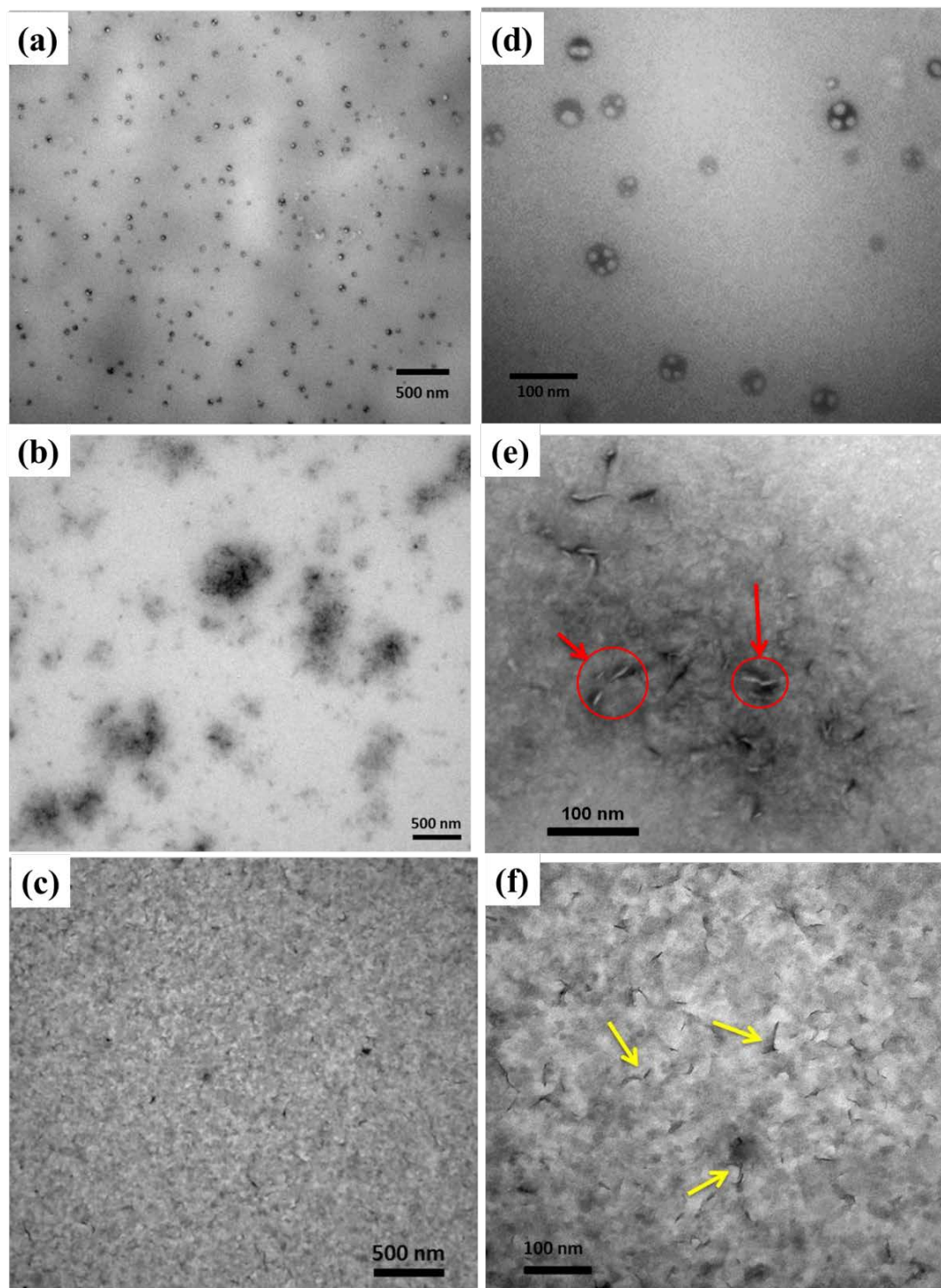


Figure 3.14 Representative TEM from drop cast samples.

Micrographs from samples by drop casting and drying 5 μ l of dispersion directly onto a Cu grid at room temperature. Micrographs show the structure for: (a) and (d) : neat 10wt%F127 with spherical micelles, (b) and (e): neat 1wt% Laponite and (c) and (f): mixed 10wt%F127 with 1wt% Laponite.

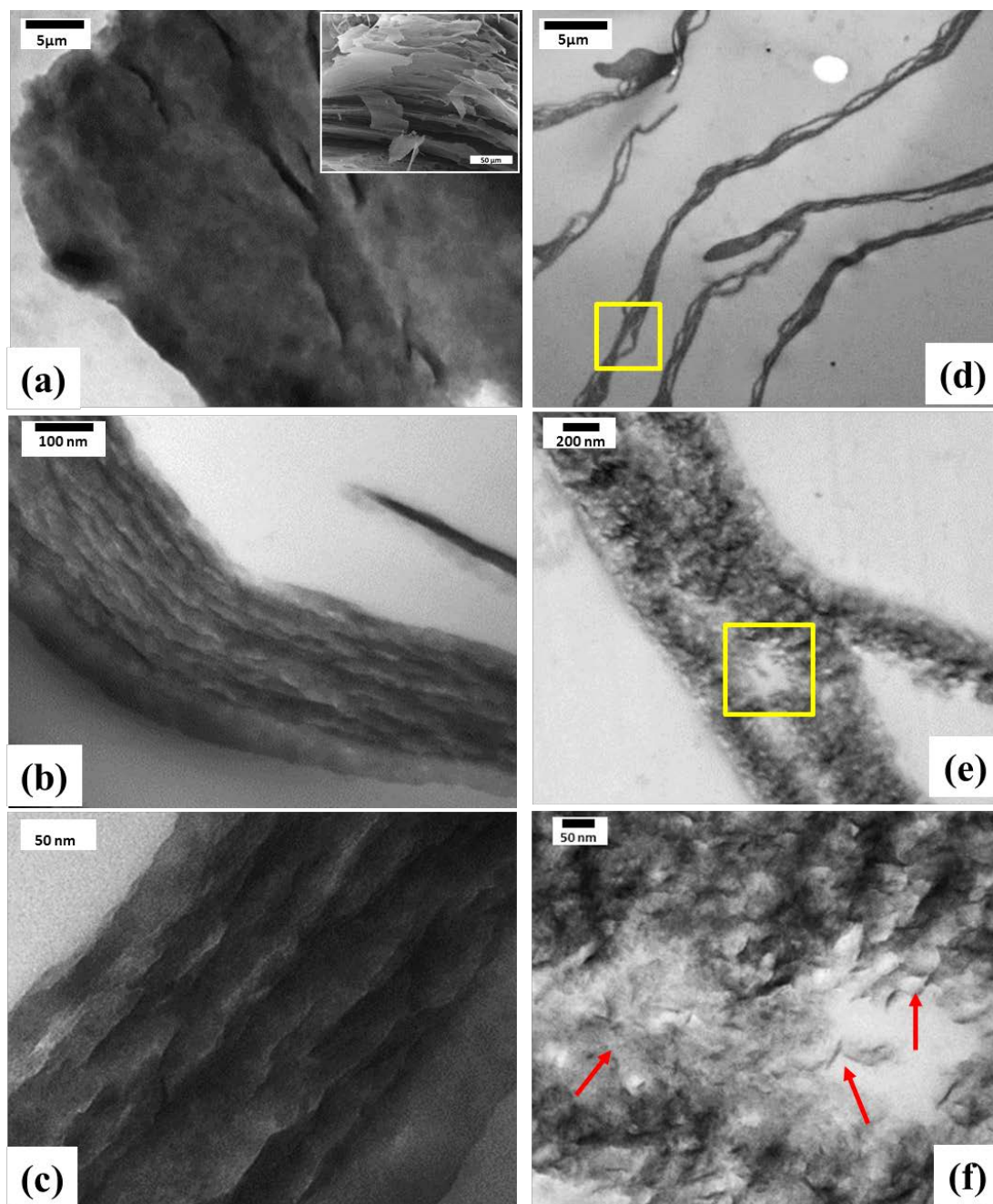


Figure 3.15 Representative TEM micrographs from lyophilized gels.

Samples prepared at RT and lyophilized were embedded in epoxy and ultramicrotomed. Slices were stained with uranyl acetate prior to imaging. (a)-(c) illustrate images from 3wt% neat Laponite gel and (d)-(f) depict the structure upon adding 3.6wt% F127 to 3wt% Laponite. Inset in (a) shows SEM of lyophilized neat Laponite at 3wt% concentration with layered structure.

As noted previously, the drop casting and drying process results in a loss of structure. To probe the internal arrangement in the system, the aqueous lyophilized samples described

previously, were embedded in epoxy and sliced using an ultra-microtome to prepare samples thin enough for TEM imaging. Prior to imaging the slices were stained with uranyl acetate to enhance contrast between the epoxy and the sample and representative images are shown in Figure 3.15.

Figure 3.15(a)-(c) illustrate details of the layered morphology for neat 3wt% Laponite (SEM inset in (a)) while (d)-(f) depicts details of the structure in 3.6wt% F127 with 3wt% Laponite (SEM images in Figure 3.11 C1-C3). For neat Laponite gels, surprisingly individual particles were difficult to identify likely a consequence of the heavy metal staining procedure resulting in smearing of the structure. In the case of the F127/Laponite dispersions, the porous layers previously observed via SEM as shown in Figure 3.11 were observed at low magnification. At high magnification, well dispersed individual particles of diameter 23 ± 3.6 nm were clearly identified throughout the layer of lyophilized material confirming both exfoliation and dispersion of the Laponite particles within the layers of the gel (Figure 3.15(f)).

The combined SEM, AFM, and TEM results show that while, drying results in a collapse of the network structure, lyophilization enables preservation of the 3D network within a gel which can subsequently be imaged successfully. The micrographs shown clearly illustrate the morphology changes as a result of formulation differences. The initial results shown here provide a direct indication that morphology and properties are inherently related to each other. These results also indicate that significant interactions exist between the Laponite and F127 within the dispersion and confirm that for complete stabilization of Laponite particles and suppression of inter-particle interactions, the F127 concentration must be higher than the Laponite concentration.

3.5. Conclusions

This chapter has focused on the room temperature behavior and structure of pure Laponite dispersions and the effect of adding a triblock copolymer surfactant, Pluronic F127, to these dispersions. The results presented show that Laponite nanoparticles

dispersed in water form a bulk gel with well-defined viscoelastic character. The solid-like character indicated by the storage modulus, G' , increases and becomes more dominant with increasing particle concentrations; a behavior consistent with the formation of a stiffer substance, in this case, a stiffer hydrogel. The G' dependence on the Laponite concentration indicates the likelihood of forming elastic clusters that interact with each other increases with the particle concentration. At Laponite concentrations above 2wt%, G' values reach a plateau and remain relatively constant up to the highest measured concentration of 5wt%.

Upon adding F127 to Laponite dispersions, significant interactions take place between the particles and polymer leading to adsorption of the polymer molecules onto the nanoparticle surface. This adsorption is evidenced by both an increase in effective particle size obtained from DLS and a suppression of polymer micelle formation as measured via DSC. These interactions in turn lead to significant changes in the dispersion bulk properties including a decrease in G' attributed to screening of inter-particle interactions leading to network formation and subsequent suppression of gelation.

For complete suppression of the network formation, the results presented indicate that the polymer to particle ratio must be larger than 1. This behavior can be explained by the need to completely screen inter-particle interactions to fully prevent gels from forming. At lower polymer concentrations, the screening process remains incomplete leading to an *effective* particle concentration, C_{eff} , capable of interacting within the dispersion as described in this chapter.

Images obtained show that drying of these gels results in complete collapse and loss of structure. Lyophilization, on the other hand, helps preserve the overall structure and shows that as the Laponite concentration increases in 3.6wt% F127, the bulk structure exhibits increased ordering. For a 5wt% concentration, regions of a 3D network of interacting particles were also observed consistent with rheology measurements indicating incomplete suppression of particle network formation.

3.6. References

- (1) Van Olphen, H. *An introduction to clay colloid chemistry: for clay technologists, geologists, and soil scientists*; Wiley, New York, **1977**.
- (2) Thompson, D. W.; Butterworth, J. T. *J. Colloid Interface Sci.* **1992**, *151*, 236-243.
- (3) Cummins, H. Z. *J. Non-Crystalline Solids* **2007**, *353*, 3891-3905.
- (4) Boucenna, I.; Royon, L.; Colinart, P.; Guedeau-Boudeville, M.-A.; Mourchid, A. Structure and Thermorheology of Concentrated Pluronic Copolymer Micelles in the Presence of Laponite Particles. *Langmuir* **2010**, *26*, 14430.
- (5) King Jr, H. E.; Milner, S. T.; Lin, M. Y.; Singh, J. P.; Mason, T. G. *Phys. Rev. E* **2007**, *75*, 021403.
- (6) Boucenna, I.; Royon, L.; Colinart, P. *J. Therm. Anal. Calorim.* **2009**, *98*, 119-123.
- (7) De Lisi, R.; Lazzara, G.; Milioto, S.; Muratore, N. *Langmuir* **2006**, *22*, 8056-8062.
- (8) De Lisi, R.; Gradzielski, M.; Lazzara, G.; Milioto, S.; Muratore, N.; Prévost, S. *J. Phys. Chem. B* **2008**, *112*.
- (9) De Lisi, R.; Lazzara, G.; Lombardo, R.; Milioto, S.; Muratore, N.; Liveri, M. T. *Phys. Chem. Chem. Phys.* **2005**, *7*, 3994-4001.
- (10) Low, P. F.; Margheim, J. F. *Soil Sci. Soc. Am. J.* **1979**, *43*, 473-481.
- (11) Van Olphen, H. E. N. D. R. I. K. In *Clays and Clay Miner. II (Proc. 11th Natl. Conf. Clays and Clay Miner. 1962, MacMillan, New York, pp. 178-187)*; **1963**.
- (12) Michot, L. J.; Bihannic, I.; Maddi, S.; Baravian, C.; Levitz, P.; Davidson, P. *Langmuir* **2008**, *24*, 3127-3139.
- (13) Paineau, E.; Bihannic, I.; Baravian, C.; Philippe, A.-M.; Davidson, P.; Levitz, P.; Funari, S. S.; Rochas, C.; Michot, L. J. *Langmuir* **2011**, *27*.
- (14) Loiseau, A.; Tassin, J.-F. *Macromolecules* **2006**, *39*.
- (15) Zebrowski, J.; Prasad, V.; Zhang, W.; Walker, L. M.; Weitz, D. A. *Colloids Surfaces A: Physicochem. Eng. Asp.* **2003**, *213*, 189-197.
- (16) Haraguchi, K.; Farnworth, R.; Ohbayashi, A.; Takehisa, T. *Macromolecules* **2003**, *36*, 5732-5741.
- (17) Wheeler, P. A.; Wang, J.; Mathias, L. J. *Chem. Mater.* **2006**, *18*.
- (18) Nelson, A.; Cosgrove, T. *Langmuir* **2005**, *21*, 9176-9182.
- (19) Nelson, A.; Cosgrove, T. *Langmuir* **2004**, *20*, 10382-10388.
- (20) Abou, B.; Bonn, D.; Meunier, J. *Phys. Rev.* **2001**, *64*.
- (21) Bellour, M.; Knaebel, A.; Harden, J. L.; Lequeux, F.; Munch, J.-P. *Phys. Rev.* **2003**, *67*.
- (22) Zulian, L.; Ruzicka, B.; Ruocco, G. *Philos. Mag.* **2008**, *88*, 4213-4221.
- (23) Patil, S. P.; Mathew, R.; Ajithkumar, T. G.; Rajamohanam, P. R.; Mahesh, T. S.; Kumaraswamy, G. *J. Phys. Chem. B* **2008**, *112*, 4536-4544.
- (24) Provencher, S. W. *Comput. Phys. Commun.* **1982**, *27*, 229-242.
- (25) Juggernaut, K. A.; Gros, A. E.; Meznarich, N. A.; Love, B. J. *Soft Matter* **2011**, *7*, 10108-10115.
- (26) Nelson, A.; Cosgrove, T. *Langmuir* **2004**, *20*, 2298-2304.
- (27) Nicolai, T.; Cocard, S. Light Scattering Study of the Dispersion of Laponite. *Langmuir* **2000**, *16*.
- (28) Bohorquez, M.; Koch, C.; Trygstad, T.; Pandit, N. *J. Colloid Interface Sci.* **1999**,

216, 34-40.

(29) De Lisi, R.; Lazzara, G.; Milioto, S.; Muratore, N. *J. Therm. Anal. Calorim.* **2007**, *87*, 61-67.

(30) Mouchid, A.; Delville, A.; Lambard, J.; LeColier, E.; Levitz, P. *Langmuir* **1995**, *11*.

(31) Mouchid, A.; Delville, A.; Levitz, P. *Faraday Discuss.* **1995**, *101*, 275-285.

(32) Willenbacher, N. *J. Colloid Interface Sci.* **1996**, *182*, 501-510.

(33) Pizzey, C.; Klein, S.; Leach, E.; Van Duijneveldt, J. S.; Richardson, R. M. *J. Physics: Condens. Matter* **2004**, *16*.

APPENDIX 3-A: Images of dispersions

Figure 3-A(a) shows the effect of increasing F127 from 0wt% to 10wt% with a 3wt% aqueous Laponite system and Figure 3-A(b) shows the macro scale suppression of gel formation using tube inversion

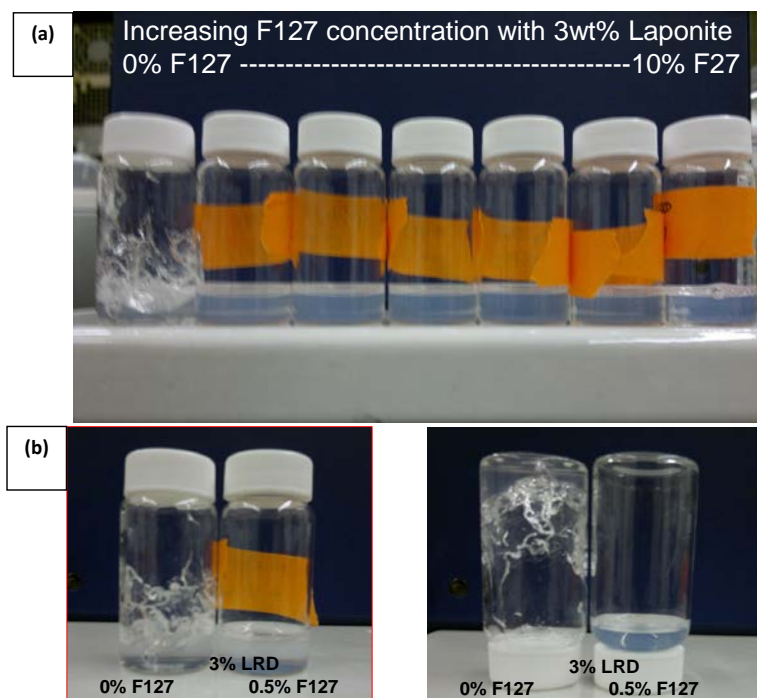


Figure 3- A Photographs illustrating 3wt% with various F127 concentrations

(a) dispersions produced to investigate effect of increasing F127 concentration in 3wt% Laponite concentration showing that adding F127 turns the solution cloudy; (b) Tube inversion showing the effect of adding 0.5wt% F127 to 3wt% Laponite dispersions.

CHAPTER 4

4. Thermo-responsive Laponite/F127 dispersions: Gelation and structure

4.1. Chapter overview

The following chapter builds on the hybrid clay/polymer dispersions introduced in Chapter 3 and the added functionality and responsive behavior due to the inherent properties of the components in the hybrid formulation are further explored. In particular, since Pluronic F127 exhibits a well-known temperature response, the work presented here focuses on understanding these thermally induced changes on both the structure and bulk properties of Laponite/Pluronic F127 dispersions and the ability to achieve on-demand bulk gelation. Variable temperature rheometry was used to monitor bulk temperature dependent changes in the system.

Microscopy results presented in Chapter 3 clearly illustrate changes in the structure depending on concentration. However, the need to dry the samples prior to imaging limits structural analysis especially when trying to understand temperature dependent effects. Here, structural analysis and temperature induced changes were studied using *in situ* synchrotron SAXS. The results presented here show the first quantified demonstration of the thermally induced structural changes and interactions between F127 and Laponite using synchrotron SAXS.

4.2. Introduction

Fluids such as colloids, emulsions, foams, polymers or surfactant solutions are often multiphasic materials. Significant effort has been devoted to the study of material structure and behaviors at different conditions to better understand the interactions within these systems¹⁻⁸. Recent work at low particle densities has shown that local arrested states are possible within the gel phase as a result of pair potential interactions⁹⁻¹¹. Due to

the complexity of these systems, studying the structural changes at the nanoscale and correlating these to bulk properties remains a key aspect to understanding the behavior of these systems.

Aqueous suspensions of Laponite provide an ideal model system and have been widely studied in the last decade ^{1-8, 12-17}. Several groups have also investigated the effect of adding surfactants ¹⁸⁻²⁶ on the phase diagram, gelation, aging behavior and structure of Laponite dispersions. De Lisi *et al.* ²¹ reported retarded gelation as a function of surfactant concentration while Schexnailder *et al.* ²⁷ studied the effect of heterogeneities in polyethylene oxide (PEO) hydrogels with crosslinked silicate nanoparticles. Zulian *et al.* ¹⁵ also noted retarded aging in the presence of surfactants. The interaction between Laponite particles and surfactants such as PEO and Pluronics has been reported using dynamic light scattering (DLS) and contrast matching in small angle neutron scattering (SANS) by Nelson and Cosgrove ¹⁸⁻²⁰ who show an increase of 3.78nm in radius and 3.45nm in thickness which they attributed to the formation of a polymer shell around the particles.

In this chapter, the structure and arrangement of the Laponite as well as Laponite/F127 aqueous dispersions (both liquid and gel) were probed using a variety of techniques including microscopy (SEM, AFM and TEM) and synchrotron small angle X-ray scattering (SAXS). Since Pluronic F127 is a thermo-responsive polymer with a well-known phase behavior, the thermal response of the system was also analyzed by variable temperature rheometry and *in situ* SAXS. It should be noted that, although aqueous F127 itself is well known to form a thermo-responsive micellar gel, the concentration used here is well below the typical gelation concentrations of aqueous F127 (> 10wt%) ^{24, 29, 31-34}.

4.3. Experimental Methods

Dispersions of Laponite and F127 in d-H₂O were prepared as described previously.

Rheology: Variable temperature rheology measurements of Pluronic F127 and F127/Laponite dispersions were conducted using an Ares rheometer (TA Instruments) with a Peltier attachment for temperature control. Variable temperature sweeps were performed in the range of 0°C-70°C at constant applied strain of 1% and oscillation frequency of 10rad/s as in the LVR (as determined in Chapter 3). A heating rate of 2°C/min was used for all experiments to allow structural rearrangement in the bulk to occur and a humidity cover was used to minimize evaporation at elevated temperatures for all experimental runs.

Synchrotron SAXS: Synchrotron SAXS experiments were conducted at Beamline X10A at NSLS I, Brookhaven National Labs using a beam energy of 11 KeV and camera length of 1.8m. The q -vector range was calibrated using a silver behenate standard. SAXS measurements of pure Laponite dispersions were first conducted to determine the average particle dimensions and organization. A Linkham THMS600 stage was used for temperature control to conduct *in situ* variable temperature-SAXS measurements. Samples were loaded using a 2mm thick annular stainless steel sample holder to ensure heat transfer within the probed temperature range of 0°C to 60°C and sealed with Kapton tape. A schematic of the sample loading setup is shown in Figure 4.1.

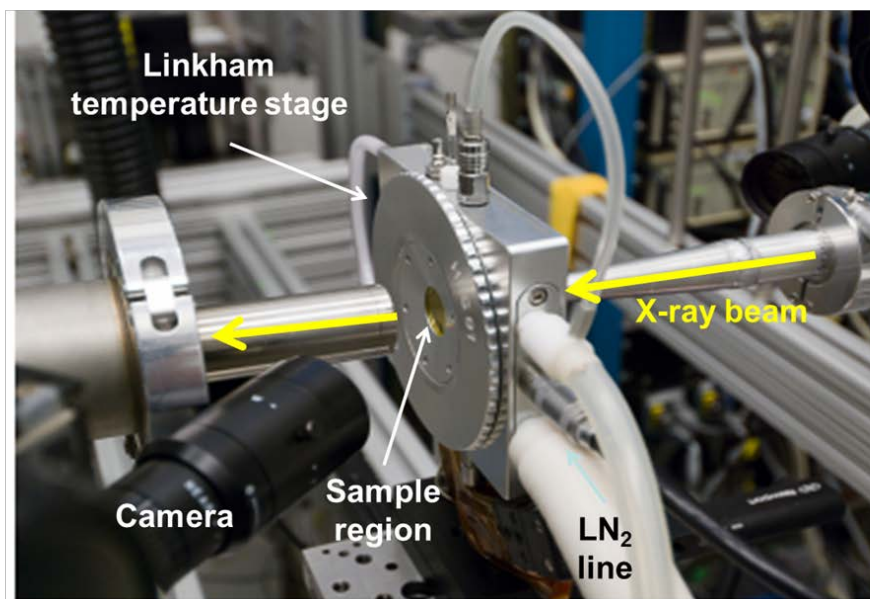
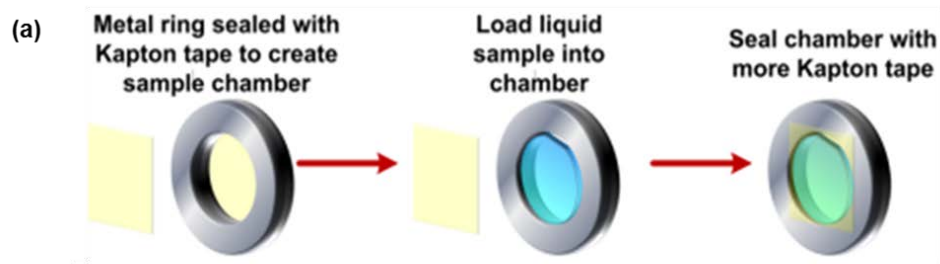


Figure 4.1 SAXS setup at Brookhaven National Labs.

Schematic of sample loading and experimental setup at Beamline X10A (NSLS) for temperature dependent SAXS of liquid and gel.

4.4. Results

Chapter 3 focused on the effects of adding Pluronic F127 to Laponite dispersions and subsequent changes in the gel formation. Here, the main focus is on demonstrating the ability to tune the response of the hybrid dispersion using the thermo-reversible behavior exhibited by F127 molecules and quantifying the structure in mixed Laponite/F127 dispersions.

Neat aqueous F127 dispersions are known to form thermo-reversible gels. At room temperature, concentrations >20wt% typically exist as a soft gel while lowering the F127 content to 10wt% causes the gelation temperature to increase to ~40°C. At < 5wt% F127, thermal gelation prior to evaporation can be completely suppressed^{28, 29}. Sun *et al.*

recently remonstrated that in the presence of Laponite however, this thermo-reversible gelation can be seen at much lower F127 concentrations³⁰.

Figure 4.2 shows an example of the bulk thermo-reversible gel at low F127 concentration of 3.6wt% and Laponite concentration of 3wt%.

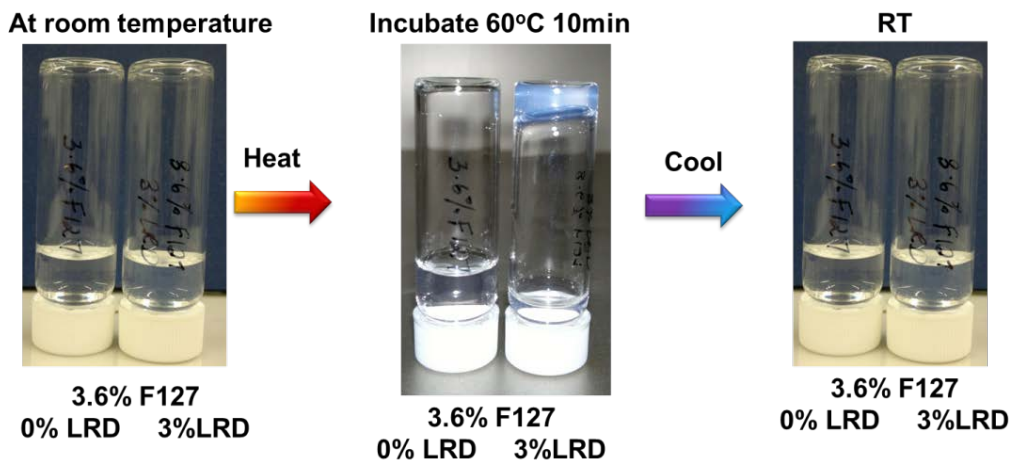


Figure 4.2 Thermo-reversible liquid to gel transition for 3.6wt% F127 with 3wt% Laponite.

4.4.1. Variable temperature rheometry

To quantify the thermally induced liquid to gel transition illustrated in the photographs in Figure 4.2, variable temperature rheology experiments were performed in the range of 0°C to 70°C for different F127 and Laponite concentrations. The evolution of G' was monitored over this temperature range. This work focuses primarily on three F127 concentration regimes:

- A low concentration regime of 3.6wt% F127 where the aqueous samples are known to form micelles but not a bulk gel (Figure 4.3)
- A medium concentration of 10wt% F127 known to form a soft gel at elevated temperatures but exists as a viscous liquid at room conditions (Figure 4.4(a))
- A high concentration of 25wt% F127 at which the samples exist as a bulk hard gel at room temperature (Figure 4.4(b)).

In each case, the effect of adding Laponite in the concentration range of 0.7-3wt% was investigated. The gelation kinetics and behavior were further quantified by applying a sigmoidal fit to the variable temperature measurements and the results of the fit are summarized in Table 4.1.

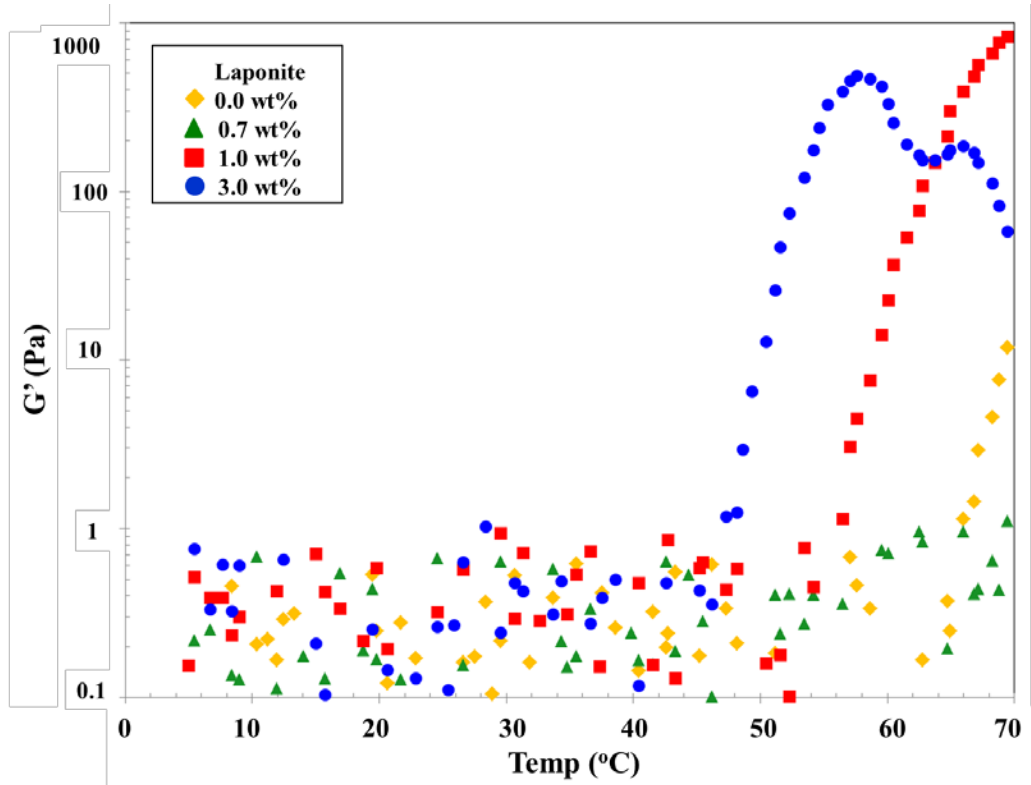


Figure 4.3 Temperature dependent G' for 3.6wt% F127 with Laponite.

The graph represents variable temperature sweeps within the LVE for 3.6wt% F127 dispersion with varying Laponite content of 0wt%, 0.7wt%, 1wt% and 3wt%.

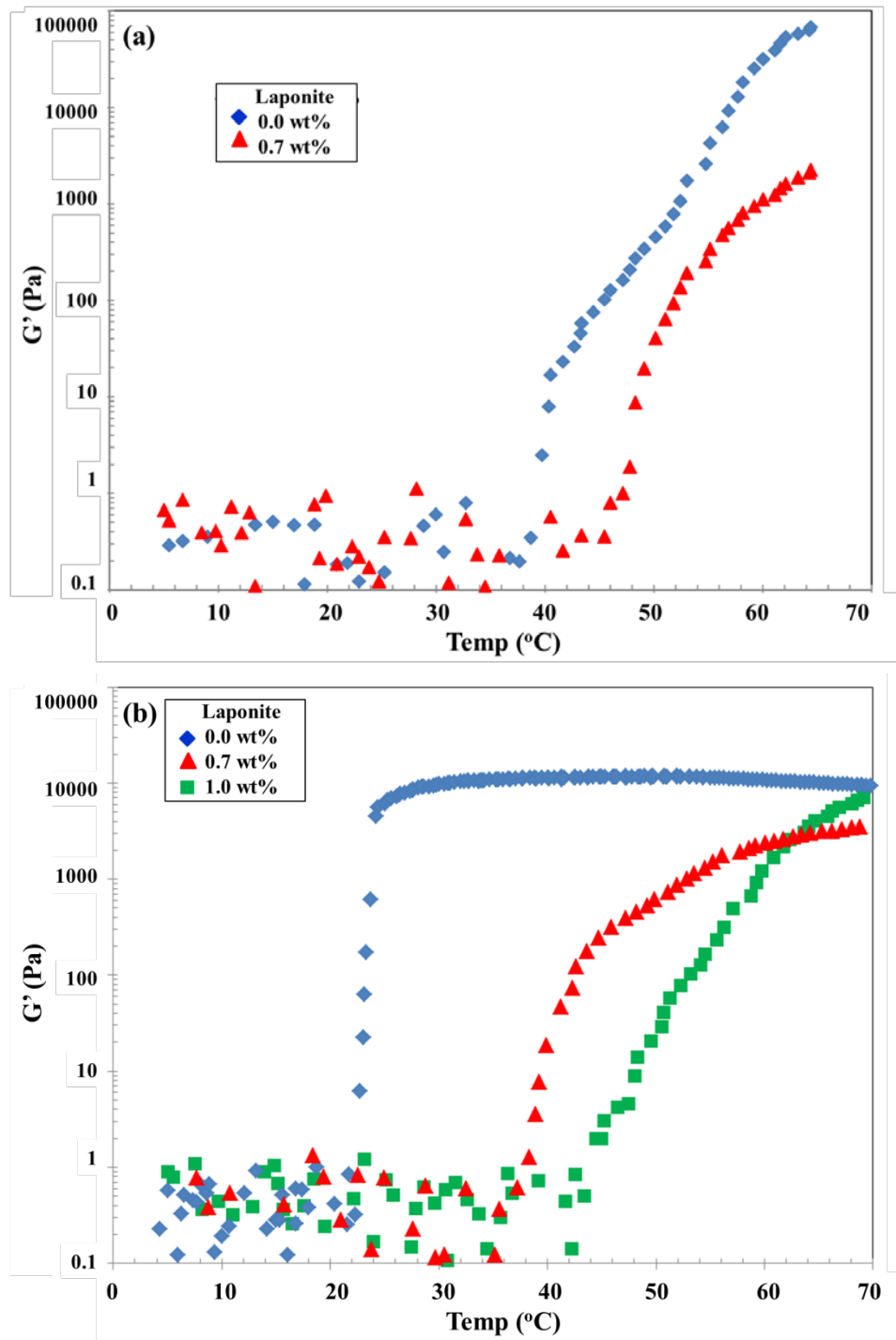


Figure 4.4 Effect of small Laponite additions to (a) 10wt% and (b) 25wt% F127.

The graphs show the behavior for (a) neat 10wt% F127 and with 0.7wt% Laponite while (b) shows the effect of adding 0.7wt% and 1.0wt% Laponite on 25wt%F127 dispersions.

F127 (wt%)	Laponite (wt%)	T _{gel} (°C) (onset)	Rate constant, x _o	Gelation Rate* (Pa/s)
3.6	0	n/a	n/a	n/a
	0.7	n/a	n/a	n/a
	1	56.7	1.43	0.335
	3	48.1	1.62	0.744
10	0	41.2	5.08	43.2
	0.7	47.9	1.99	2.29
25	0	22.7	0.474	93.2
	0.7	38.8	3.08	4.31
	3	36.2	2.74	5.13

Table 4.1 Summary of thermal gelation and fit parameters.

The results in each case can be summarized as follows:

- a) **3.6wt% F127 concentration with added Laponite:** Figure 4.3 shows the effect of different Laponite particle concentrations on the thermal response of 3.6wt% F127 as a function of temperature. With 0wt% and 0.7wt% Laponite, G' did not change in the range probed. As the Laponite concentration is further increased to 1.0wt% and 3.0wt%, a clear and distinct increase in the value of G' is observed. In both cases G' > G'', confirming gel formation. The gel formation temperature, defined as T_{gel}, decreased with increasing Laponite concentration. As shown in Figure 4.3, at 1.0wt% Laponite, T_{gel} occurs at 56°C while at 3.0wt% T_{gel} decreases to 48°C. The fit results show that increasing the Laponite content in 3.6wt% F127 dispersions decreases the temperature at which the liquid to gel transition starts while the rate of gelation, defined as the change in slope of G' per unit time, increases by a factor of 2.

At medium and high F127 concentrations of 10wt% and 25wt% respectively, the neat solutions exhibit thermal gelation. For these concentrations, the addition of Laponite was found to also affect both the onset temperature of gelation, gelation rate, as well as final gel stiffness.

- b) 10wt% F127 + 0.7wt% Laponite:** Figure 4.4(a) shows the variable temperature measurements for 10wt% F127 with 0wt% and 0.7wt% Laponite. As seen here, the presence of Laponite causes a delay in the initiation of gel formation and lowers the final gel stiffness. Table 4.1 shows that the presence of Laponite in 10wt% F127 delays the onset of gelation by 5°C and also produces a 20-fold decrease in the gelation rate measured.
- c) 25wt% F127 with added Laponite (0.7wt% and 1wt%):** Figure 4.4(b) shows the variable temperature measurements for 25wt% F127 with 0wt%, 0.7wt% and 1wt% Laponite added. In the absence of Laponite, 25wt% F127 exhibits a rapid gel formation at ~23°C as expected based on prior reports. With the addition of 0.7wt% Laponite, the temperature for the onset of gelation was delayed from ~23°C to ~38°C and further increase in Laponite content to 1wt%, shifts T_{gel} to ~42°C. The delay in gelation was accompanied with a decrease in gelation rate from ~93 Pa/s to ~5Pa/s.

The delay in gelation onset upon adding Laponite to 10wt% and 25wt% F127 points to two possible effects. First, the interaction between the polymer and particles result in a depletion of polymer concentration able to participate in gel formation as described by a reduction in micelle formation in Chapter 3. This is further supported by the TEM images presented in Figure 3.14 for drop cast and dried samples of pure 10wt% F127, pure 1wt% Laponite and a mixture of 10wt% F127 with 1wt% Laponite. The micrographs clearly show a suppression of micelle formation in the 10wt% F127 sample dried at room temperature upon adding 1wt% Laponite. Secondly, the lower value of G' at the end of gelation also points to potential defects in the quasi-crystalline structure of the F127 liquid crystal gel at 20wt%. At low F127 concentrations, the gel formation is directed exclusively by the interactions between the particles. In this case, the copolymer molecules serve primarily as a surfactant rather than as a micelle and gel forming component. Hence, increasing the particle concentration produces more effective inter-particle interactions and network formation resulting in larger G' values.

4.4.2. Structure in dispersions and gels

SEM and TEM images previously shown in section 3.4.5 of both drop-cast and lyophilized samples demonstrated significant dependence of structure on composition. However, limitations due to the sample preparation and high vacuum imaging requiring removal of any liquid in the system limit the ability to use these methods to determine dynamic temperature induced changes in these systems. Instead, small angle x-ray scattering (SAXS) experiments which can be conducted at ambient conditions using aqueous dispersions were carried out on a variety of samples. Finally, *in situ* variable temperature SAXS measurements were used to follow temperature induced changes during the gel formation.

I. Neat Laponite dispersions

The SAXS scattering profiles for aqueous Laponite dispersions at different concentrations are shown in Figure 4.5 and demonstrate two distinct behaviors as a function of the scattering vector, q . At intermediate and high values of q ($q > 0.2\text{nm}^{-1}$), the scattering intensity, $I(q)$, decays as a function of q^{-2} for all Laponite concentrations measured, a behavior consistent with the expected scattering from a dispersion of thin disk shaped particles with random orientation^{35, 36}. At low q -values ($< 0.2\text{nm}^{-1}$), $I(q)$ no longer follows q^{-2} with increasing concentration; instead the slope at small q -values exhibits a significant change consistent with particle aggregation suggesting structural arrangement and large scale organization^{27, 37}.

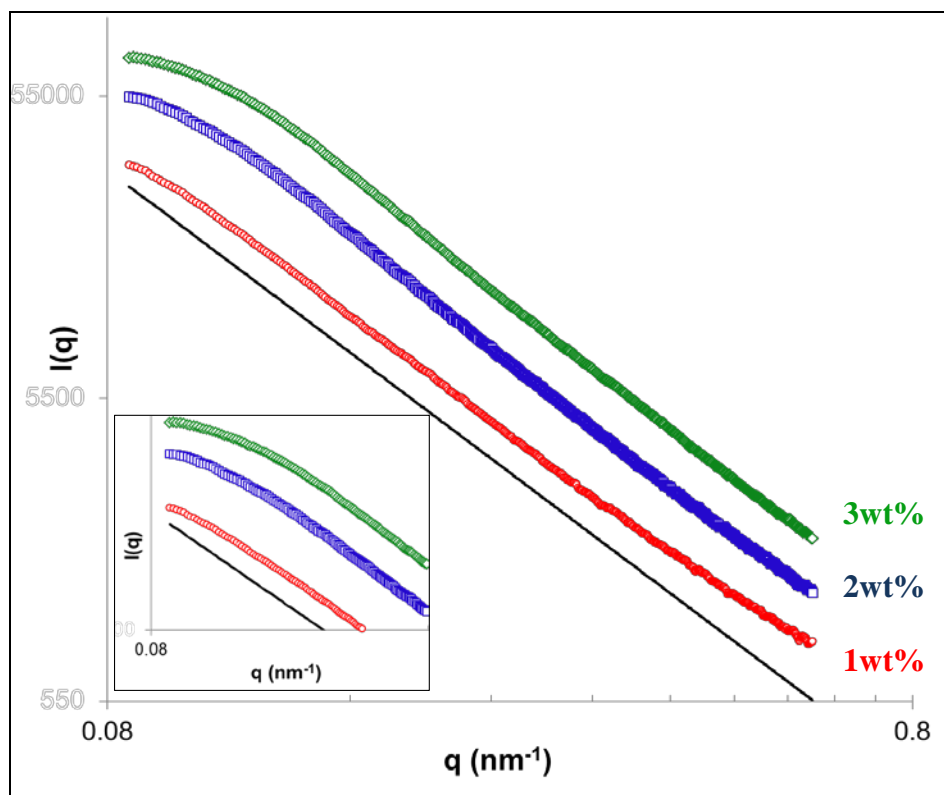


Figure 4.5 Room temperature SAXS plots for three different Laponite concentrations in water.

The solid line is the calculated form factor, $P(q)$, for a disk shaped particle with radius $\sim 13\text{nm}$ and $\sim 2\text{nm}$ thickness indicating that even at 1wt% concentration, Laponite particles exist as stacks of at least two individual particles. (inset) Low q scattering shows deviation from q^{-2} behavior as concentration increases.

II. *Thermo-responsive behavior of pure F127*

As shown earlier in Figure 4.3 and Figure 4.4, neat F127 exhibits a bulk change in viscosity indicating gel formation at high enough concentrations. The temperature dependent gelation is known to occur via aggregation and micellization as well as collapse of the PEO segments due to decreased solubility at high temperature. To investigate this behavior, first, the thermal response of neat F127 solutions heated from 0°C to 60°C at $2^{\circ}\text{C}/\text{min}$ was investigated. In addition to the *in situ* variable temperature SAXS measurements, samples were also lyophilized to directly image the room temperature structure and correlate the internal structure to the liquid and gel states as a function of sample concentration. These results are summarized in Figure 4.6.

At room temperature, in the low concentration regime (~3.6wt% F127), the aqueous dispersion typically exist as low viscosity liquids as a result of free PEO-PPO-PEO molecules. As the F127 concentration increases to 10wt%, the room temperature viscosity shows a corresponding increase although the dispersions maintain a fluid state. At higher F127 concentrations, free molecules coexist with micelles formed by aggregation of F127. The increase in viscosity is a result of inter-micellar interactions at the higher concentrations. When F127 concentration is further raised to 25wt%, aqueous F127 turns into a self-supporting gel at room temperature. This gel formation occurs as a result of higher micelle concentration such that steric interactions occur resulting in micelles arranged in a quasi-crystalline cubic lattice.

SEM images of samples prepared at room temperature and lyophilized are shown in Figure 4.6 (middle row) and confirm the increase in local order of aqueous F127 at room temperature with increasing concentration. As shown here, 3.6wt% F127, no evidence of ordering was apparent. Increasing concentration to 10wt% F127 produces a layered morphology while further increase to 25wt% F127 yields a relatively well-ordered porous structure.

In all cases, *in situ* SAXS data monitoring temperature induced changes show significant structural rearrangement. These spectra are shown in the bottom row of Figure 4.6. At low F127 concentration of 3.6wt% shown in Figure 4.6 (a), an increase in scattering intensity at low q -vector was observed when temperature was raised and is attributed to the formation of micelles as the F127 molecules aggregate such that the scattering objects change from extended chains into globular structures. At 10wt% F127 concentration, a broad peak is observed at $q \sim 0.32\text{nm}^{-1}$ and is attributed to the formation of a liquid cubic crystalline lattice with some disorder. As the concentration is further increased to 25wt%, this broad peak becomes sharper and more distinct indicative of increased order within the sample. The overall structure at each concentration was found to be consistent with prior SANS reports by Hecht and Hoffman⁴¹ as well as Hammouda *et al.*⁴²⁻⁴⁴.

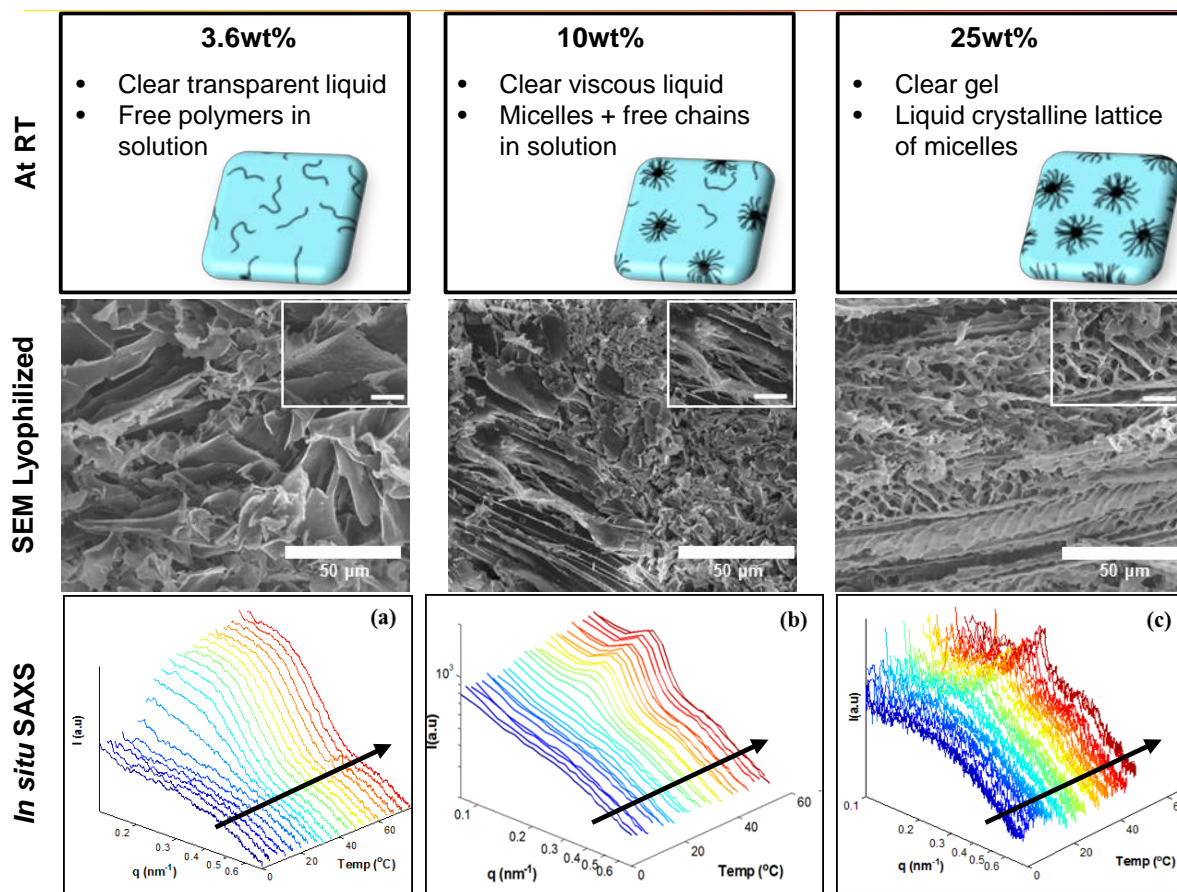


Figure 4.6: Summary of concentration and temperature effects on pure F127 solutions.

Top: Summary of physical appearance at RT. Middle: SEM of lyophilized samples prepared at RT. As shown here, increasing F127 concentration results in a transition from no order (3.6wt%) to well-ordered porous structure (25wt%). Bottom: *In situ* SAXS as a function of F127 concentration. As concentration increases, the samples become more ordered with well-defined peak indicating liquid crystalline ordering.

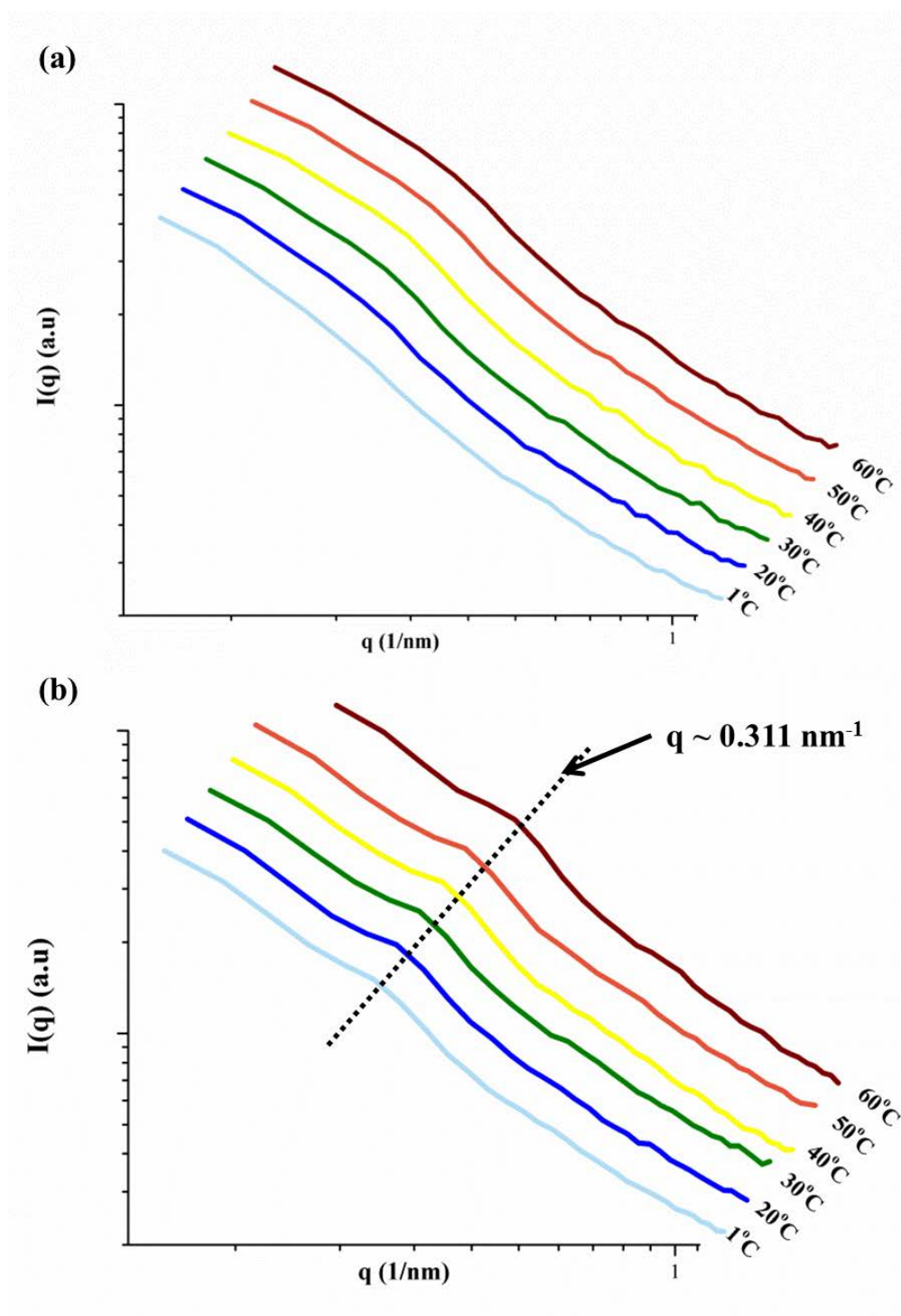
III. *Mixed Laponite/F127 dispersions*

Figure 4.7 shows the *in situ* SAXS spectra collected for different compositions of aqueous F127 and Laponite dispersions. In all cases, the presence of the Laponite nanoparticles, even at very low concentrations, results in a significant increase in the overall background scattering and a profile typical of pure Laponite dispersions as illustrated in Figure 4.5 was obtained. In all cases, the scattering from Laponite nanoparticles dominates the collected spectra due to the higher electron density of the inorganic nanoparticles.

The results shown in Figure 4.7 are summarized as follows for each composition:

- a) **0.7wt% Laponite + 6.8wt% F127:** As shown in Figure 4.7(a), in the presence of the Laponite in the dispersion, little to no change was observed in the scattering profile between temperatures of 0°C and 60°C.
- b) **0.7wt% Laponite + 17wt% F127:** As the concentration of F127 was increased from 6.8wt% to 17wt%, a small peak appeared at $q \sim 0.311 \text{ nm}^{-1}$. At 17wt% F127, the neat dispersions typically form a self-supporting gel similar to 25wt% F127 discussed in the previous section (Figure 4.6). Consequently, a strong temperature dependent peak corresponding to micelle ordering is expected, consistent with the peak shown for both neat 10wt% and 25wt% F127 dispersions shown in Figure 4.6. However as illustrated in Figure 4.7(b) here, with the addition of the Laponite into the system, this peak intensity is strongly suppressed (dotted line shows the peak position) due to stronger scattering from the inorganic Laponite nanoparticles.
- c) **3.6wt% F127 + 1wt% or 3wt% Laponite:** In the case of 3.6wt% F127 dispersions with either 1wt% or 3wt% Laponite shown in Figure 4.7(c) and (d), scattering from Laponite nanoparticles again completely dominates the spectra and no apparent changes occur with changing temperature. At 3wt% Laponite, the scattering $I(q)$ at small q increases with increasing temperature indicating the likely occurrence of aggregation or clustering of the particles into larger features.

However, this cannot be fully resolved due to the accessible q -range for SAXS experiments conducted at Beamline X10A (Brookhaven National Labs, NSLS I).



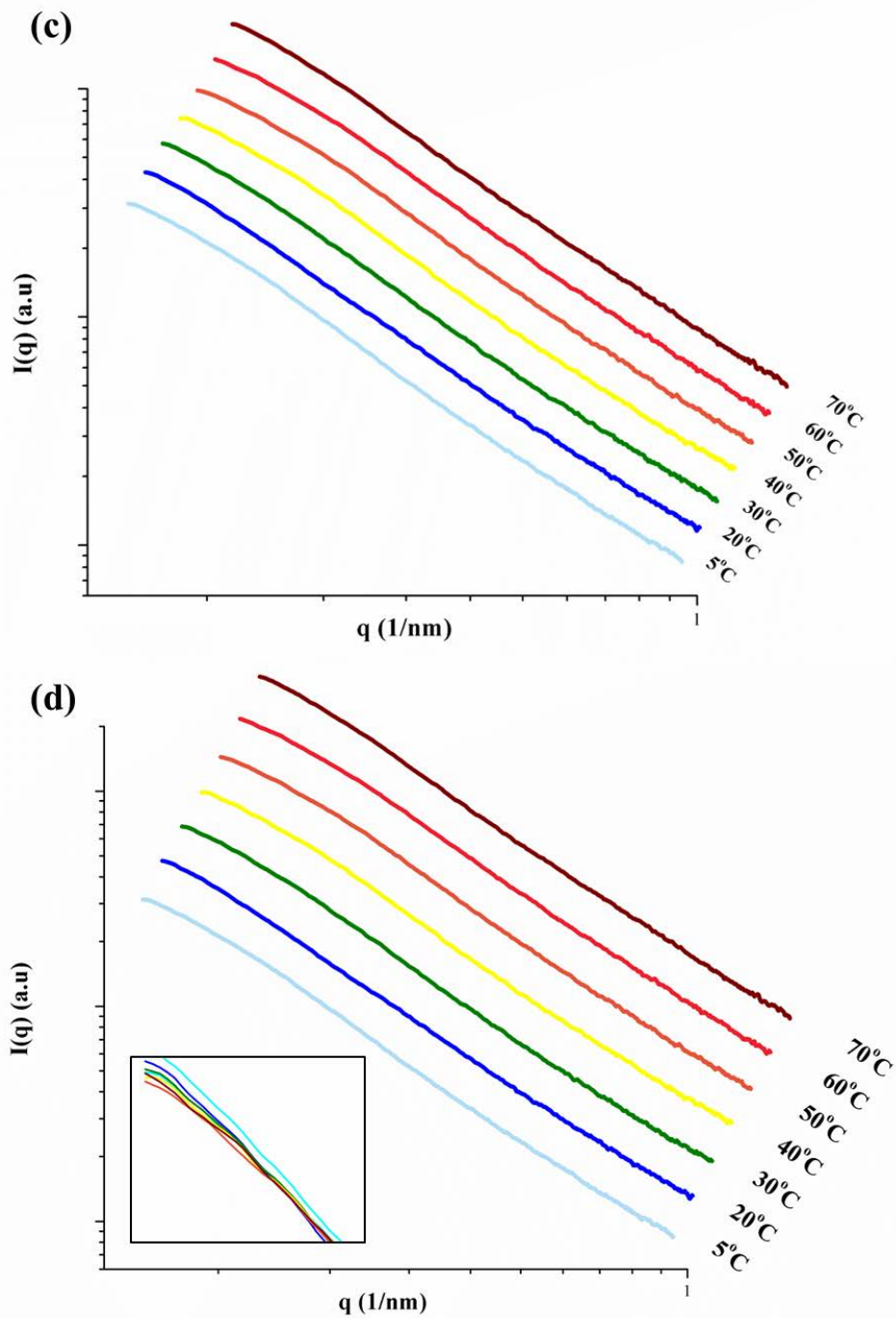


Figure 4.7 *In situ* temperature dependent SAXS for different Laponite/F127 dispersions.

(a) 6.8wt% F127 with 0.7wt% Laponite (b) 17wt% F127 with 0.7wt% Laponite (c) 3.6wt% F127 with 1wt% Laponite (d) 3.6wt% F127 with 3wt% Laponite. At higher F127 concentration of 17wt% as shown in (b) the presence of Laponite also appears to suppress crystalline ordering of the micelles. Inset in (d) shows changes at low q vector.

IV. Quantifying temperature induced changes in F127-Laponite from SAXS

As described in Chapter 2, scattering contributions during SAXS experiments depend on the electron density of the scattering material. In this case, Laponite has a much higher electron density than F127 and the Laponite scattering contribution can dominate the collected spectra even at low Laponite content. To quantify the structural changes taking place, the data analysis was conducted using two different methods depending on the Laponite concentration in the dispersion (low vs. high).

A. Low Laponite concentration regime (0.7wt%)

In the low concentration regime, the scattering profile from a neat Laponite dispersion can be modeled using only the form factor, $P(q)$, consistent with negligible inter-particle interactions between nanoparticles in a dilute suspension.

$$I(q) \propto P(q)_p \propto \left[\Delta\rho \cdot V_p \cdot \frac{\sin\left[\frac{qT(\cos\alpha)}{2}\right]}{\left[\frac{qT(\cos\alpha)}{2}\right]} \cdot \frac{2J_1[qR_p \sin\alpha]}{[qR_p \sin\alpha]} \right] \quad (4.1)$$

where $\Delta\rho$ = electron density difference between Laponite and medium (in this case H₂O), α = angle between scattering vector, q , and face of scattering particle, T = thickness of particles, R_p = radius of particles, and V_p = volume of scattering particle.

As seen in Figure 4.7 (a) and (b), in the presence of as little as 0.7wt% added Laponite, the scattering profile becomes heavily dominated by the particle scattering. Prior work using contrast matched SANS by Nelson *et al.*¹⁸⁻²⁰ has shown that Laponite/F127 interactions occur via the adsorption of F127 molecules onto the nanoparticle surface. The shape of the F127 coated Laponite particle can then be approximated as a simple core-shell structure consisting of a Laponite core and polymer shell shown schematically in Figure 4.8.

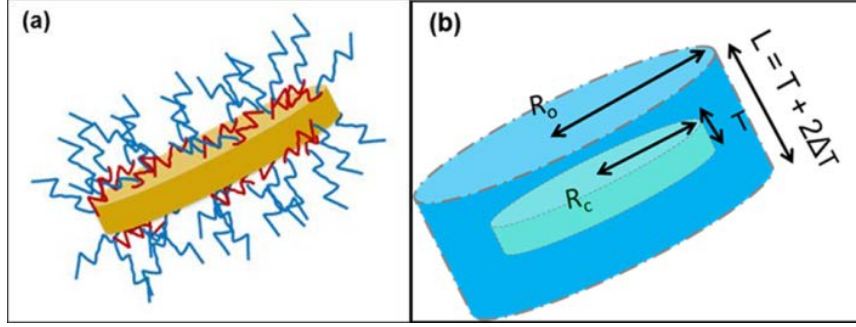


Figure 4.8 Schematic of Laponite/F127 core-shell structure.

(a) Laponite particle coated with F127 molecules and (b) example of core shell cylinder and dimensions for data fitting.

Since the dilute particle scattering contribution, $I(q)_{dil}$, can be measured separately and described simply as a function of the shape of the Laponite particle such that $I(q)_{dil} \propto P(q)_{lap}$, the scattering from the shell can be determined by subtracting $P(q)_{lap}$ from the overall $I(q)$. At low temperature, the form factor then becomes that of a core-shell cylinder as described in equation 4.2 below

$$\begin{aligned}
 P(q)_{CS} \propto & \left[\Delta\rho_1 \cdot V_c \cdot \frac{\sin \left[\frac{qT_c(\cos\alpha)}{2} \right]}{\left[\frac{qT_c(\cos\alpha)}{2} \right]} \cdot \frac{2J_1[qR_c \sin\alpha]}{[qR_c \sin\alpha]} \right] \\
 & + \left[\Delta\rho_2 \cdot V_{cs} \cdot \frac{\sin \left[\frac{q(T_c + 2\Delta T)(\cos\alpha)}{2} \right]}{\left[\frac{q(T_c + 2\Delta T)(\cos\alpha)}{2} \right]} \cdot \frac{2J_1[q(R_c + \Delta R)\sin\alpha]}{[q(R_c + \Delta R)\sin\alpha]} \right]
 \end{aligned} \tag{4.2}$$

The first term in equation 4.2 then accounts for the particle at the core of the cylinder while the second term accounts for the shell layer scattering. Here, $\Delta\rho_1$ = electron density difference between Laponite and F127, $\Delta\rho_2$ = electron density difference between water

and F127 shell, ΔT = increase in thickness, ΔR = increase in radius and V_{cs} = volume of core shell cylinder.

By subtracting the particle contribution and background scattering^I from the overall sample scattering, equation 4.2 reduces to the scattering contribution corresponding to a core-shell cylinder with a hollow core. The temperature dependent spectra for 0.7wt% Laponite with 6.8wt% F127 and 17wt% F127 generated after subtracting scattering from 0.7wt% Laponite are shown in Figure 4.9. This procedure enhances the spectral differences between each temperature shown for the different polymer concentrations which are otherwise non-obvious (Figure 4.7(a) and (b)). In both cases, the dispersions exhibit little to no order at low temperatures (evidenced by the lack of defined peaks) although increasing temperature results in clear spectral changes.

At the higher polymer concentration of 17wt%, the long range inter-micelle interaction peak at $q=0.31\text{nm}^{-1}$ becomes more apparent as the temperature is raised to 60°C. Figure 4.9(c) shows a direct comparison between the room temperature (28°C) SAXS scattering profiles from aqueous F127 at concentrations of 6.8wt% and 17wt%; the arrow indicates the stronger correlation peak evident at 17wt% F127 concentration.

Since F127 undergoes aggregation, micelle formation as well as collapse of the hydrophilic PEO chains⁴⁰⁻⁴⁴, the core-shell cylinder model described by equation 4.2 was applied to the data using a least squares regression method in SasView^{II}. In the case of the 17wt% F127 due to higher polymer content, a hard sphere interaction parameter

^IObtained by separately collecting SAXS spectra from 0.7wt% Laponite dispersions

^{II} This work benefitted from SasView software, originally developed by the DANSE project under NSF award DMR-0520547. Data fitting with the core - shell model was done using a built in model in SASView software package (<http://www.sasview.org/>) and a least squares regression for $q = 0.22 - 0.8\text{nm}^{-1}$. The core scattering was set equal to the background to account for a hollow core.

between scattering objects was also included in the calculation. The model fit assumes a uniform shell thickness around the particle and the results are discussed below.

Figure 4.10(a) depicts an example of the fit results obtained using a core-shell cylinder model with a hollow center for 17wt% F127 at room temperature while Figure 4.10(b) summarizes the fit results for both concentrations and temperatures. The core radius which corresponds to the size of the particle at the center of the core-shell scattering particle remained constant at ~12-13nm for all temperatures probed. The core thickness was extracted and found to be constant at ~2nm for all temperatures and both F127 polymer concentrations used providing additional evidence that the inorganic Laponite particle size does not undergo changes during heating. The values for the core dimensions correspond to a particle diameter of ~26nm corresponding to 2 particles stacked together at the center of each core-shell cylinder, indicating incomplete platelet separation.

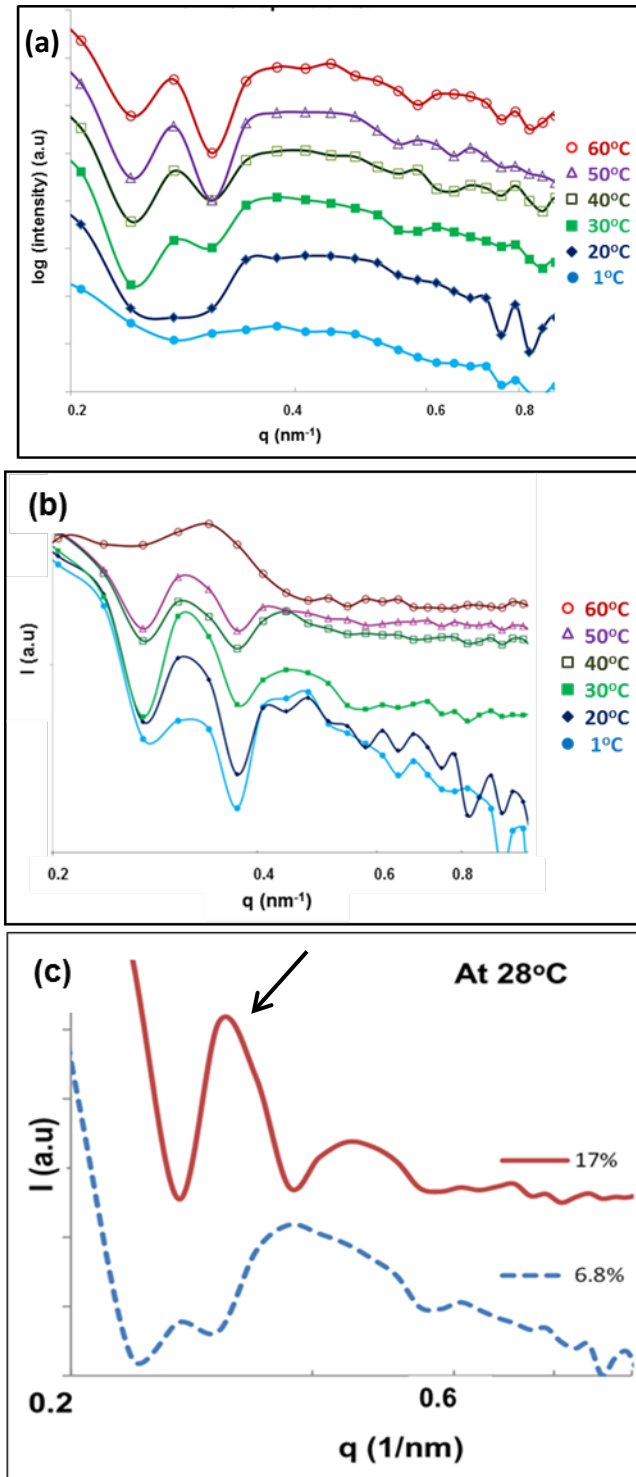


Figure 4.9 Variable temperature SAXS spectra after removing 0.7wt% Laponite scattering contribution.

(a) 6.8wt% F127 and (b) 17wt% F127 after spectral subtraction to remove the particle scattering contribution with the curves vertically offset for clarity. Panel (c) illustrates a direct comparison between 6.8wt% F127 and 17wt% F127 at 28°C with the arrow showing the peak arising from long range structure at higher F127 structure

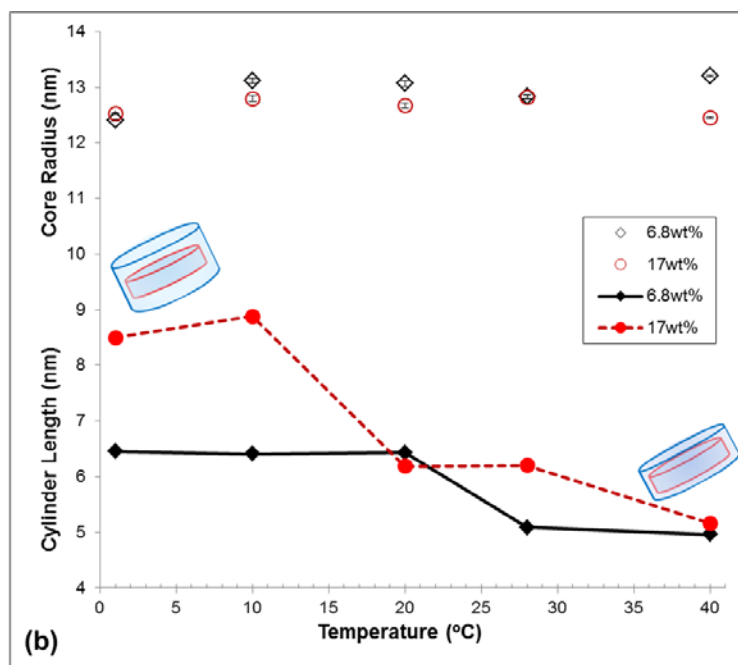
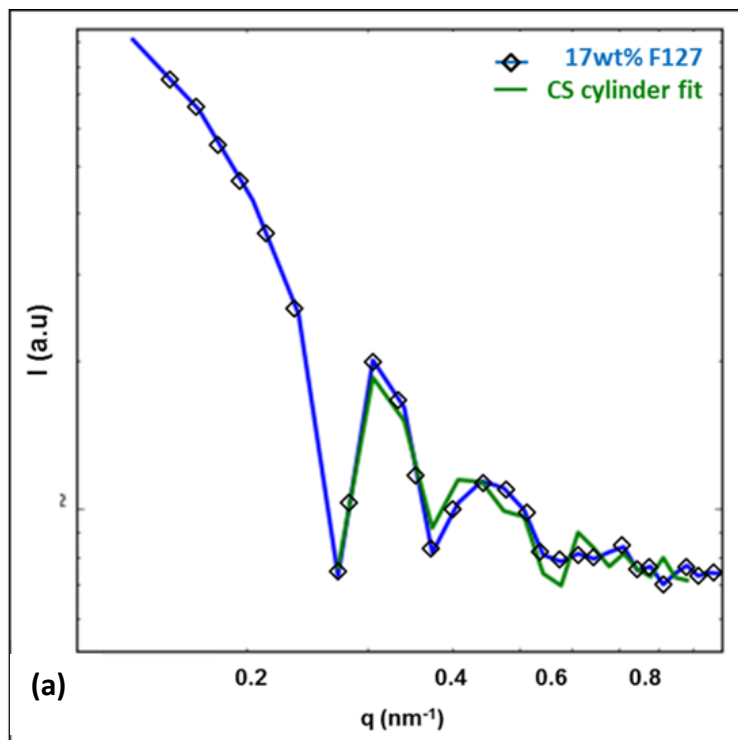


Figure 4.10 Fit results using a core-shell cylinder model.

(a) Example of least squares core shell model fit (green line) to room temperature scattering for 17wt% F127 (blue line with symbols). (b) Summary of fit results showing changes in the core radius (open symbols) and overall dimension of core-shell cylinder (solid symbols). The lines are meant as a guide and in both cases, the error bars are smaller than data points.

From the model fits, the overall size of the core-shell particle exhibits an overall decrease as the temperature is raised with an overall reduction in cylinder length from ~8.5nm to ~5nm with 17wt% F127 while aqueous 6.8wt% F127 solutions exhibit a change in cylinder length from ~6.5nm to ~5nm. Since the scattering cylinder depends on the Laponite particles with an adsorbed F127 shell, and the Laponite particle does not change with temperature, the overall size and shape of the scattering object then depends on the size of the F127 shell. Hence, the decrease in cylinder length indicates that the surface adsorbed F127 molecules undergo significant changes with increasing temperature. Since prior work has demonstrated that the PPO midblock adsorbs directly onto the Laponite faces, the change in shell thickness indicates that the PEO side blocks in the F127 molecules collapse and shrink as temperature increases.

From these fits, the average F127 polymer shell thickness was found to be on the order of 2-4nm, a value consistent with prior data from Nelson and Cosgrove using contrast matched SANS to determine an adsorbed layer thickness of 2.83-3.78nm¹⁸. The low temperature F127 shell thickness was found to be larger at higher F127 concentration and this is attributed to a larger number of free molecules likely present in the solution at 17wt%. Interactions and entanglements between these free molecules and the adsorbed chains can then lead to an overestimate of the shell thickness. The temperature dependent changes in shell thickness reported here are consistent with prior reports on the dehydration of the PEO block as temperature rises. This decrease in polymer thickness around the particles no longer effectively shields the inter-particle interactions such that the particles are able to interact with each other to form large scale aggregates big enough to scatter light visually. The particle aggregation also increases the sample viscosity resulting in cloudy gel seen in Figure 4.2. Figure 4.11 shows a schematic illustration of this temperature induced liquid to gel transition.

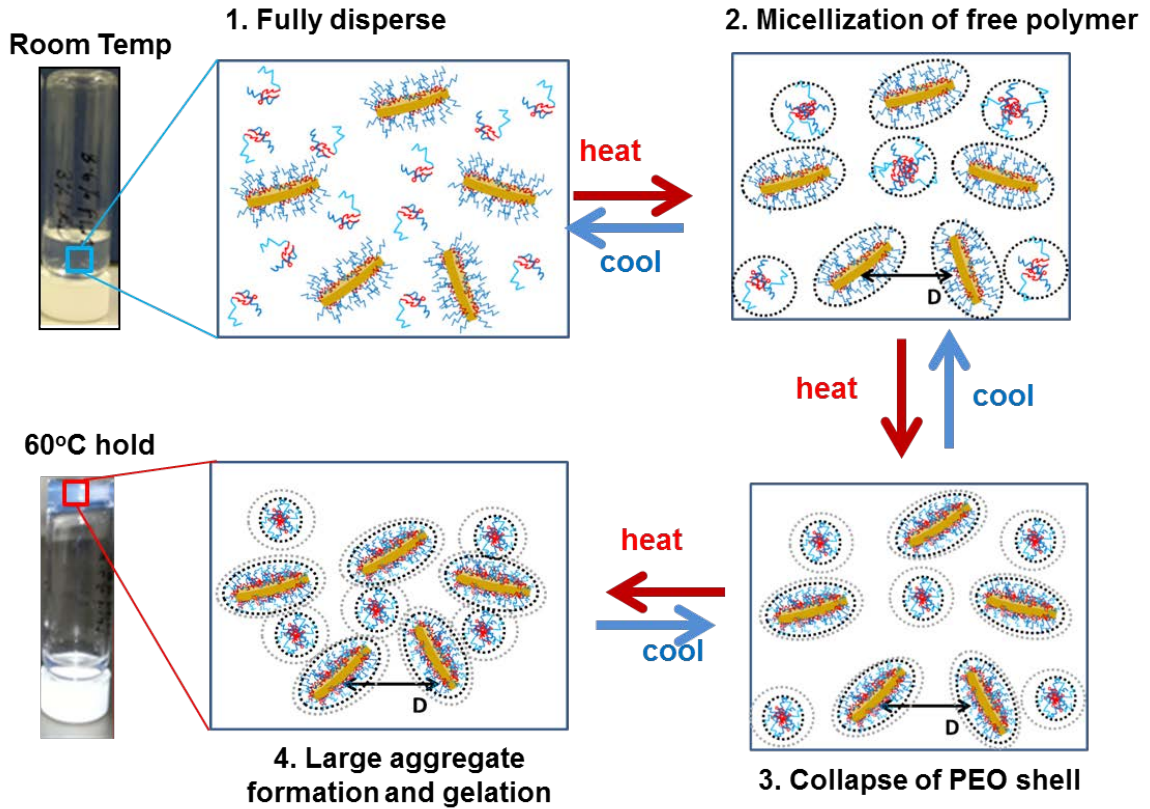


Figure 4.11 Schematic of changes in structure during thermal gel formation.

B. High Laponite concentration regime (3wt%)

For higher Laponite concentration dispersions, the particles are able to interact with each other and a structure factor contribution, $S(q)$, is present in the overall scattering intensity profile. Consequently, the collected data can no longer be analyzed by simply subtracting the low concentration scattering. Instead, an experimental structure factor, $S(q)_{expt}$ ^{38, 39}, can be used to describe the structural changes. Here, equation 4.3 shown below can be used to extract $S(q)_{expt}$ which can be plotted as a function of temperature.

$$S(q)_{expt} = \frac{I(q)_{conc}}{I(q)_{dil}} = \frac{I(q)_{conc}}{P(q)} \cdot \frac{C_{dil}}{C_{conc}} \quad (4.3)$$

Figure 4.12 depicts the changes in $S(q)_{expt}$ with increasing Laponite concentrations at room temperature using the data shown previously in Figure 4.5. As indicated here, a

peak in the structure factor curve is observed and the peak position shifts to higher q when Laponite particle concentration increases. These changes are consistent with calculated structure factor distributions reported by Ruzicka *et al.* for neat Laponite dispersions¹³ and peak position is attributed to a characteristic spacing, D^* , between scattering clusters in the sample given by:

$$D^* = 2\pi/q_{peak} \quad (4.4)$$

In the case of Laponite, these scattering clusters can consist of individual particles or several particles arrested in close proximity to each other as shown in the TEM images from Figure 3.13. The shift to higher q with increasing concentrations indicates that the clusters are closer to each other (30nm apart at 2wt% vs. 27.4nm apart at 3wt%). The values obtained are in good agreement with prior work on Laponite solutions containing large scale aggregates^{13, 18, 39}.

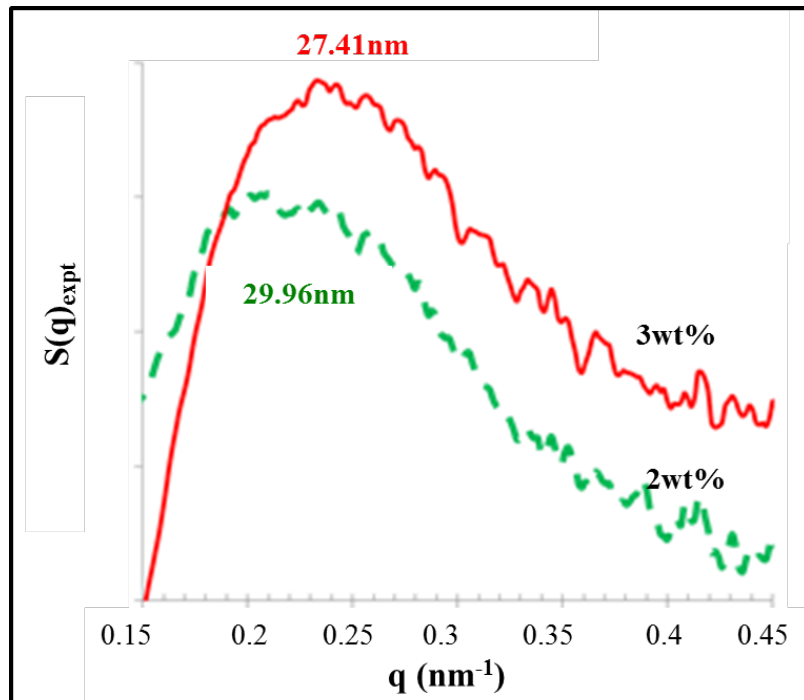


Figure 4.12 Experimental structure factor in neat Laponite dispersions.

Figure 4.13 summarizes the change in the characteristic spacing obtained from $S(q)_{\text{expt}}$ plots for a dispersion containing 3.6wt% F127 and 3wt% Laponite as a function of temperature. As expected, the characteristic spacing exhibits a measurable decrease from $\sim 27\text{nm}$ to $\sim 24\text{nm}$ as temperature was raised up to 70°C providing evidence for the formation of aggregated clusters. This is again consistent with the existence of extended PEO chains from the F127 side-arms at low temperature while the fast drop in spacing to $\sim 25\text{nm}$ observed at 30°C supports micelle formation via polymer aggregation and depletion (Figure 4.6).

The slower rate of decrease in the spacing D^* as temperature rises to 60°C is consistent with potential dehydration and subsequent collapse in the PEO chain keeping the scattering centers apart. The larger error bars obtained at high temperature occur as a result of peak broadening of $S(q)_{\text{expt}}$. This peak broadening is a characteristic feature of a glassy network within the gel where the clusters are under dynamic arrest and has been demonstrated in several natural clays underdoing the sol-gel transition with increasing concentration⁴⁶.

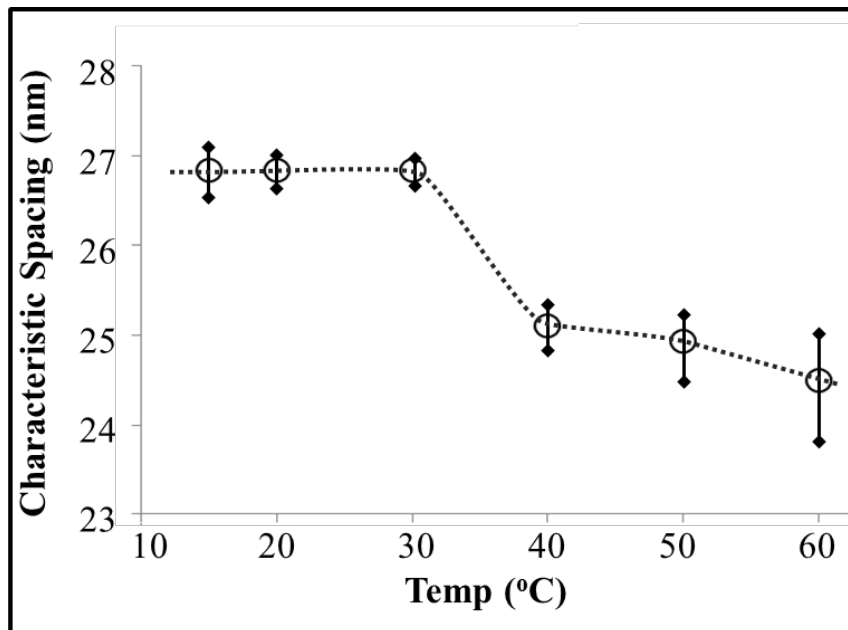


Figure 4.13 Temperature dependent characteristic spacing for 3wt% Laponite with 3.6wt% F127.

(The dotted line is drawn as a guide)

4.5. Conclusion

The work presented in this chapter shows that a well-defined thermally reversible liquid to gel phase transition occurs in both neat aqueous F127 and in different formulations containing both Laponite and F127. This phase transition was studied using both rheology and small angle x-ray scattering (SAXS) at room temperature as well as under variable temperature conditions.

At concentrations of 10wt% and 25wt%, liquid crystal structure and ordering as well as bulk gel formation was observed and attributed to micelle formation and subsequent interactions of these micelles with each other. As concentration of F127 decreases to 3.6wt%, the corresponding micelle concentration also decreases such that gelation no longer occurs at the low F127 concentrations. Subsequent addition of Laponite nanoparticles to aqueous F127 was found to have a significant effect on the thermal response of these dispersions.

At 3.6wt% F127, the addition of Laponite nanoparticles favors the formation of a thermal gel in the mixed dispersion; increasing the concentration of Laponite decreases the gelation onset temperature. However, for concentrations of 10wt% and 25wt% F127 which undergo thermal gelation in the neat state, the addition of Laponite instead caused a delay in the onset of gelation. Based on these effects, we determine that the presence of nanoparticles is required for network formation and subsequent gelation in the case of dilute F127 solutions well below the micellar gel forming concentration while at higher F127 concentrations the Laponite particles likely act as defects preventing effective micelle formation. Further, the difference in behavior indicates that the gels created likely have a different structural arrangement. In the presence of Laponite, at low F127 concentrations, gels likely form via particle aggregation and rearrangement; on the other hand, at high F127 concentration, the micellization of free F127 and subsequent interactions of these micelles dominate the gelation process.

Results from the *in situ* variable temperature SAXS experiments clearly demonstrate the changes and ordering in neat F127 at the three concentrations. Upon adding Laponite particles, the temperature dependence of the aqueous dispersions was no longer evident. Furthermore, the characteristic peak at $q \sim 0.311\text{nm}^{-1}$ for the micelle interactions was suppressed indicating decreased micelle ordering and reduced liquid crystalline order. Data analysis at low particle concentration showed that the adsorbed polymer shell thickness decreased as temperature was raised. Finally, by plotting the experimental structure factor parameter, $S(q)_{\text{expt}}$, from the collected $I(q)$ scattering data, the characteristic spacing, D^* , between scattering clusters was obtained. The data indicates that D^* decreases with temperature and confirms aggregation of particles into clusters as the temperature was raised.

The results presented in this chapter are a first demonstration of the changes in both the F127 shell thickness and the decrease in characteristic cluster spacing with temperature determined using *in situ* variable temperature synchrotron SAXS measurements.

4.6. References

- (1) D. Bonn, H. Tanaka, G. Wegdam, H. Kellay, and J. Meunier, *Eur. Letters (EPL)*, **1999**, 45, 52-57.
- (2) H. Tanaka, J. Meunier, and D. Bonn, *Phys. Rev. E*, **2004**, 69, 1-6.
- (3) A. Mourchid, A. Delville, J. Lambard, E. Lecolier, and P. Levitz, *Langmuir*, **1995**, 11, 1-9.
- (4) P. Levitz, E. Lecolier, A. Mourchid, A. Delville, and S. Lyonnard, *Eur. Letters (EPL)*, **2004**, 49, 672-677.
- (5) B. Ruzicka, L. Zulian, and G. Ruocco, *Philosophical Magazine*, **2007**, 87, 1-11
- (6) B. Ruzicka and E. Zaccarelli, *Soft Matter*, **2011**, 7, 1268-1286.
- (7) B. Ruzicka, L. Zulian, R. Angelini, M. Sztucki, and G. Ruocco, *Phys. Rev. E*, **2008**, 77, 1-4.
- (8) B. Ruzicka, L. Zulian, E. Zaccarelli, R. Angelini, M. Sztucki, A. Moussaïd, and G. Ruocco, *Phys. Rev. Lett.*, **2010**, 104, 85701.
- (9) A. Fortini, E. Sanz, and M. Dijkstra, *Phys. Rev. E*, **2008**, 78, 1-8.
- (10) A. Fortini, M. Schmidt, and M. Dijkstra, *Phys. Rev. E*, **2006**, 73, 1-16.
- (11) B. Ruzicka, L. Zulian, and G. Ruocco, *Journal of Phys.: Cond. Matter*, **2004**, 16, S4993
- (12) B. Ruzicka, L. Zulian, and G. Ruocco, *Journal of Phys.: Cond. Matter*, 16, **2004**, 1-11.
- (13) B. Ruzicka, E. Zaccarelli, L. Zulian, R. Angelini, M. Sztucki, A. Moussaïd, T. Narayanan, and F. Sciortino, *Nature Materials*, **2010**, 10, 1-5.
- (14) H. A. Baghdadi, H. Sardinha, and S. R. Bhatia *Journal Of Polymer Science Part B: Polymer Physics* **2005**, 43, 233-240
- (15) L. Zulian, B. Ruzicka, and G. Ruocco, *Philosophical Magazine*, **2008**, 88, 1-10.
- (16) A. Shahin and Y. Joshi, *Phys. Rev. Lett.*, **2006**, 106
- (17) A. Shahin and Y. M. Joshi, *Langmuir*, **2012**, 28, 5826-5833.
- (18) A. Nelson and T. Cosgrove, *Langmuir*, **2004**, 20, 2298-304.
- (19) A. Nelson and T. Cosgrove, *Langmuir*, **2004**, 20, 10382-8.
- (20) A. Nelson and T. Cosgrove, *Langmuir*, **2005**, 21, 9176-82.
- (21) R. de Lisi, M. Gradzielski, and G. Lazzara, *The Journal Of Phys. Chem. B* **2008**, 112, 9328-9336.
- (22) Q. Jin, P. Schexnailder, A. Gaharwar, and G. Schmidt, *Macromolecular Bioscience*, **2009**, 9, 1028-1035.
- (23) S. Morariu and M. Bercea, *Journal Of Chem. & Eng. Data* **2008**, 54, 54-59.
- (24) I. Boucenna, L. Royon, and P. Colinart, *Journal Of Thermal Analysis And Calorimetry* **2009**, 98, 119-123.
- (25) J. R. de Bruyn, F. Pignon, E. Tsabet, and A. Magnin, *Rheologica Acta* **2008**, 47, 1-11.
- (26) P. Mongondry, T. Nicolai, and J. F. Tassin, *Journal Of Colloid And Interface Science* **2004**, 275, 191-196.
- (27) K. A. Juggernaut, A. E. Gros, N. A. Mezmarich, and B. J. Love, *Soft Matter* **2011**, 7, 10108-10115.
- (28) P. Alexandridis, J. F. Holzwarth, and T. A. Hatton, *Macromolecules*, **1994**, 27, 2414-2425.

- (29) K. Mortensen and J. S. Pedersen, *Macromolecules*, **1993**, 26, 805-812.
- (30) K. Sun and S. R. Raghavan, *Langmuir*, **2010**, 11, 26, 8015-8020.
- (31) von Lenaerts, C. Triqueneaux, M. Quartern, F. Rieg-Falson, and P. Couvreur, *International Journal Of Pharmaceutics* **1987**, 39, 121-127.
- (32) J. Gilbert, C. Washington, M. Davies, and J. Hadgraft, *International Journal Of Pharmaceutics*, **1987**, 40, 93-99.
- (33) D. Attwood, J. Collett, and C. Tait, *International Journal Of Pharmaceutics*, **1985**, 26, 25-33.
- (34) N. A. Meznarich, K. A. Juggernaut, K. M. Batzli, and B. J. Love, *Macromolecules*, **2011**, 44, 7792-7798.
- (35) J. D. Ramsay, S. W. Swanton, and J. Bunce, *Journal Of The Chemical Society, Faraday Transactions* **1990** 86, 3919-8.
- (36) J. D. Ramsay and P. Lindner, *Journal Of The Chemical Society, Faraday Transactions*, **1993**, 89, 4207-9.
- (37) P. Schexnailder, E. Loizou, L. Porcar, P. Butler, and G. Schmidt, *Phys. Chem. Chem. Phys.*, **2009**, 11, 1-7.
- (38) A. Loiseau and J. F. Tassin, *Macromolecules*, **2006**, 39, 9185-9191.
- (39) M. Morvan, D. Espinat, J. Lambard, and T. Zemb, *Colloids And Surfaces A: Physicochemical And Engineering Aspects* **1994**, 82, 193-203.
- (40) J. M. Saunders, J. W. Goodwin, R. M. Richardson, and B. Vincent, *The Journal Of Phys. Chem. B*, **1999**, 103, 9211-9218.
- (41) E. Hecht and H. Hoffmann, *Tenside, Surfactants, Detergents*, **1998**, 35, 185-199 .
- (42) B. Hammouda, D. Ho, D. Ho, and S. Kline, *Macromolecules*, **2002**, 35, 8578-8585.
- (43) B. Hammouda, D. L. Ho, and S. Kline, *Macromolecules*, **2004**, 37, 6932-6937.
- (44) B. Hammouda and D. L. Ho, *Journal Of Polymer Science Part B: Polymer Physics*, **2007**, 45, 2196-2200.
- (45) C. Pizzey, S. Klein, E. Leach, JS, Van Duijneveldt, RM Richardson, *Journal of Phys.: Cond. Matter*, **2004**, 15, 16, 2479.
- (46) E. Paineau, I. Bihannic, C. Baravian, A-M. Philippe, P. Davidson, P. Levitz, S.S. Funari, C. Rochas, and L.J. Michot, *Langmuir*, **2011**, 27 5562-5573.

APPENDIX 4-A: Details of log –Boltzmann Sigmoidal mathematical fit

Overview of log Boltzmann sigmoidal fit to quantify thermogel formation.

A log-Boltzmann sigmoid model was applied to the temperature dependent rheology data to quantify the gelation kinetics of the F127 containing samples. Equation 4-A describes the model fit used where t_0 denotes the inflection temperature, the temperature at which the complex viscosity has reached halfway between its initial and final values. Figure 4-A illustrates a representative Boltzmann sigmoid curve and illustrates the four relevant fitting parameters: η_0 , η_f , t_0 , and Δt .

$$\log \eta^*(t) = \log(\eta_f) + \frac{\log(\eta_0) - \log(\eta_f)}{(1 + e^{\frac{t-t_0}{\Delta t}})} \quad (\text{Equation 4-A})$$

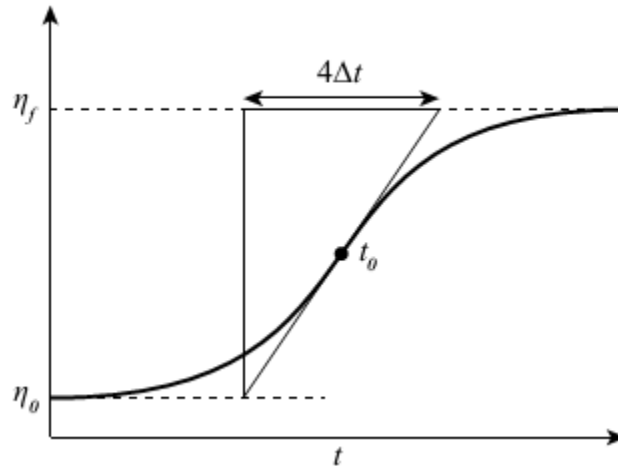


Figure 4- A Schematic of the log Boltzmann sigmoidal model curve showing the relevant parameters.

CHAPTER 5

5. *In situ* photogelation kinetics of Laponite nanoparticle-based photorheological dispersions

5.1 Chapter summary

Chapters 3 and 4 focused on the thermoresponsive behavior of F127/Laponite aqueous dispersions and showing that this response can be characterized at the bulk scale as well as at the microstructural levels. While the thermal response described in Chapter 4 has several advantages such as reversibility as well as a large tunable space by simply formulating dispersions appropriately, the need to apply heat can have limitations on potential applications where liquid to gel phase transitions and irreversible changes at constant temperature is needed. The current chapter explores the use of UV light to tune the gelation of F127/Laponite systems using a formulation based approach where a UV light activated reaction triggers gel formation. This chapter looks in particular at understanding the factors that affect the UV induced photogelation kinetics utilizing a commercially available photo-acid generator.

5.2 Introduction

Over the past decade, there has been increasing interest in stimuli-responsive fluids and other materials, whose properties can be influenced by external factors including electric fields, magnetic fields and, of increasing interest, light¹⁻⁷. Stimuli responsive fluids where exposure to different wavelengths of light produces a change in viscosity are referred to as photorheological (PR) fluids⁸ and have generated a large amount of interest due to a myriad of possible applications in flow sensors and microfluidic devices⁹.

The main challenge in developing PR systems has been the synthesis of novel light sensitive molecules¹⁰⁻¹² as evidenced by the work of Wolff *et al.* on the photorheological

effects in micelle solutions based on light sensitive anthracene derivatives⁸ and by Sakai *et al.* on azobenzene modified cationic surfactants to produce reversible changes in viscosity using light². In recent years, development of PR fluids requiring less involved synthesis has generated more interest in this field. In the last decade, there have been reports on a series of photogelling system formulations including zwitterionic worm-like micelles¹³, cationic surfactant solutions with a photosensitive acid or salt⁹, as well as dispersions containing synthetic nanoparticles combined with a surfactant and photoactive acid generator¹⁴.

While the dynamic driving force for gel formation in these nanoparticle-based PR systems has been established as a structural rearrangement of the dispersion components, little is known about the kinetics of gelation. To further understand and explore these systems, we have conducted a set of *in situ* photorheological experiments focusing on a Laponite-containing PR fluid recently reported by Sun *et al.*¹⁴.

The nanoparticle-based PR fluid dispersion in this work consists of Laponite nanoparticles formulated with F127 as well as a commercially available photoactive acid generator (PAG), diphenyliodonium-2-carboxylate monohydrate. The PAG is the photoactive component and, upon UV irradiation, undergoes photolysis to generate benzoic acid and iodobenzene reducing the pH from ~9 to ~7. According to the proposed photogelling mechanism¹⁴, the photolysis of the PAG causes the F127 desorb from the surface of the Laponite particles while the pH drop induces the generation of surface charges on the Laponite nanoparticles^{18, 19}. To minimize electrostatic repulsions, the Laponite nanoparticles rearrange in an edge to edge or face to edge structure within the solution and producing a gel (Figure 5.1).

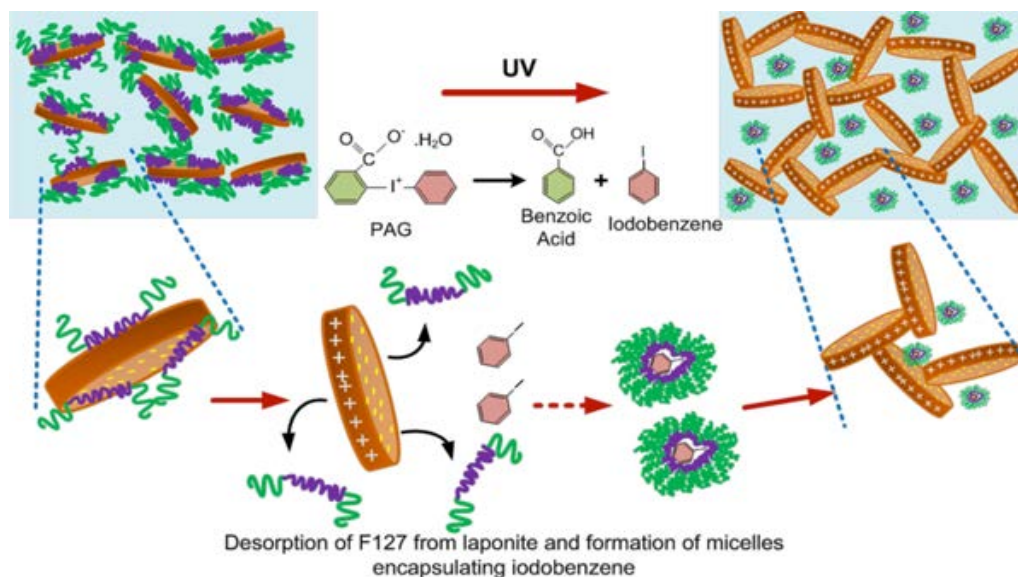


Figure 5.1 Schematic of photogelation mechanism (adapted from Sun et al.¹⁴)

The rest of this chapter focuses on further understanding the gelation mechanism and interactions within the system with a particular emphasis on the kinetics leading to gel formation. The primary goal of the current chapter is to understand gelation kinetics and establish a foundation for future intelligent design of Laponite nanoparticle-based PR fluids.

5.3 Experimental Methods

Formulation: Dispersions of Laponite and F127 were prepared in d-H₂O as described in Chapter 3. To prepare the formulations for photorheology studies, desired amounts of the PAG were then added to achieve final solution compositions spanning 0-10wt% F127, 0-4wt% Laponite and 5-20mM PAG. To ensure complete dissolution of both F127 and PAG as well as uniform distribution of Laponite nanoparticles, all dispersions were stirred overnight prior to use. All samples containing the PAG were isolated from ambient light to preserve the integrity of the chemical compound.

DSC: Differential scanning calorimetry (DSC) was performed using a Q2000 series DSC (TA instruments, DE) and hermetically sealed aluminum pans to suppress evaporation endotherms. Different formulations were investigated both before and after UV

irradiation. 10 mg of sample was placed into a DSC pan and hermetically sealed. To determine the effect of UV exposure on the dispersions, DSC pans containing the dispersions were exposed to UV at an intensity of $150\text{mW}/\text{cm}^2$ for 10min. The UV treated pan was then weighed again to account for possible evaporation during the irradiation process followed by hermetic sealing. In all cases, UV exposure was found to cause less than 0.2mg of mass loss attributed to evaporation of water. All DSC experiments were carried out at a heating rate of $5^\circ\text{C}/\text{min}$ from 0°C to 80°C .

Photorheology: Rheometry measurements were conducted on an ARES rheometer (TA Instruments, DE) in parallel plate geometry. For each formulation, initial complex viscosity measurements were carried out using a dynamic frequency sweep test between 1-15 rad/s at 0.05 rad/s increments. A PhotoCuring Accessory (TA instruments, DE) equipped with a high pressure mercury lamp ($\lambda = 320\text{-}500\text{nm}$) was fitted to the ARES rheometer and a transparent acrylic plate was used as the top plate for *in situ* photorheology experiments. To ensure constant UV intensity during the experiments, the lamp was turned on at least 30 minutes prior to calibrating the intensity at the sample surface. Variation in UV intensity across the sample surface was no greater than 10% as determined by calibration measurements at five different locations. All experiments were conducted with a gap size of $< 1.2\text{mM}$ to ensure uniform UV exposure throughout the sample and minimize the effect of thickness variations on the absorption of UV light.

Experiments investigating the effect of dispersion formulations on gelation behavior were conducted at constant UV intensity of $150\text{mW}/\text{cm}^2$. Separately, the effect of UV intensity on the photogelation kinetics was explored for fixed sample composition by varying the intensity measured at the sample surface between $100\text{-}150\text{mW}/\text{cm}^2$. Oscillatory shear tests were conducted at fixed strain of 5% and frequency of $10\text{rad}/\text{s}$ to monitor the evolution of the complex viscosity under minimal sample deformation. Initiation of UV exposure occurred 60 seconds after the onset of data collection. All experiments were conducted at ambient conditions to eliminate temperature effects. An additional dynamic frequency sweep was conducted at the end of the photogelation process to confirm that

the shear test parameters of 5% strain and 10rad/s were within the linear viscoelastic regime of the final gel produced.

Structure analysis: To determine the effect of both PAG addition and UV irradiation on the microstructure, SEM images of lyophilized samples with the PAG were analyzed before and after irradiation. Temperature dependent SAXS experiments as described in Chapter 4 were also conducted on irradiated samples to determine the thermal stability of the photo gel. Samples for SAXS were prepared as described previously; to prepare gels, the dispersions were loaded into the metal washer followed by UV irradiated to form the gel phase prior to being sealed.

5.4 Results

5.4.1 Effect of composition and UV exposure on calorimetric behavior

Differential Scanning Calorimetry (DSC) has been widely used to investigate the micellization in a variety of Pluronic materials²¹⁻²⁵. Several groups have investigated the influence of various particles on the micellization of these block copolymers. Lin and Alexandridis²⁶ probed the adsorption of F127 onto carbon black particles while De Lisi *et al.*²⁷ studied the effect of Laponite particles in both homopolymer and several commercially available triblock copolymers. Boucenna *et al.*²⁸ recently reported that the addition of low concentrations of Laponite (1-4wt%) to a 17wt% F127 solution has little to no effect on the micelle formation of the F127 solution. In each of these studies, the surfactant concentration investigated was >10 %. The current study probes the effect of sample composition as well as UV treatment on the micelle formation in complex solutions at F127 concentration of less than 10wt%.

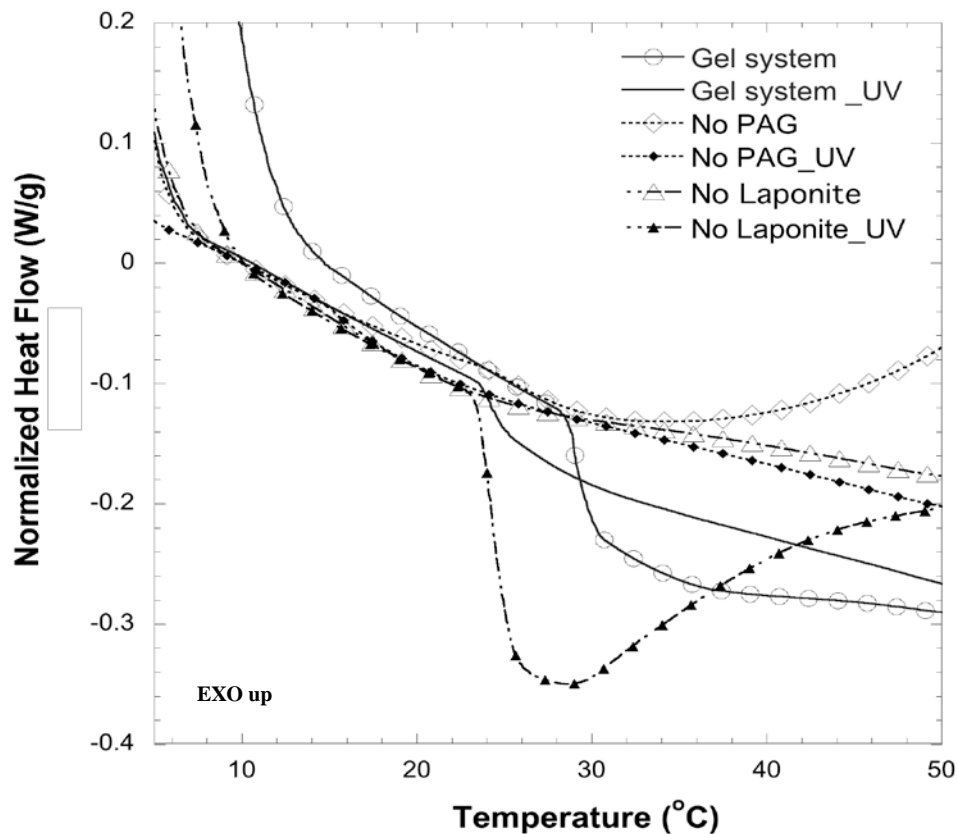


Figure 5.2 Representative DSC thermograms.

The data illustrates changes in the micellization endotherm as a function of sample composition and UV exposure. (*Gel system* = 3.6wt% F127, 3wt% Laponite and 13mM PAG, *No Laponite* = 3.6wt% F127 and 13mM PAG and *No PAG* = 3.6wt% F127 and 3wt% Laponite)

Figure 5.2 shows DSC thermograms obtained for different compositions before and after UV exposure. The presence of Laponite and/or PAG in the aqueous F127 solutions was found to affect the thermodynamics of F127 micelle formation as evidenced by the changes observed in the micellization endotherm. To quantify the DSC results, the temperature for the onset of micellization, T_{OM} , and the total enthalpy change, ΔH , during micelle formation were compared both before and after UV exposure. The results are summarized in Table 5.1.

Sample composition			Calorimetric data	
F127 (wt%)	Laponite (wt%)	PAG (mM)	T _{OM} (°C)	ΔH (J/g)
1.8	0	0	24.8 ± 2.00	0.54 ± 0.19
3.6			23.0 ± 1.80	1.09 ± 0.29
5.4			21.3 ± 0.15	1.59 ± 0.40
7.2			19.9 ± 0.12	2.62 ± 0.24
10			18.4 ± 0.01	3.28 ± 0.00
3.6	0	13	22.0 ± 0.55	0.68 ± 0.30
	1		19.7 ± 0.47	0.65 ± 0.11
	2		23.1 ± 0.85	0.27 ± 0.14
	3		20.9 ± 0.45	0.37 ± 0.13
	4		<i>No discernible micelle peak</i>	
3.6	3	0	24.0 ± 0.78	0.973 ± 0.15
		5	25.5 ± 0.37	0.575 ± 0.17
		13	20.9 ± 0.45	0.373 ± 0.13
		20	<i>No discernible micelle peak</i>	
<i>After UV exposure for 10 min @ 150mW/cm²</i>				
3.6	3	13	24.3 ± 0.50	0.309 ± 0.05
3.6	3	0	24.2 ± 2.30	0.303 ± 0.03
3.6	0	13	23.0 ± 0.03	2.10 ± 0.09

Table 5.1 Summary of effect of additives on thermal behavior of the dispersions.

T_{OM} represents the temperature for the onset of micellization while ΔH is the micellization enthalpy.

The results summarized in Table 5.1 clearly show that addition of Laponite and/or PAG to a 3.6wt% F127 solution causes a significant drop in the enthalpy of micellization, ΔH, from ~1.09J/g for pure F127 to as little as 0.373J/g in the presence of 3wt% Laponite and 13mM PAG. As the concentration of Laponite and PAG was further increased to 4wt% and 20mM respectively, the micellization endotherm is completely suppressed. The distinct and measurable difference in the ΔH caused by the presence of these additives is

attributed to the subsequent lower concentration of F127 used in this work. The suppression of the micellization endotherm in Figure 5.2 and Table 5.1 is attributed to the interactions of the additives with the F127 molecules. Upon the addition of Laponite nanoparticles, the surfactant molecules in solution can adsorb onto the nanoparticle as well as interact with the PAG molecules to help stabilize the dispersions.

The adsorbed molecules are no longer free to interact with other solubilized F127 molecules in solutions and cannot contribute to the temperature-induced micellization of F127 monitored via DSC as described in Chapter 3. At the higher surfactant concentrations previously investigated by De Lisi *et al.*²⁷ (> 10wt% F127), this depleted fraction of F127 is negligible relative to the total number of molecules in solution and the micellization endotherm appears unaffected. Consequently, any change in the enthalpy of micelle formation was not detected. At 3.6wt% F127 investigated in the current study, F127 depletion via interactions with Laponite plays a much more important role and results in a significantly lower number of F127 molecules available for micelle formation which can explain the observed suppression of the micellization endotherm analogous to a lower micelle concentration.

Since gelation of the PR fluid formulation occurs after UV exposure, DSC was carried out on a series of samples after UV-induced gelation. For a given composition, UV exposure caused the onset of micellization to occur at slightly higher temperatures. A significant decrease in the enthalpy associated with micelle formation was observed for samples containing Laponite indicating a further suppression of micelle formation after UV exposure. In the absence of Laponite particles, surprisingly the enthalpy associated with micelle formation for a 3.6wt% F127 and 13mM PAG solution showed an increase from 0.681J/g prior to UV exposure to 2.10J/g after UV exposure. We attribute this behavior to the presence of relatively hydrophobic iodobenzene after UV photolysis of the PAG. The endotherm associated with micelle formation in Pluronic block copolymers has been attributed to the desolvation of the hydrophobic PPO blocks²⁹, the increase in enthalpy after UV photolysis of the PAG is likely due to the higher concentration of

hydrophobic components in the aqueous dispersion in the form of iodobenzene encapsulated within the PPO-rich micelle cores.

5.4.2 Effect of solution formulation and UV intensity on gelation kinetics

Photogelation of the F127, Laponite and PAG containing dispersion formulation is a multi-step process involving (a) photolysis of the PAG, (b) desorption of the Pluronic F127 from the surface of the Laponite nanoparticles, and (c) reorganization of the dispersed Laponite nanoparticles into a *house of cards* network to form the gel state. Each of these steps is time-dependent and can have a significant effect on the gelation kinetics. A series of experiments were conducted surrounding a dispersion formulation of 3.6wt% F127, 3wt% Laponite and 13mM PAG to investigate the effect of solution composition on the gelation behavior. Since the PAG is the primary UV active component of the system, *in situ* photorheology at a fixed sample composition but different UV intensity (100-150mW/cm²) was also performed to probe the effect of PAG photolysis.

Figure 5.3 below shows a summary of the results obtained when each component within the formulation is varied independently ((a)-(c)) as well as when the UV intensity is varied at constant formulation composition (Figure 5.3 (d)). Figure 5.3 tracks the evolution of the complex viscosity as a function of time while Figure 5.4 shows the behavior for the storage and loss moduli (G' and G'' respectively) during the gelation process.

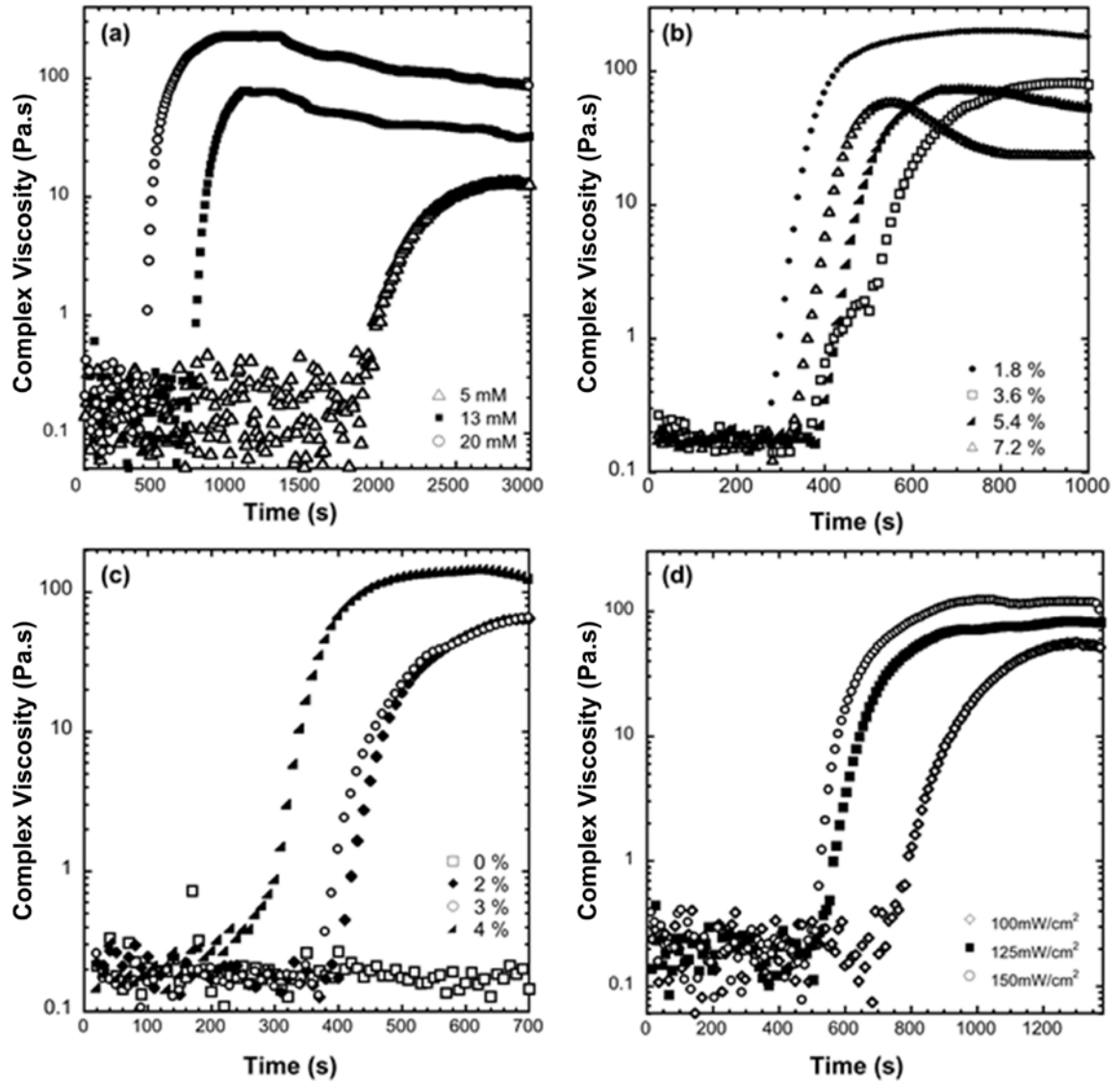


Figure 5.3 Summary of *in-situ* photogelation kinetics showing changes in complex viscosity.

Results are shown as a function of dispersion formulation. Effect of (a) PAG concentration (5-20mM) with 3.6wt% F127 + 3wt% Laponite (b) F127 concentration (1.8-7.2wt%) with 3wt% Laponite + 13mM PAG and (c) Laponite concentration (0-4wt%) with 3.6wt% F127 + 13mM PAG. (UV intensity = 150 mW/cm²) (d) Effect of UV intensity on photogelation kinetics for a dispersion containing 3.6wt% F127, 3wt% Laponite and 13mM PAG. The graphs illustrate the change in the complex viscosity of the system as a function of time while under UV illumination.

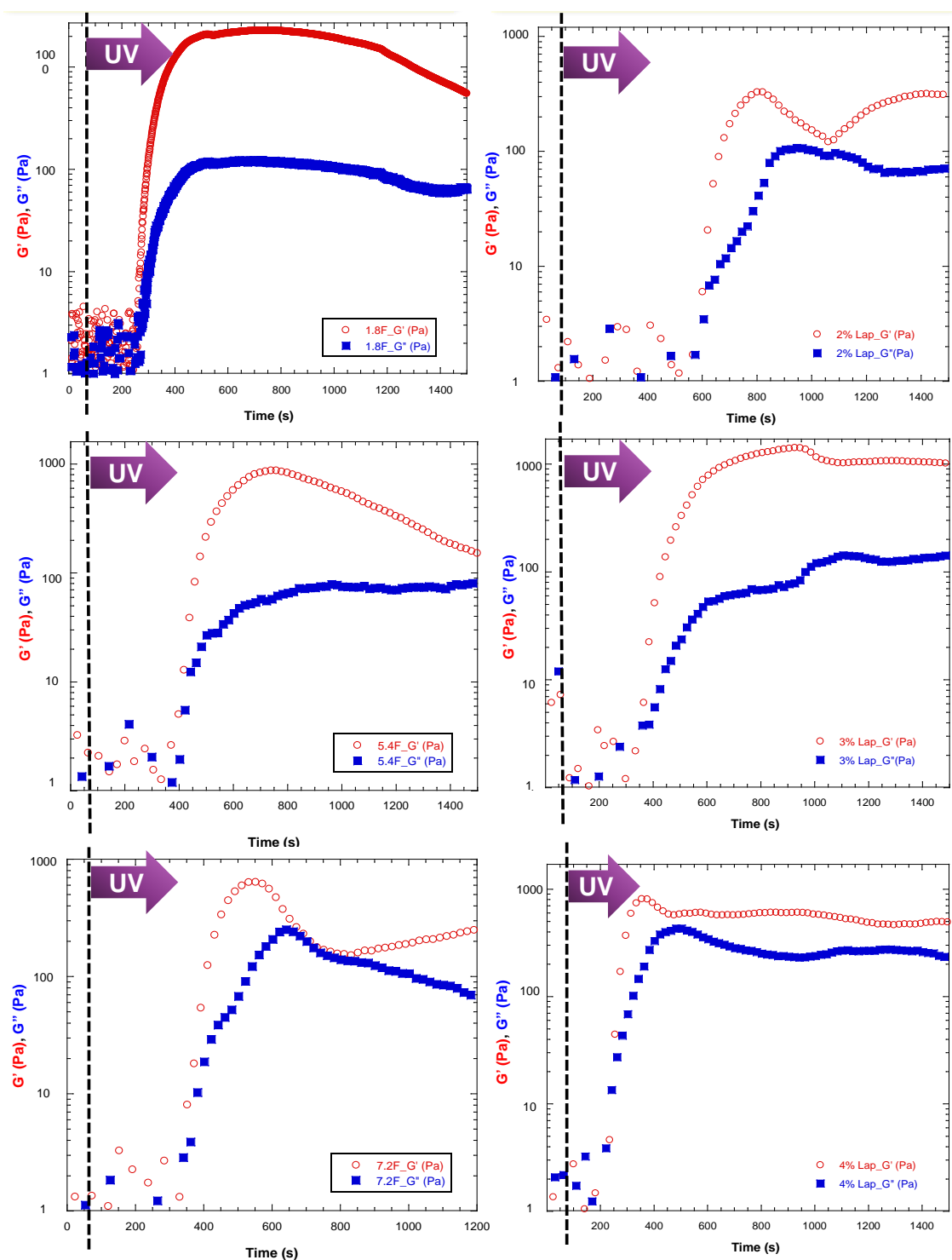


Figure 5.4 G' (open) and G'' (filled) profiles as a function of UV exposure time.

Left: Effect of changing F127 concentration (top: 1.8wt%, middle: 5.4wt% and lower: 7.2wt%) with 3wt% Laponite and 13mM PAG; Right: Effect of changing Laponite concentration with 3.6wt% F127 and 13mM PAG (top: 2wt%, middle: 3wt% and lower: 4wt%).

5.4.3 Quantifying kinetics of gelation via photorheological studies

While the complex viscosity evolution with time shows the effect of UV on the gelation, further quantification of the reaction kinetics was achieved by applying a log-Boltzmann sigmoidal fit, described by Equation 5.1, to the data.

$$\log \eta^*(t) = \log(\eta_f^*) + \frac{\log(\eta_0^*) - \log(\eta_f^*)}{\left(1 - e^{-\frac{4(t-t_0)}{\Delta t}}\right)} \quad (5.1)$$

where η_0^* and η_f^* are the measured viscosities before illumination (initial viscosity) and after network formation at long times of illumination (final viscosity) respectively. t_0 corresponds to the time necessary for $\log \eta^*(t)$ to reach a value midway between $\log(\eta_0^*)$ and $\log(\eta_f^*)$ while Δt describes the period associated with the sigmoidal transition region as complex viscosity toggles from η_0^* to η_f^* ³⁰⁻³³.

As Δt gets smaller, the time to achieve final viscosity also decreases; Δt can therefore be used as the characteristic gelation time within the log-Boltzmann sigmoid model. The results obtained from the fits for each data set is summarized in Table 5.2 and Table 5.3 respectively.

<i>Solution Composition</i>			<i>Log-Boltzmann Sigmoidal Fit Parameters</i>			
F127 (wt%)	Laponite (wt%)	PAG (mM)	η_0^* (Pa-s)	η_f^* (Pa-s)	t_0 (s)	$\Delta t/4$ (s)
1.8	3	13	3.39×10^{-3}	178.0 ± 1.3	295 ± 24	41.9 ± 3.7
3.6			8.32×10^{-3}	79.4 ± 1.5	438 ± 93	58.7 ± 9.6
5.4			4.68×10^{-3}	70.8 ± 1.6	417 ± 51	55.4 ± 10.2
7.2			7.41×10^{-3}	67.6 ± 1.1	350 ± 8	47.4 ± 2.3
3.6	2	13	2.09×10^{-3}	66.1 ± 1.0	386 ± 25	51.1 ± 1.9
	3		8.32×10^{-3}	79.4 ± 1.5	438 ± 93	58.7 ± 9.6
	4		2.40×10^{-1}	83.2 ± 1.6	355 ± 109	23.1 ± 6.7
3.6	3	5	5.62×10^{-3}	17.4 ± 1.4	1960 ± 150	167.0 ± 24.0
		13	8.32×10^{-3}	79.4 ± 1.5	438 ± 93	58.7 ± 9.6
		20	1.17×10^{-2}	89.5 ± 1.2	463 ± 54	30.0 ± 0.0

Table 5.2 Summary of sigmoidal fit results for gelation kinetics as a function of sample composition.

UV intensity (mW/cm²)	PAG (mM)	η_0^* (Pa-s)	η_f^* (Pa-s)	t_0 (s)	$\Delta t/4$ (s)
100	5	5.62×10^{-3}	<i>No gelation after 3600 s of UV exposure</i>		
	13	8.32×10^{-3}	61.7 ± 1.0	832 ± 82	80.0 ± 14.0
	20	1.17×10^{-2}	224.0 ± 1.1	538 ± 164	40.0 ± 13.0
120	13	8.32×10^{-3}	80.7 ± 1.2	630 ± 93	53.0 ± 8.0
150	5	5.62×10^{-3}	17.4 ± 1.4	1960 ± 150	167.0 ± 24.0
	13	8.32×10^{-3}	79.4 ± 1.5	438 ± 93	58.7 ± 9.6
	20	1.17×10^{-2}	89.5 ± 1.2	463 ± 54	30.0 ± 0.0

Table 5.3 Summary of sigmoidal fit for different UV exposure intensity and PAG concentrations.

Dispersions contain fixed concentrations of Laponite (3wt%) and F127 (3.6wt%)

From these parameters, a gelation rate defined mathematically as the time taken for the complex viscosity to increase from initial (η_0^*) to final (η_f^*) values was calculated for each case using equation 5.2.

$$Rate \propto \frac{\eta_f^* - \eta_0^*}{\Delta t} \quad (5.2)$$

Figure 5.5 illustrates how the gelation rate was affected by composition as well as UV intensity. The concentration of F127 was found to have a negligible effect on the photogelation kinetics for dispersions containing more than 3.6wt% F127 as shown in Figure 5.5(a). However, at a lower concentration of 1.8wt% F127, the gelation rate is much higher. This behavior is attributed to the higher ratio of Laponite to F127 and faster rearrangement of the nanoparticles as a result of fewer F127 molecules available and able to adsorb onto the particle surface.

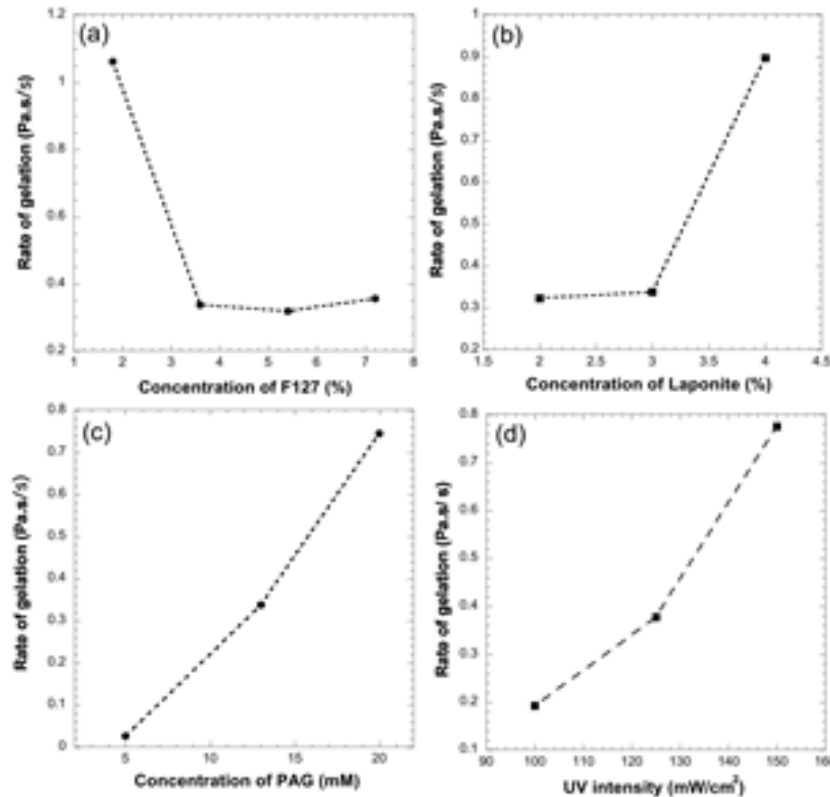


Figure 5.5 Gelation rate variations as a function of composition.

Dispersions formulations varied surrounding 3.6wt% F127, 3wt% Laponite and 13mM PAG exposed to 150 mW/cm² UV intensity and the effect of (a) F127 concentration, (b) Laponite concentration, (c) PAG concentration and (d) UV intensity. The gelation rate is defined as the rate of increase of the complex viscosity of the sample and is given in (Pa-s)/s.

Figure 5.5(b) shows that increasing the Laponite particle concentration results in a higher gelation rate. Figure 5.3(c) shows that the presence of Laponite nanoparticles is essential for photogelation as the sample viscosity remains constant in the absence of nanoparticles. As Laponite concentration, hence number of Laponite particles, within a fixed volume increase, the corresponding probability of interactions between individual particles leading to cluster formation and creating stiff regions that contribute to the viscosity rise. This interaction probability scales with the Laponite concentration since the inter-particle distance decreases as concentration increases. At high Laponite concentration, the attractive electrostatic interactions producing the nanoparticle network can therefore occur much more readily once depletion of free F127 has taken place and surface charges have been generated resulting in a higher gelation rate.

Since the PAG is the photoactive component, it is expected to have a large influence on the gelation kinetics as shown by the large, almost linear, increase in gelation rate with PAG concentration shown in Figure 5.5(c). Increasing the UV intensity causes the gelation rate to increase as shown in Figure 5.5(d) since the photon flux contributing to photolysis also increases. The PAG can therefore undergo photolysis at a faster rate leading to faster F127 desorption from Laponite nanoparticles and subsequent rearrangement into a *house of cards* network. The dependence of the gelation rate on both the PAG concentration and UV intensity provide further evidence of the importance of the PAG photolysis in the photogelation process.

5.4.4 Photogelation mechanism, kinetics and structure

The final gel viscosity of the system can be related to the overall structure and arrangement within the gel system. Changes in the gel viscosity measured as a function of sample composition thus provide insight into the possible network structure. Figure 5.6 shows the variation in the final gel viscosity when each component of the sample is varied.

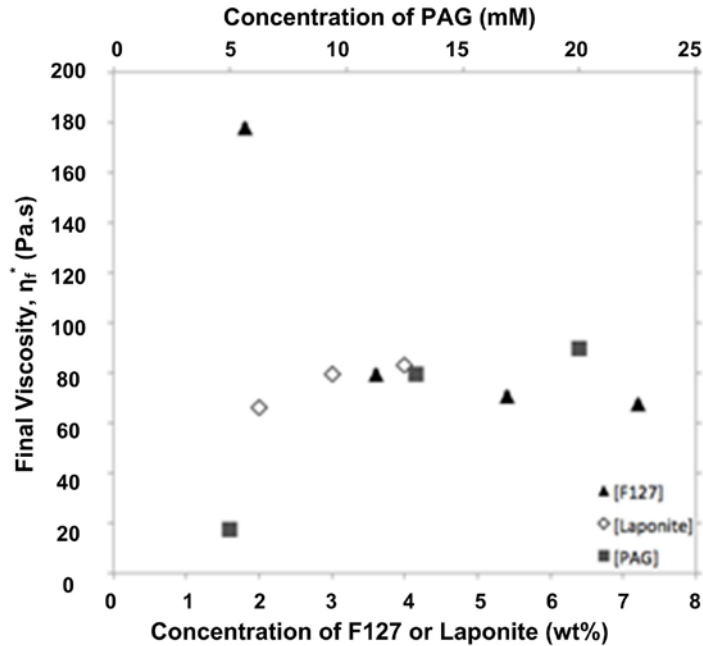


Figure 5.6 Final viscosity of the gels with different dispersions.

Results obtained from starting formulation composition 3.6wt% F127, 3wt% Laponite and 13mM PAG and varying components one at a time in the range of F127 (1.8-7.2wt%), Laponite (2-4wt%) and PAG (5-13mM).

Increasing the F127 concentration causes a significant drop in the final gel viscosity indicating a weaker gel. We attribute this to two possible effects. First, as indicated by the DSC results discussed earlier, increasing the F127 concentration results in a larger number of "free" molecules available to encapsulate the generated iodobenzene. Consequently, de-shielding of Laponite nanoparticles is delayed, thus preventing network formation and subsequent gelation. Secondly, at high enough PAG concentrations resulting in de-shielding and particle network formation, the increased F127 concentration may result in formation of a larger number of micelles, which can subsequently act as defects within the gel, causing it to be weaker. Figure 5.7 illustrates the proposed gel structure resulting from each of these cases.

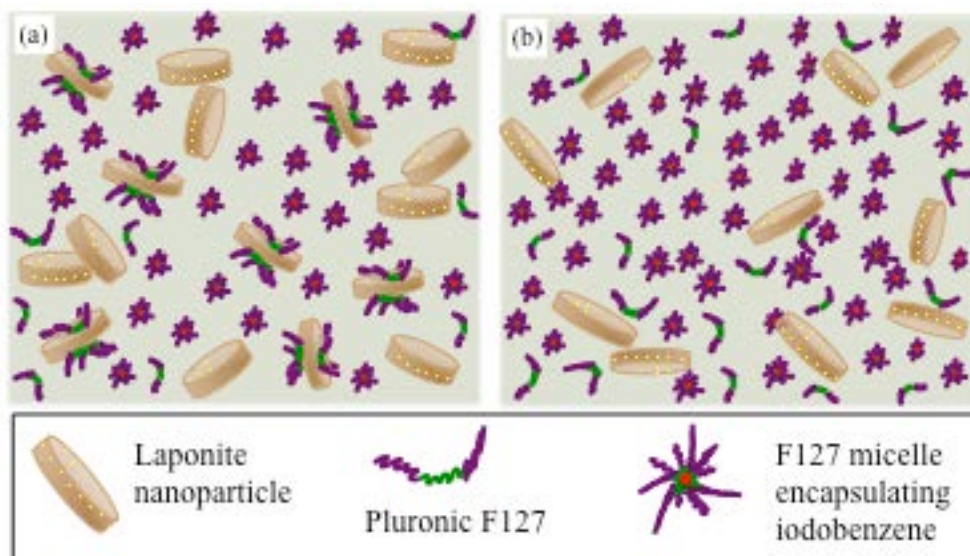


Figure 5.7 Schematic of proposed final gel structure at high F127 concentration.

The presence of excess polymer accounts for lower final viscosity. (a) Insufficient de-shielding of Laponite nanoparticles for network formation and (b) Large areas of micelles grouped together preventing continuous network of nanoparticles

On the other hand, increasing both Laponite and PAG concentration results in an increase in final viscosity of the gel. The gel viscosity is then correlated to the macromolecular gel structure. The Laponite particles are essential in creating a nanoparticle network as indicated by the constant viscosity and maintained fluid state of dispersions with no Laponite in Figure 5.3(c). As the nanoparticle concentration increases, the final gel structure can change from having a few pockets of interacting particles to a percolating network, which provides added rigidity to the material and produces a higher final viscosity. This proposed variation is illustrated in Figure 5.8.

Finally, increasing the PAG concentration also causes an increase in final viscosity. This is attributed to the strength of the network formed after UV-induced photolysis. As PAG concentration increases, the concentration of both iodobenzene and benzoic acid after photolysis also increases. More efficient de-shielding of the Laponite nanoparticles occurs and the charged Laponite particles may experience stronger electrostatic forces. A stronger network is produced from the charged particles being held together more strongly producing a higher final viscosity.

Using the current work, we have identified a framework for intelligent design and formulation of photoactive systems. For example, to maximize the gel strength as measured by the final viscosity, the concentration of Laponite particles needs to increase while that of F127 needs to be minimized. At the same time, since rate of gelation of the system plays a significant role in possible applications of such systems, the gelation rate can now be tuned by simply changing the concentration of the PAG in the dispersion. A high PAG concentration will lead to a fast gelling system even at low UV intensity while the reverse is also true. The photogelation rates can also be tuned by using different PAGs with more efficient UV absorption and subsequent photolysis leading to a quicker lowering in the pH of the system. Figure 5.9 below provides a simplified view of this complex three-phase dispersion and summarizes the effect of sample composition on the gelation rate and final viscosity of the gel formed identified through the current work

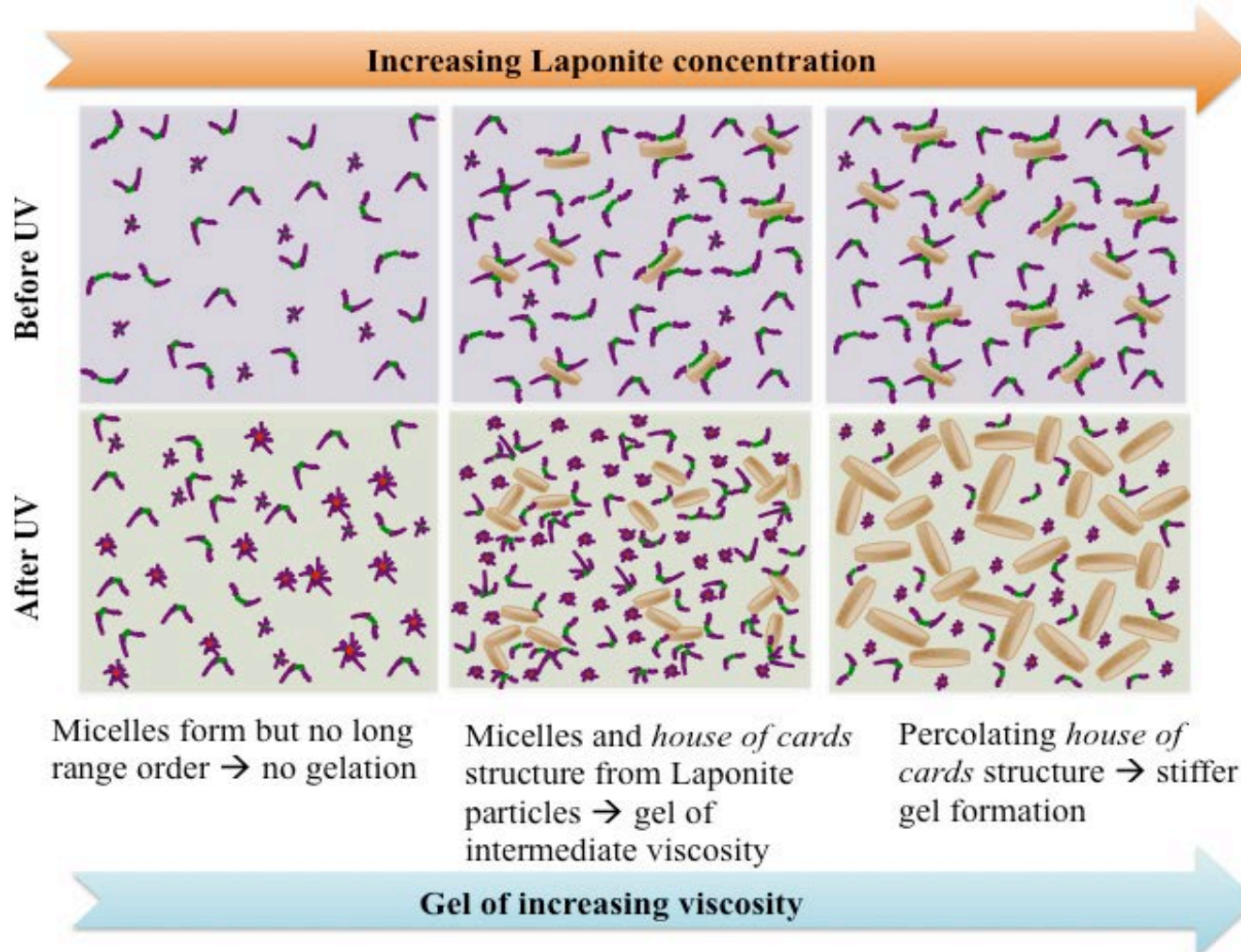


Figure 5.8 Schematic of resulting gel as a function of Laponite particle concentration

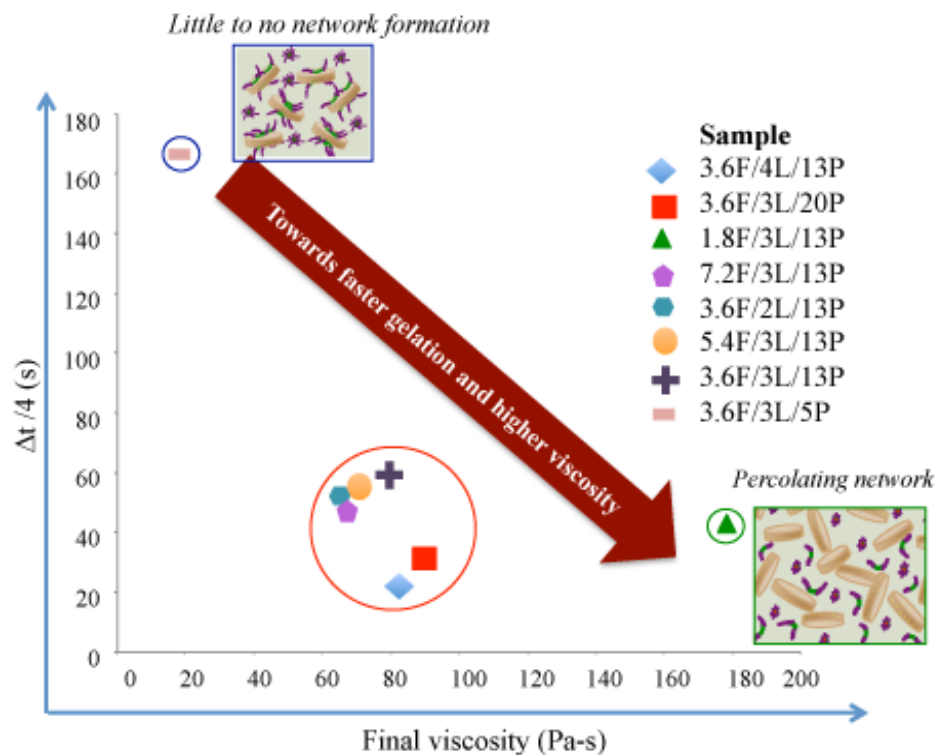


Figure 5.9 Parameter space mapping for Laponite dispersion photogelation kinetics and final viscosity (UV intensity=150 mW/cm²).

5.4.5 Microstructure and SAXS

SEM of the bulk microstructure after lyophilization was done to determine changes due to the addition of the PAG and subsequent effect of UV irradiation. Representative images are shown in Figure 5.10 illustrating the changes in the microstructure upon adding the PAG molecules and the effect of UV irradiation.

As shown in Figure 5.10 B1-B3, addition of the PAG changes the microstructure and results in a relatively uniform microstructure with globular features. The presence of the Laponite particle network described in Chapter 4 and shown here in Figure 5.10 A3 is no longer evident indicating improved dispersion with the added PAG, although the roughness becomes obvious at higher magnification (Figure 5.10 B3).

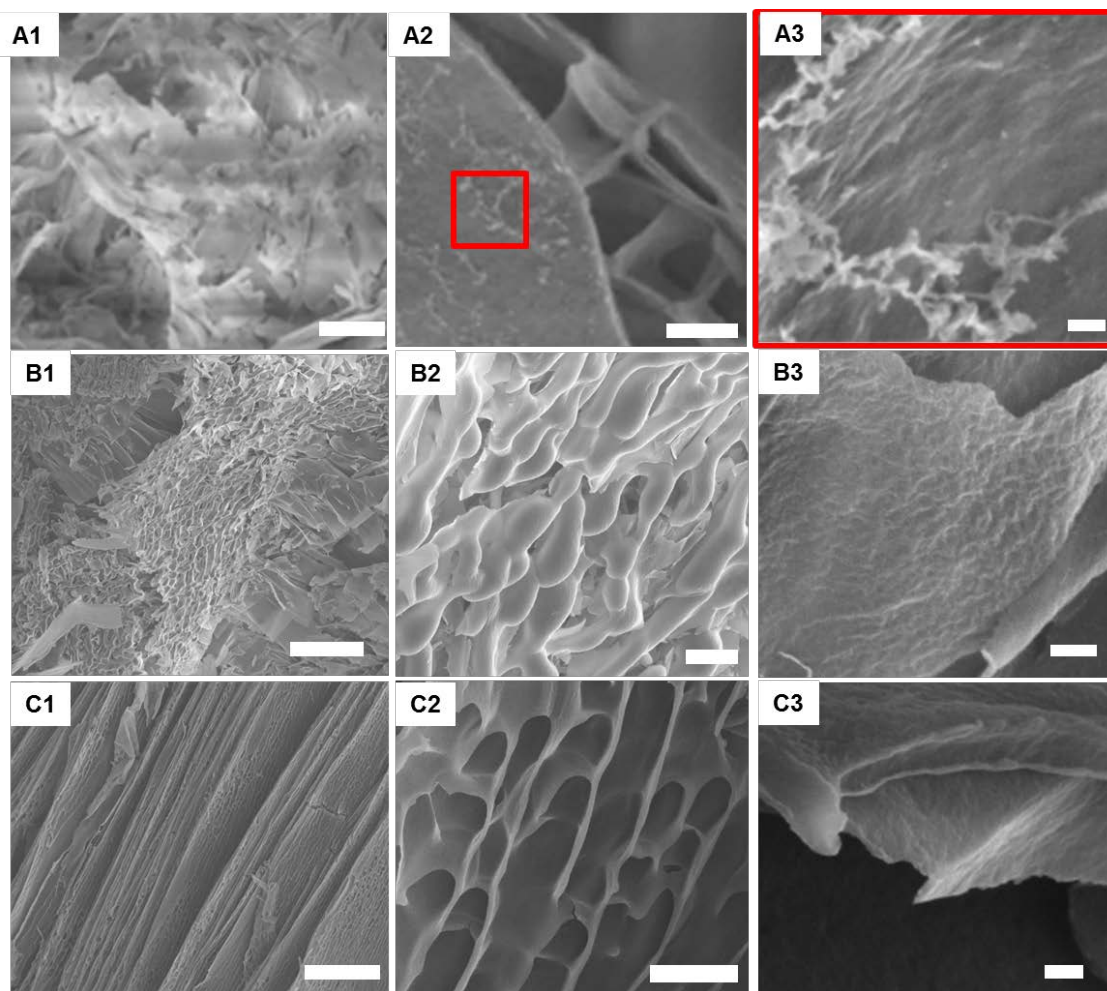


Figure 5.10 Representative SEM images of lyophilized samples.

A1-A3 = 3wt% F127 with 3wt% Laponite; B1-B3: Same as A1-A3 with 5mM PAG and before UV irradiation; C1-C3: same as B1-B3 but after UV irradiation. Scale bars in left column = 50µm, middle column = 5µm and right = 400nm

UV exposure has a significant effect and increases the order and arrangement within the samples. Figure 5.10 C1 shows well aligned layers at low magnification exhibiting an interconnected network of large pores as shown in C2. C3 shows a high magnification image of the individual layers after UV irradiation showing relatively uniform thickness on the order of 300nm. However, the resolution of the SEM images as well as the need to extract water prior to imaging does not provide detailed (or accurate) information about the particle arrangement and spacing. Instead, variable temperature SAXS of the

dispersions before and after gelation was used to probe the structure and determine the characteristic spacing in the dispersion.

The SAXS results summarized in Figure 5.11 indicate that, before UV irradiation, the dispersion exhibits a similar ordering in the presence of the PAG as reported in Chapter 4 for dispersions with no PAG. However, after gel formation by UV exposure, the characteristic spacing is no longer temperature dependent; instead, a spacing on the order of 22nm was extracted for all temperatures. Again, the large error bar for the photogel samples shown here were due to the broad peak in the structure factor curves obtained indicating polydispersity in the spacing and arrangement.

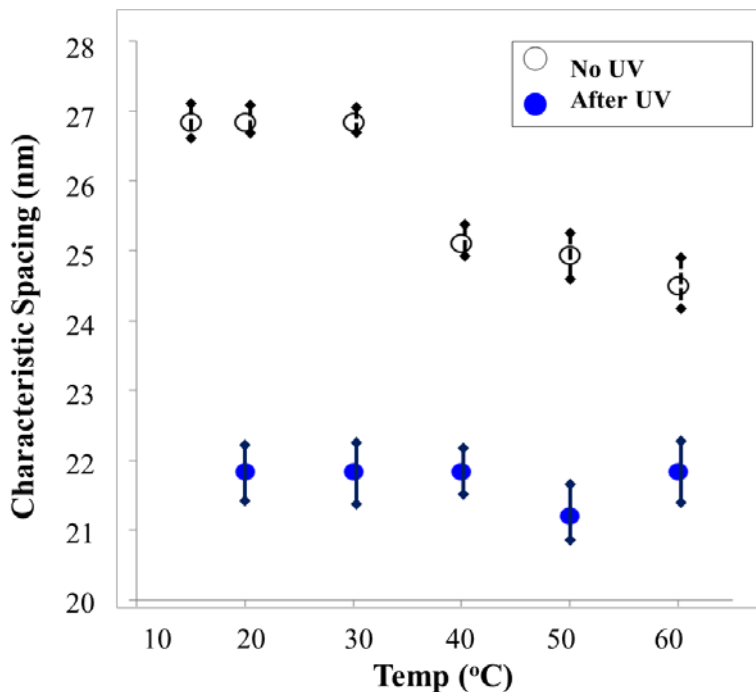


Figure 5.11 Summary of temperature dependent SAXS results before and after UV exposure

The data indicates that UV induced gel formation results in a “frozen” structure with fixed arrangement throughout the temperature range probed (solid markers). The dispersion composition used here contained 3.6wt% F127, 3wt% Laponite and 5mM PAG.

Since UV induced gelation occurs via a chemical reaction, the gel formed is expected to be permanent and independent of thermal changes when sealed. The fixed spacing after

UV exposure also provides further evidence of the gelation mechanism described throughout this chapter. The fixed spacing provided evidence that the gel produced contains particles or clusters that are not affected by changes in the F127 molecules; instead changes in the polymer likely to occur at different temperatures has no effect on the arrangement of Laponite particles within the gel. TEM images (Figure 5.12) of lyophilized samples after UV exposure indicated that the particles are relatively well dispersed throughout the layers shown Figure 5.10 C3. The particles are again arranged in both face to edge and edge to edge configurations.

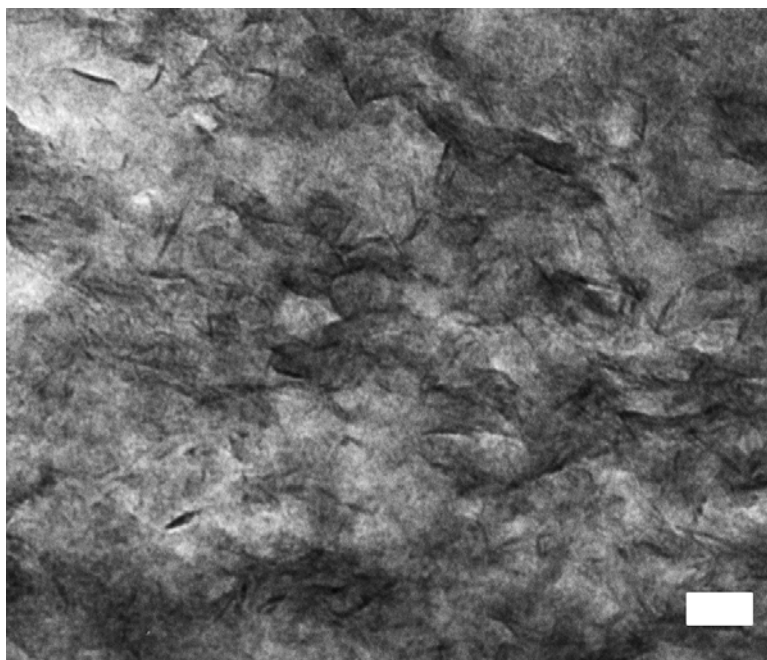


Figure 5.12 Representative TEM of lyophilized gel after UV exposure.

Dispersion composition of 3.6wt% F127, 3wt% Laponite and 5mM PAG (scale bar = 100nm).

5.5 Conclusion

A detailed study into the kinetics of photogelation of PR fluid dispersions was conducted in the low concentration regime of Pluronic F127, Laponite nanoparticles and a photoacid generator (PAG) using *in situ* photorheology as the primary tool to characterize bulk gelation. The results show the effect of dispersion formulation on the gelation kinetics. Increasing F127 concentration delays the time required for onset of gelation and lowers

the final viscosity while the presence of Laponite nanoparticles in the system was found to be essential for photogelation to occur. PAG concentration and PAG photolysis were both significant factors affecting the gelation kinetics of the dispersion.

Using DSC, we demonstrate that for F127 concentrations below 10wt%, the interaction between F127 and Laponite has a significant effect on the ability of F127 to form micelles in solution. Temperature dependent SAXS data further supports the formation of a permanent gel with fixed arrangement and supports the gel formation mechanism described.

We further build on the gelation mechanism and propose a scheme describing the influence of the starting composition on the resulting gel structure and correlate this with the measured final viscosity. While this scheme provides a simplified view of a complicated system, additional work remains necessary to fully understand the gelation kinetics and complex interactions in these nanoparticle-based photoactive systems. Identification of the rate limiting steps in photogelation of these systems remains a key requirement for full optimization and design of PR fluid formulations to be used in applications where control of time-dependent response is essential.

5.6 References

- (1) I. Porcar, P. Perrin, C. Tribet, *Langmuir* **2001**, 17, 6905.
- (2) H. Sakai, Y. Orihara, H. Kodashima, A. Matsumura, T. Ohkubo, K. Tsuchiya, M. Abe, *J. Am. Chem. Soc.* **2005**, 127, 13454.
- (3) J. Eastoe, A. Vesperinas, *Soft Matter* **2005**, 1, 338.
- (4) M. Gianneli, R. F. Roskamp, U. Jonas, B. Loppinet, G. Fytas, W. Knoll, *Soft Matter* **2008**, 4, 1443.
- (5) S. Reinicke, S. Döhler, S. Tea, M. Krekhova, R. Messing, A. M. Schmidt, H. Schmalz, *Soft Matter* **2010**, 6, 2760.
- (6) I. Willerich, F. Groehn, *Chem. Eur. J.* **2008**, 14, 9112.
- (7) I. Willerich, F. Groehn, *Angew. Chem. Int. Ed.* **2010**, 49, 8104.
- (8) T. Wolff, C. S. Emming, T. A. Suck, G. Vonbunau, *J. Phys. Chem.* **1989**, 93, 4894.
- (9) A. M. Ketner, R. Kumar, T. S. Davies, P. W. Elder, S. R. Raghavan, *J. Am. Chem. Soc.* **2007**, 129, 1553.
- (10) T. G. Shang, K. A. Smith, T. A. Hatton, *Langmuir* **2006**, 22, 1436.
- (11) G. Pouliquen, C. Tribet, *Macromolecules* **2006**, 39, 737.
- (12) G. O. Lloyd, J. W. Steed, *Soft Matter* **2010**, 7, 75.
- (13) R. Kumar, S. R. Raghavan, *Soft Matter* **2009**, 5, 797.
- (14) K. Sun, R. Kumar, D. E. Falvey, S. R. Raghavan, *J. Am. Chem. Soc.* **2009**, 131, 7135.
- (15) A. Nelson, T. Cosgrove, *Langmuir* **2004**, 20, 10382.
- (16) P. Mongondry, T. Nicolai, J. F. Tassin, *J. Colloid Interface Sci.* **2004**, 275, 191.
- (17) A. Loiseau, J. F. Tassin, *Macromolecules* **2006**, 39, 9185.
- (18) S. L. Tawari, D. L. Koch, C. Cohen, *J. Colloid Interface Sci.* **2001**, 240, 54.
- (19) B. Jönsson, C. Labbez, B. Cabane, *Langmuir* **2008**, 24, 11406.
- (20) T. Nicolai, S. Cocard, *Langmuir* **2000**, 16, 8189.
- (21) P. Alexandridis, J. F. Holzwarth, T. A. Hatton, *Macromolecules* **1994**, 27, 2414.
- (22) G. Wanka, H. Hoffmann, W. Ulbricht, *Macromolecules* **1994**, 27, 4145.
- (23) A. Cabana, A. Aït-Kadi, J. Juhász, *J. Colloid Interface Sci.* **1997**, 190, 307.
- (24) B. K. Lau, Q. Wang, W. Sun, L. Li, *J. Polym. Sci., Part B: Polym. Phys.* **2004**, 42, 2014.
- (25) A. A. Barba, M. D'amore, M. Grassi, S. Chirico, G. Lamberti, G. Titomanlio, *J. Appl. Polym. Sci.* **2009**, 114, 688.
- (26) Y. Lin, P. Alexandridis, *J. Phys. Chem. B* **2002**, 106, 10834.
- (27) R. De Lisi, G. Lazzara, S. Milioto, N. Muratore, *J. Therm. Anal. Calorim.* **2007**, 87, 61
- (28) I. Boucenna, L. Royon, P. Colinart, *J. Therm. Anal. Calorim.* **2009**, 98, 119.
- (29) G. Wanka, H. Hoffmann, W. Ulbricht, *Colloid Polym. Sci.* **1990**, 268, 101.
- (30) B. J. Love, F. Teyssandier, Y. Y. Sun, C. P. Wong, *Macromol. Mater. Eng.* **2008**, 293, 832.
- (31) B. J. Love, F. P. Ruinet, F. Teyssandier, *J. Polym. Sci., Part B: Polym. Phys.* **2008**, 46, 2319.
- (32) T. Savart, C. Dove, B. J. Love, *Macromol. Mater. Eng.* **2010**, 295, 146.

(33) F. Teyssandier, B. J. Love, *J. Appl. Polym. Sci.* **2011**, 120, 1367

APPENDIX 5-A: UV intensity calibration at sample surface

Prior to running the photorheology experiments, the UV shield and light pipe are attached to the rheometer surrounding the parallel plates. The UV lamp was turned on at least 30 minutes prior to running the experiments to allow the lamp to warm up and stabilize. To ensure uniform UV intensity on the sample surface, a UV radiometer was placed between the parallel plates at 5 different positions shown below in Figure 5-A and the intensity measured in each case. The position of the light guide and lens housing was adjusted by turning the screws connecting the UV light pipe and lens to adjust the alignment until the measured intensity variation at the 5 positions (a)-(e) was less than 10%.

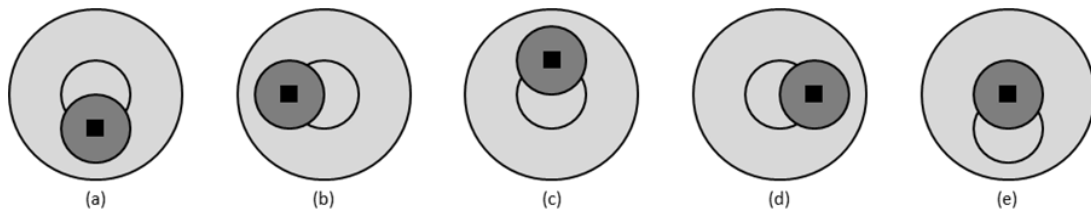


Figure 5- A Schematic of positions used to calibrate UV intensity to ensure uniform UV exposure on sample.

APPENDIX 5-B: Illustration of Lorentz-corrected plots to determine structure

Figure 4-B shows the scattering profile from of the 3% Laponite/ 3.6% F127 dispersions as a function of temperature. As shown here, little to no changes are immediately apparent.

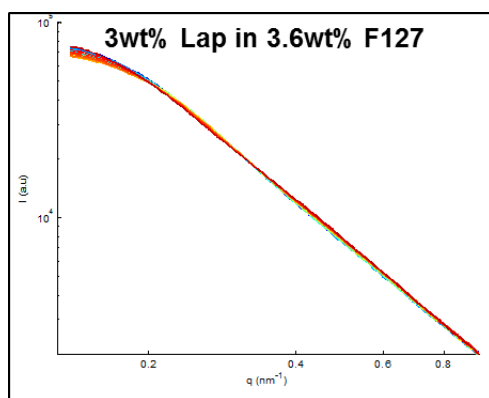


Figure 5- B Scattering data from 3wt% Laponite with 3.6wt% F127 as a function of temperature.

Figure 4-C shows the Lorentz-corrected plot following the method by Paineau *et al.* The peak position shifts to the right and becomes broader as temperature increases (blue to red lines).

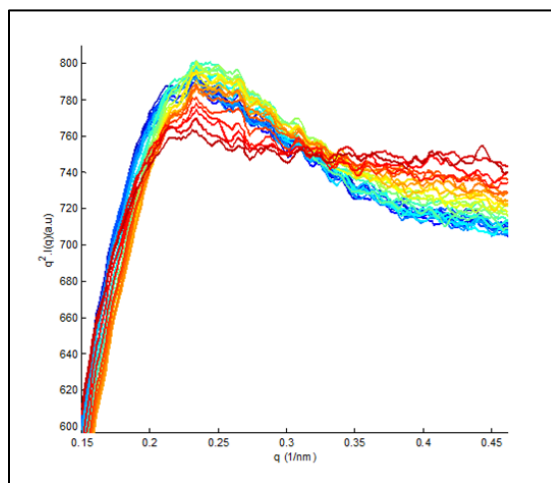


Figure 5- C Lorentz corrected from scattering data before UV exposure showing change in peak.

The graph shows the characteristic peak position in 3wt% Laponite and 3.6wt% F127 which shifts from low to high q as temperature increases.

CHAPTER 6

6. *In situ* time resolved UV-SAXS: Correlating bulk and nanoscale changes during photogelation

6.1 Chapter Summary

Chapter 6 focuses on determining structural changes during the photo induced gel formation process described in Chapter 5 where, by simply changing the formulation composition and adding a photoacid generator, the liquid to gel transition occurs upon UV irradiation. SAXS results show that such a gel has a stable structure with variable temperature. The current chapter focuses on the structural changes that occur during the UV irradiation process to produce the gel. In particular, the goal here is to compare the dynamics of the structural changes to the bulk gelation and assess the role of different chemistry by changing the photoacid generator used.

6.2 Introduction

The ability to create 3D structures of nanoparticles by using either a template or by applying an external stimulus has been widely studied¹⁻⁵. These structures are governed in general by a balance of attractive and repulsive forces in the system^{3, 6-9}. Among the most studied materials are colloidal nanoparticles, particularly spherical particles. The study of non-spherical particles such as disks and rods remains a challenge due to the asymmetrical shape and complex interactions⁴. Disk shaped clay particles such as natural clays as well as synthetic Laponite clays have been widely studied in the last decade both as a model colloidal system and a nano-filler for various composite materials¹⁰⁻¹⁷. These particles are known to self-assemble into a network in solution^{11, 18-21}. Clay dispersions have been widely probed with various techniques such as rheology²²⁻²⁴, scattering methods²⁵⁻³⁰ and TEM^{31, 32}.

Prior work using both contrast matched small angle neutron scattering (SANS)^{16, 25-27, 29, 33} and ultra-small angle neutron scattering (USANS)²⁵ has demonstrated that Laponite nanoparticles can form large scale aggregates in a dispersion while the addition of a polymer results in a core-shell structure. SANS data taken at different temperatures has provided evidence of aggregation in thermally gelling Laponite/polymer systems¹⁶. However, one limitation of SANS experiments is the long data collection time required to increase the signal to noise ratio. More recently, Ruzicka *et al.* showed that the structure of Laponite dispersions can change significantly with time using synchrotron SAXS experiments conducted over extended time periods of up to 30,000hrs³⁴. However, to date, little to no work exists on the dynamic structural evolution occurring in a Laponite containing responsive system.

The work presented so far has demonstrated that the presence of different components in aqueous Laponite dispersions has a significant effect on both the structural organization and the properties of these dispersions. Chapter 5 showed the ability to achieve on demand liquid to gel transition by simply adding a commercially available photoacid generator to the dispersions and probed the kinetics of such a transition. However, the particle rearrangement taking place during the gel formation and the relationship between the time relating the bulk and nanoscale changes has not been studied. The evidence presented in Chapter 5 suggests that gelation occurs via assembly of the Laponite nanoparticles into a fixed 3D structure upon UV irradiation. The following chapter shows that the particle rearrangement can be directly probed using simultaneous time resolved UV-SAXS measurements. Finally, the time scale at which structure evolution occurs is compared and correlated to the bulk gelation kinetics.

6.3 Experimental Methods

Formulation: Dispersions of Laponite and F127 were prepared in d-H₂O as described in Chapter 3. The dispersions discussed here contain 3wt% and 3.6wt% F127. Photogelling dispersions were prepared as described in Chapter 5. Three different commercially available PAGs shown in Table 6.1 were used to in the concentration range of 5mM-20mM.

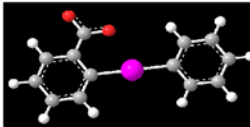
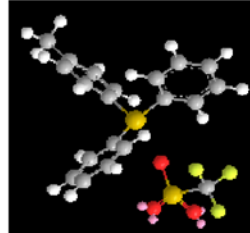
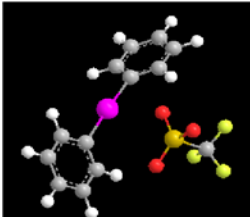
Code	Chemical name	Formula	Structure
PAG 1	Diphenyl iodonium-2-carboxylate monohydrate	$C_{13}H_9I^+O_2^- \cdot H_2O$	
PAG 2	(4-Methylphenyl) diphenylsulfonium triflate	$C_{20}H_{17}S^+ \cdot (CF_3SO_3)^-$	
PAG 3	Diphenyl-iodonium triflate	$(C_6H_5)_2I^+ \cdot (CF_3SO_3)^-$	

Table 6.1 Summary of photoacid generator (PAG) compounds used in this study

Photorheology: Rheometry and photorheometry experiments were conducted as previously described in Chapter 5. All experiments were conducted with a gap size of < 1.0mM to ensure uniform UV exposure throughout the sample and minimize the effect of thickness variations on the absorption of UV light. In all cases, UV exposure was started 60 seconds after the onset of data collection.

NMR: Nuclear Magnetic Resonance (NMR) experiments were conducted as a function of UV exposure time on PAG samples dissolved in D_2O to determine the irradiation induced chemical changes and the time taken for these to occur. To ensure that samples were not accidentally exposed to ambient light, the solutions for the initial chemical structure were loaded in amber tinted tubes impervious to UV. Samples undergoing UV irradiation were loaded in quartz tubes, sealed and exposed to broadband UV ($\lambda = 320-500nm$) for different time periods and spectra were collected using a Varian 400 NMR spectrometer.

Time resolved UV-SAXS: Time resolved simultaneous UV-SAXS experiments were conducted at Beamline 12-ID (B,C and D) at the Advanced Photon Source (APS) at Argonne National Labs (Lemont, IL). Due to the long sample to detector distance, a larger q -range ($0.08\text{-}4.5\text{nm}^{-1}$) relative to the results from experiments described in Chapter 5 was accessible. All samples were loaded in a quartz capillary placed inside a Peltier controller before being placed in the Beamline and data was collected using a 2D MarCCD detector. An optical cable was mounted perpendicular to x-ray beam in order to conduct simultaneous UV-SAXS measurements. The UV intensity was calibrated using a radiometer mounted behind the sample and UV onset was controlled remotely. Figure 6.1 shows the UV-SAXS setup used for the combined UV-SAXS experiments.

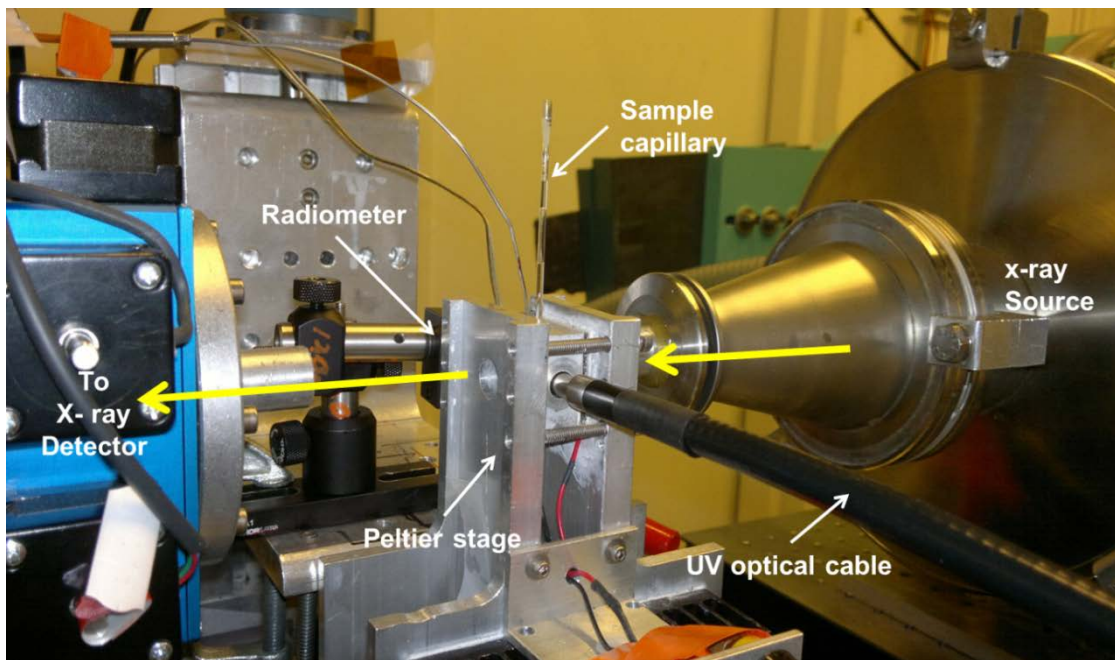


Figure 6.1 Picture of setup used for simultaneous UV-SAXS at 12-ID at the Advanced Photon Source.

To ensure that beam damage did not occur, time resolved SAXS spectra were initially collected without UV; the intensity and data acquisition parameters were adjusted until no change in the scattering occurred over a 60 min collection period ensuring the integrity of the sample in the absence of UV irradiation. Time resolved measurements were collected at 1s/frame. An average of 10 frames per spectrum was collected and spectra were collected at a rate of 6 per minute.

6.4 Results

6.4.1 Photogelation

The type of PAG used was found to have a significant effect on the photogelation kinetics. Figure 6.2 shows the complex viscosity advancement of samples containing 5mM PAG with 3wt% Laponite and 3.6wt% F127 as a function of UV exposure times. In each case, UV onset in each case occurred at 60s. As shown here, PAG 1 exhibits the slowest gelation with gel formation onset only occurring after 1500s of UV exposure. An increase in complex viscosity is noted within 500s in the case of both PAG 2 and PAG 3.

The differences in gelation rate were attributed to the type of molecules being used. PAG 1 is a covalently bonded molecule and photoacid generation requires breaking of covalent bonds while PAG 2 and PAG 3, on the other hand, are both ionic and therefore react more readily to UV exposure. The chemical changes induced in each PAG by UV exposure were probed using NMR as shown in the next section.

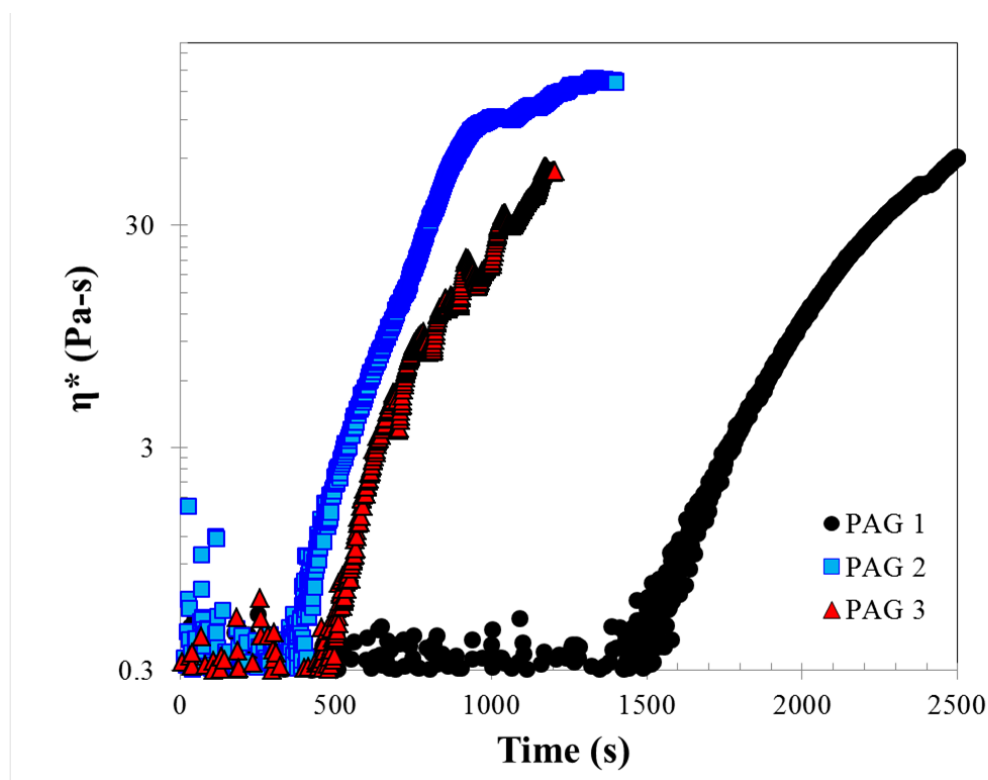


Figure 6.2 Photogelation profiles for dispersions containing of 5mM of PAG 1, 2, and 3.

The dispersions were formulated with 3wt% Laponite and 3.6wt% F127.

6.4.2 NMR results

The time dependent chemical changes were further confirmed by ^1H -NMR results as a function of known UV exposure times for each PAG component. ^{13}C -NMR spectra were also collected; however, the signal obtained for each compound, particularly after UV exposure, was found to be too weak even after 30 min of data collection for reliable measurements.

Figure 6.3 shows the changes occurring within the aromatic region of the spectra. PAG 1 exhibits an increased number of peaks after the first 120s of UV exposure indicating the formation of additional compounds. The complete disappearance of the peaks initially assigned to carbon atoms at positions a, b, d and e (

Figure 6.3) indicates a complete breakdown of the $-\text{C}-\text{I}^+-\text{C}-$ bond in the iodonium compound. The final spectrum after 1800s indicates the presence of a mixture of aromatic products consistent with prior studies on alkyl iodonium containing PAG compounds³⁵⁻³⁷.

The ^1H -NMR spectra for PAG 2 show that the peak positions and shape in the aromatic region do not change although the overall peak intensity decreases by almost 50% after the initial 120s of UV exposure. PAG 3 also exhibits a decrease in the intensity within the aromatic regions as well as the appearance of new peak at $\delta= 6.75\text{ppm}$ and $\delta= 7.4\text{ppm}$ corresponding to incomplete photolysis of $-\text{C}-\text{I}^+-\text{C}-$ bonds and formation of new products. The intensity decrease in both cases indicates a likely decrease in concentration of the

moieties responsible for these peak positions consistent with chemical changes occurring when the sample is exposed to UV ³⁸.

In addition to the NMR from the aromatic region, Figure 6.4 shows the ¹H-NMR data corresponding to aliphatic and sulfur regions ($\delta= 3.0-4.5\text{ppm}$) in PAG 2 and PAG 3. In both cases, significant changes were observed in this spectral region consistent with prior reports on similar PAG compounds ^{35, 36}. These were caused by UV induced changes in the triflate (CF_3SO_3^-) component.

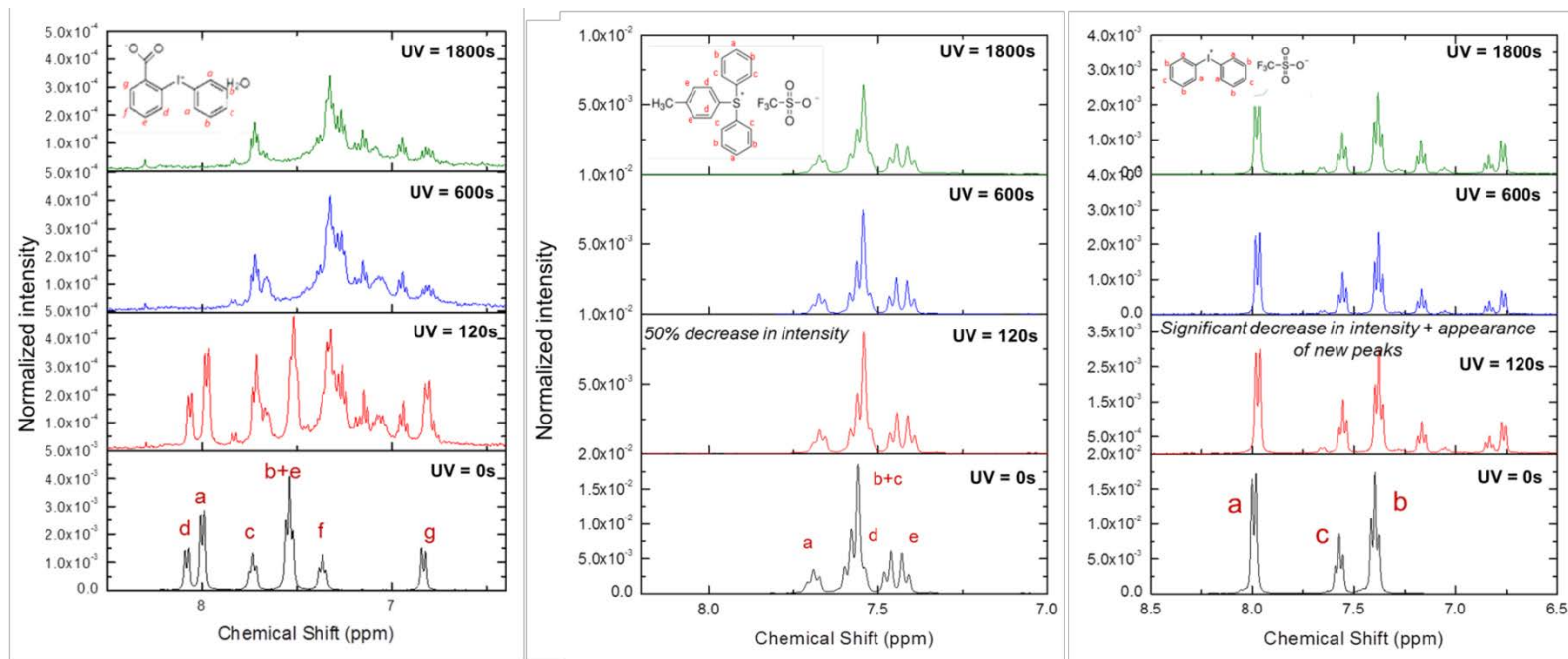


Figure 6.3 $^1\text{H-NMR}$ aromatic region as a function of UV exposure time for 5mM PAG in D_2O . The graphs are shown for the aromatic carbon region PAG 1(left), PAG 2(middle), and PAG 3(right).

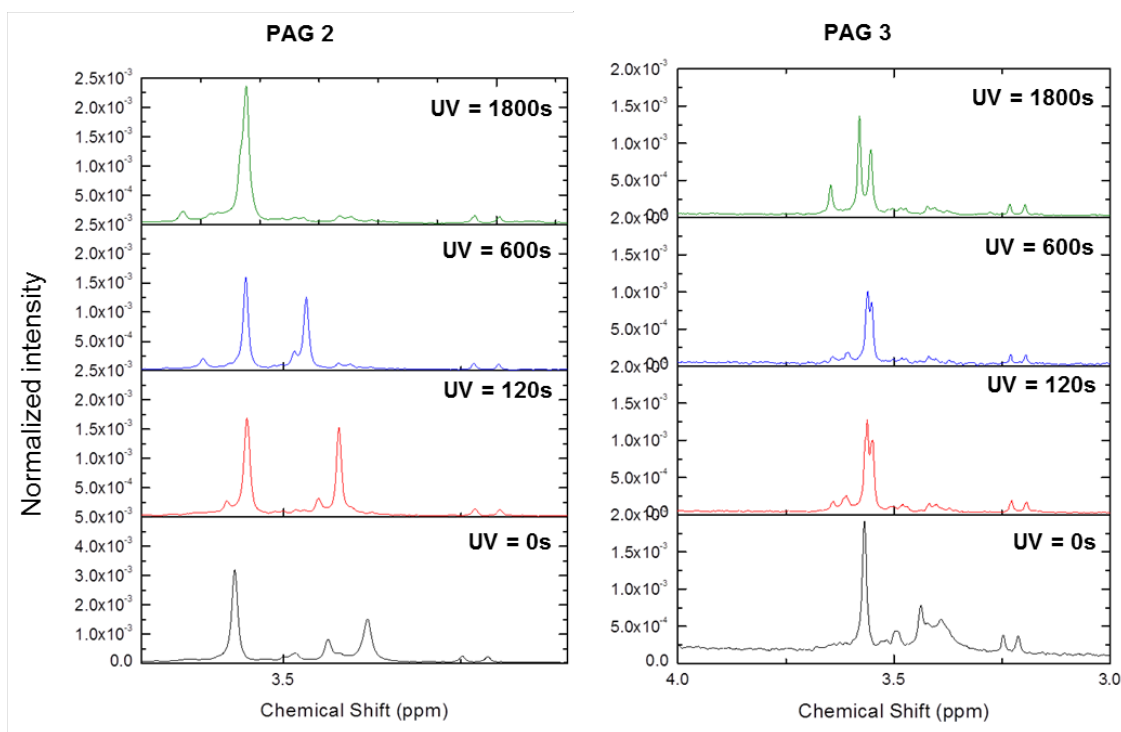


Figure 6.4 $^1\text{H-NMR}$ aliphatic and sulfur regions for 5mM PAG 2 and PAG 3 in D_2O .

The graphs show the low chemical shift region corresponding in this case to changes in the triflate component. No changes are seen in this region of the spectrum for PAG 1 (not shown).

In all 3 cases, UV irradiation causes significant breakdown of the chemical structure. In the aromatic region, PAG 1 continued changing throughout more than 600s of UV exposure while PAG 2 and PAG 3 exhibited the most changes within the first 120s of irradiation but remained unchanged afterwards. In the aliphatic and sulfur portion of the spectra, interestingly, the reaction appears to occur in two stages. The first stage with produces a dramatic change in peak positions was observed within 120s of UV exposure. As irradiation continued, the samples retained their chemical structure until the 600s-1800s. However, due to the complicated nature of the spectra shown here, these moieties contributing to these changes could not be identified conclusively.

6.4.3 Microstructure changes

Lyophilized samples with the different PAGs were imaged both before and after UV exposure to determine potential changes in the microstructure as a result of

photogelation. As already described in Chapter 5, SEM images for samples containing PAG 1 (Figure 6.5 B1-B3) exhibits a random structure with little to no organization in the liquid state; the gel state (C1-C3) produced after UV irradiation on the other hand was found to have a well ordered layered structure with interconnected pores.

UV irradiation and changing from a liquid to a gel did not produce significant changes in the microstructure of samples containing PAG 2 and PAG 3 as shown in Figure 6.6 and Figure 6.7 respectively. The dispersion formulated with 5mM of PAG 2 had a layered microstructure both before and after UV exposure with no evidence of pores (Figure 6.6) while dispersions containing 5mM PAG 3, on the other hand, displayed a 3D structure with a well-ordered array of pores (Figure 6.7 (b) and (e)). These pores were found to be non-uniform with sizes ranging up to several microns in diameter.

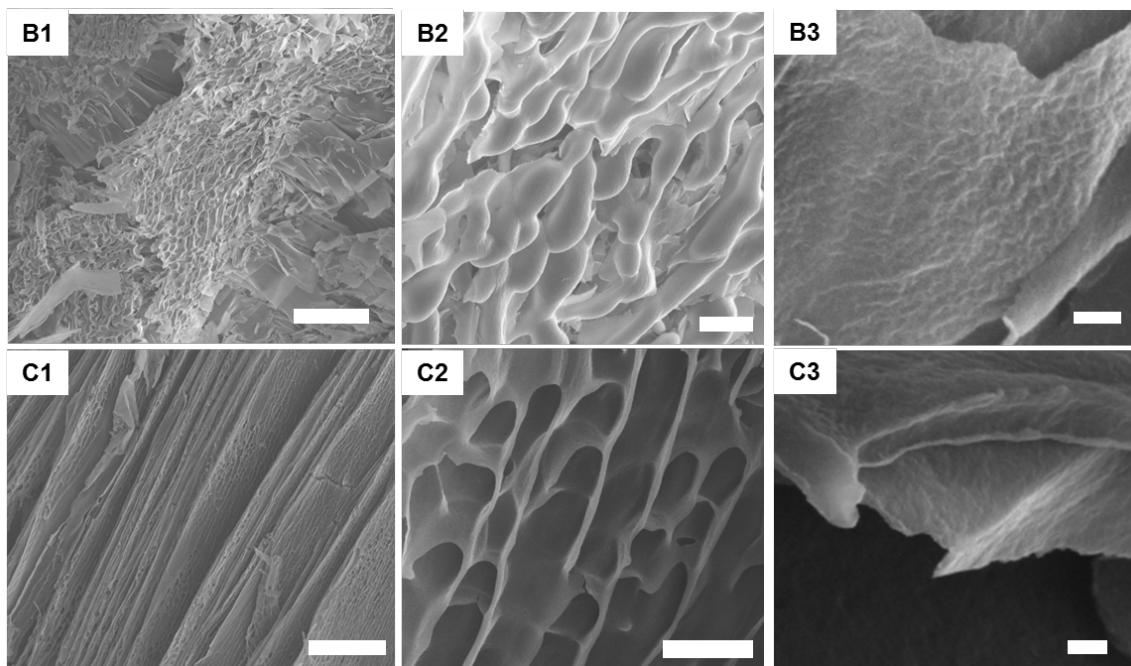


Figure 6.5 SEM images of lyophilized samples with 3wt% Laponite, 3.6wt% F127 and 5mM PAG 1.

Adapted from Figure 5.10. B1-B3 = PAG 1 before UV irradiation; C1-C3: PAG 1 after UV irradiation.

Scale bars Column 1= 50µm, Column 2= 5µm and Column 3= 400nm

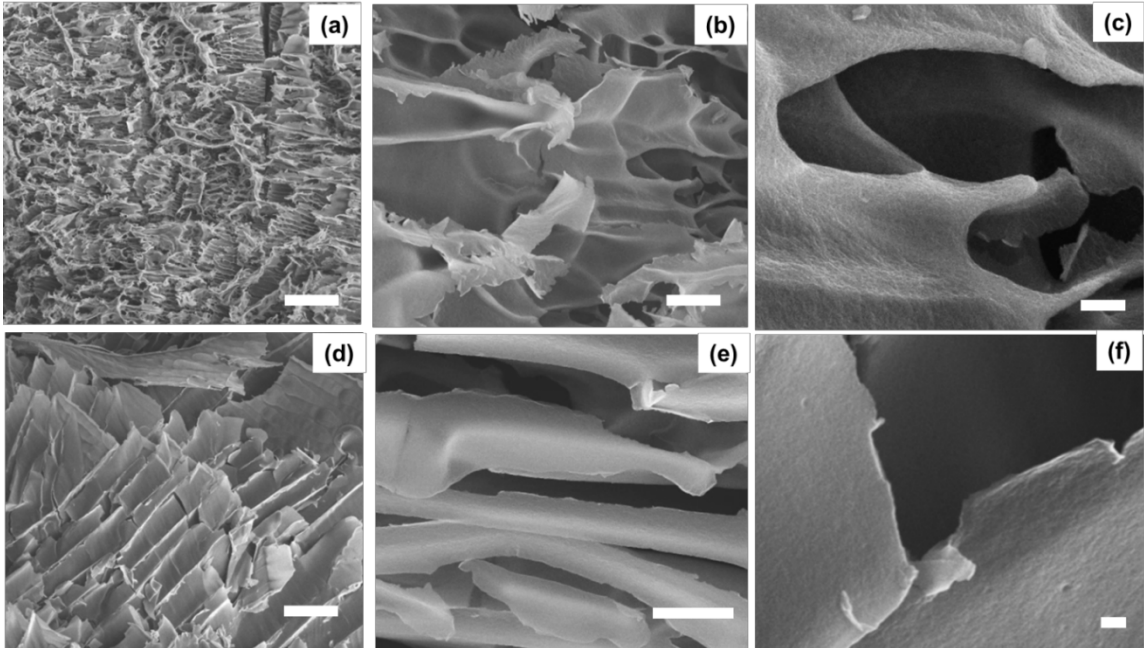


Figure 6.6 SEM images obtained 3wt% Laponite, 3.6wt% F127 and 5mM PAG 2.

Samples shown were lyophilized before UV exposure (top row) and after photogelling by UV exposure (bottom row). Scale bars shown: (a) and (d) = 50µm, (b) and (e) = 5µm and (c) and (f) 1µm.

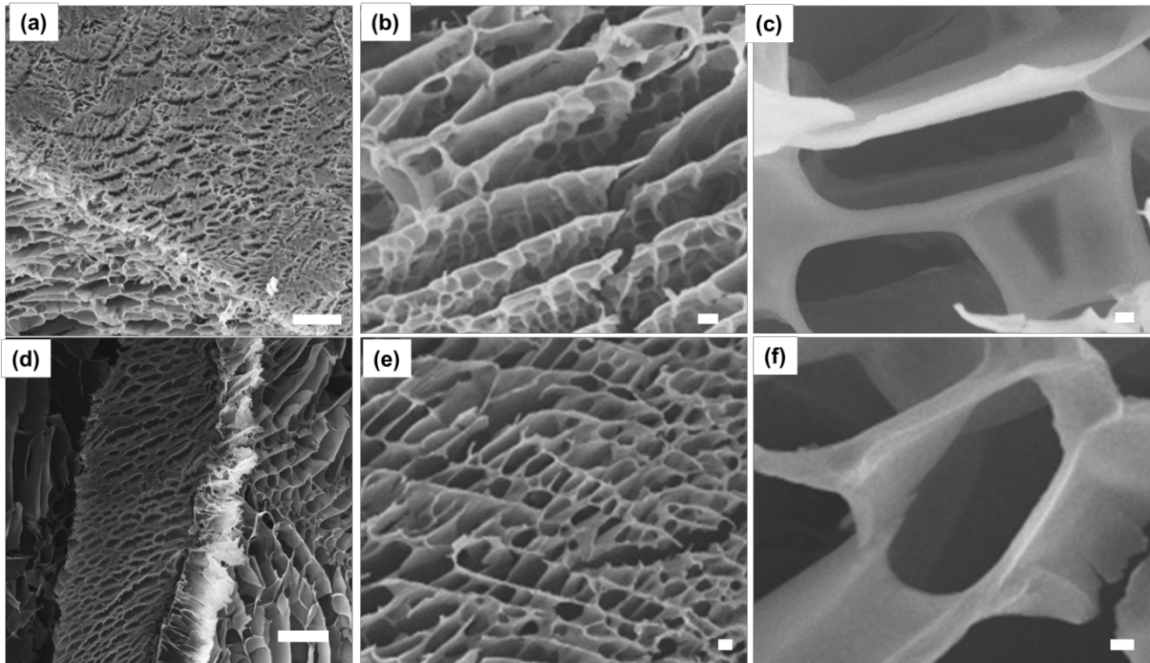


Figure 6.7 SEM images 3wt% Laponite, 3.6wt% F127 and 5mM PAG 3.

Samples shown were lyophilized before UV exposure (top row) and after photogelling by UV exposure (bottom row). Scale bars shown: (a) and (d) = 50µm, (b) and (e) = 5µm and (c) and (f) 1µm.

From the photorheology and SEM images, it is apparent that simply changing the PAG type not only changes the rates for UV gelation but also results in significantly different microstructures. However the microstructure of the lyophilized samples provides no information on the clustering and organization of the Laponite nanoparticles with the bulk material. Instead, time resolved simultaneous UV-SAXS experiments were used to follow the dynamic structural changes during UV exposure.

6.4.4 Time resolved simultaneous UV-SAXS

Time resolved simultaneous UV-SAXS measurements were conducted to determine the effect of UV on the structure during photogelation. In all cases, several spectra were first collected without UV to obtain a baseline of the initial particle arrangement. UV onset time was noted and SAXS spectra collected continuously until no further changes were observed (typically ~1500s) at a rate of 6 frames per minute. Time resolved UV-SAXS data for each of the 3 PAGs are shown in Figure 6.8 and Figure 6.9.

Figure 6.8 (a), (c) and (e) depict 3D plots of the time resolved SAXS obtained over the entire accessible q -range for PAGs 1, 2 and 3 respectively while Figure 6.8 (b), (d) and (f) shows the corresponding $I(q)$ vs. q overlay plots. The dotted arrow in each case points to a peak that appears in the high q region and centered at $q \sim 3.2\text{nm}^{-1}$. This peak is consistent with recently reported values for temperature triggered self-assembly of Laponite/Pluronic systems reported by Boucenna *et al.*³⁹. They report a similar peak position in contrast matched SANS data normalized by the Laponite form factor and attribute this to strong inter-particle interactions. Using a similar treatment, the Laponite concentration effect can be determined using

$$\phi = t \frac{q_{peak}}{2\pi} \quad (6.1)$$

where ϕ is the local effective volume fraction of Laponite disks with thickness, t .

Assuming single platelets of thickness 0.9nm, this yields a volume fraction $\phi \sim 0.046$, which in turn corresponds to a local Laponite concentration on the order of 15wt%, a value much larger than the average concentration of 3wt%. Since the SEM images show a network with large empty areas, the higher value determined for ϕ is consistent with larger Laponite concentration due to particles located primarily within the network while the majority of the space contains water.

The insets within the $I(q)$ vs. q plots indicate the changes occurring in the low q region of $0.09\text{-}0.25\text{nm}^{-1}$. The arrow indicates the variation of the scattering intensity $I(q)$ from $t = 0\text{s}$ to $t=1500\text{s}$. The change in scattering intensity is attributed to large scale structure and ordering expected as Laponite gels are formed^{12, 34, 40-44} similar to the thermal gelation process described in Chapter 5.

The surface plot shown in Figure 6.9 illustrates the intensity variation as a function of time and scattering vector q . The onset of UV irradiation is shown by the dotted line while the contour lines are meant as a guide when viewing the intensity changes. As shown here, the most significant change occurs in the low q region. Each PAG used had scattering intensity changes occurring after different times of UV exposure. Since the scattering intensity corresponds to the structural arrangement in the system, this indicates that re-structuring occurs at different times and rates depending on the PAG used. This structural rearrangement will be discussed in more detail in the following section.

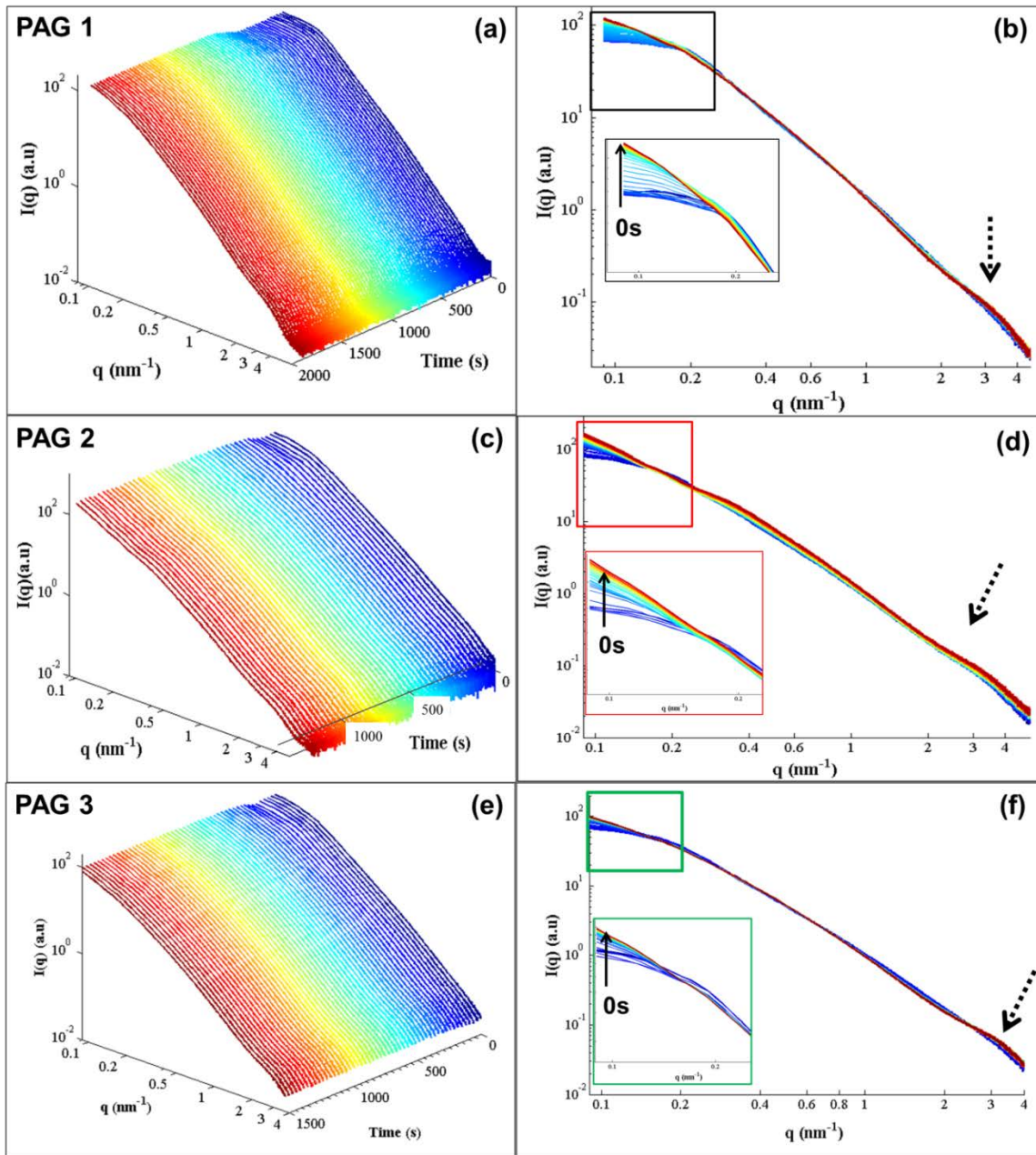


Figure 6.8 Time resolved SAXS for 3.6wt% F127 with 3wt% Laponite and 5mM PAG.

The different PAGs used are shown in separate images. PAG 1 = (a) and (b); PAG2 = (c) and (d) and PAG 3 = (e) and (f). Graphs (a), (c) and (e) represent 3D plots of the time dependent change in the scattering spectra while (b), (d) and (f) show a 2D overlay plot. The inset in each case highlights changes in slope in the low q region of $0.09\text{-}0.25\text{nm}^{-1}$

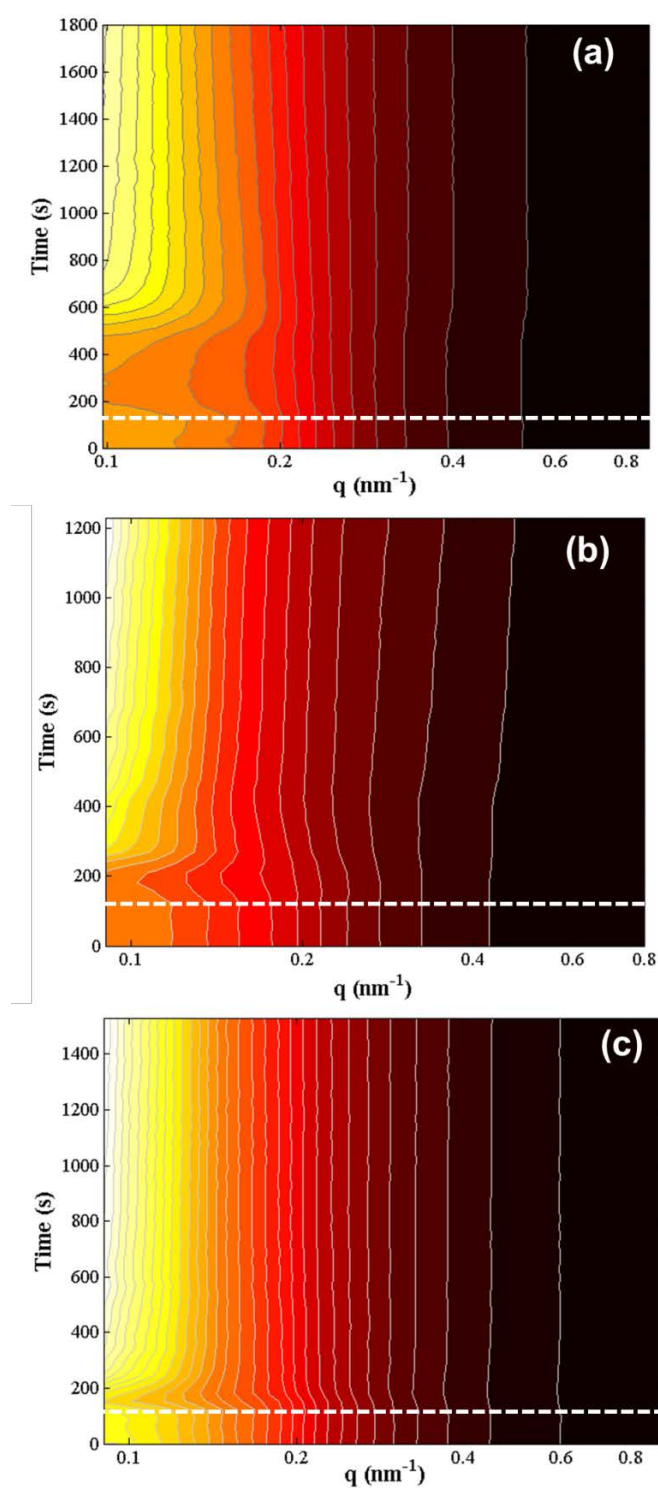


Figure 6.9 Surface plot of time resolved data showing intensity variation.

Graphs show data for samples containing 3wt% Laponite, 3.6wt% F127 and 5mM of PAG 1 (a), PAG 2 (b) and PAG 3 (c). In each case the contour lines are included as a guide to the eye. In each case, the dotted line represents the time at which UV irradiation was started.

6.4.5 Structural rearrangement and bulk gelation

The UV-SAXS data shows time dependent changes at low q while photorheology indicates that the bulk properties of the dispersions change from a liquid to that of a gel. Since structure and bulk properties are related to each other, the changes measured from UV-SAXS can be related to bulk changes. The following section looks at correlating the time scale at which the structural rearrangement occurs to the formation of a bulk gel measured in these dispersions.

Since the formulations used contained 3wt% Laponite, the particles are expected to interact with each other as described previously in Chapters 4 and 5. To determine and quantify these interactions, the structural changes were determined by plotting an analogue representation of the structure factor, $S(q)_{exp}$, described in Chapter 4. Instead, a Lorentz-corrected plot of $I(q).q^2$ as a function of q , consistent with prior reports by Paineau *et al.*⁴⁵ for a series of natural clays, was derived for each PAG and used to determine the structure evolution with UV exposure.

The 3D time resolved data for PAGs 1, 2 and 3 and corresponding 2D plots are shown in Figure 6.10. The peak observed at low q -vector is attributed to the characteristic structural spacing of the scattering particle clusters. The surface plots in Figure 6.11 further show the intensity distribution and the differences in structural arrangement with the different PAGs present in the system. In each case, the peak exhibits a significant dependence on the UV irradiation time.

A significant change in both the peak intensity and peak shape occurs as UV irradiation takes place. For all three PAGs, prior to UV exposure as well as during the early stages, the Lorentz-corrected plot shows a sharp structure factor peak. As UV irradiation takes place, the peak intensity initially decreases followed by peak broadening. This is subsequently followed by a shift in the peak position and further broadening, a behavior characteristic of glassy structures where clusters are unable to rearrange themselves but are instead at fixed positions¹⁸⁻²⁰. The peak intensity for dispersions containing PAG 2

increases after the initial peak shift to higher q . In the case of PAGs 1 and 3, an overall decrease in peak intensity was also noted.

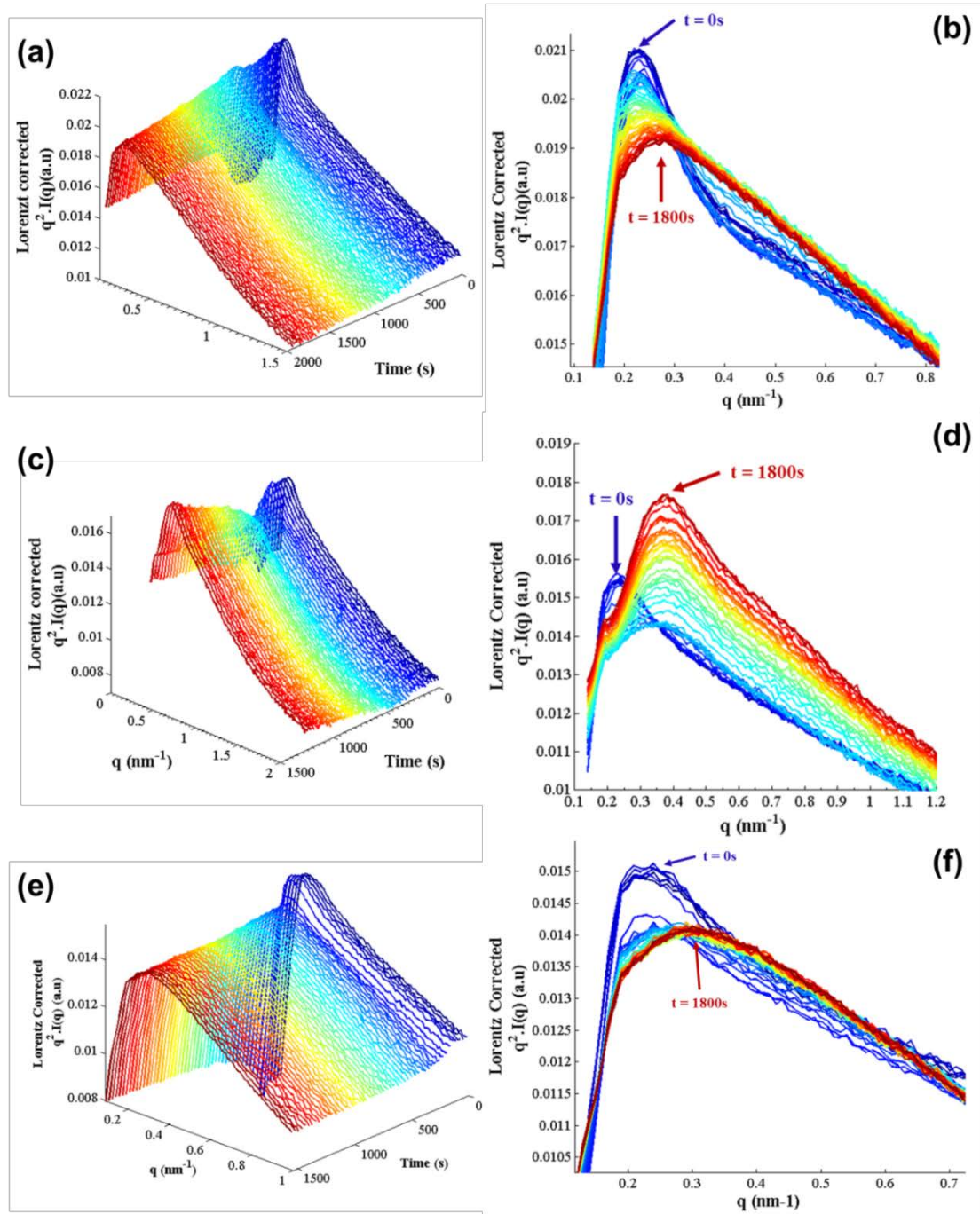
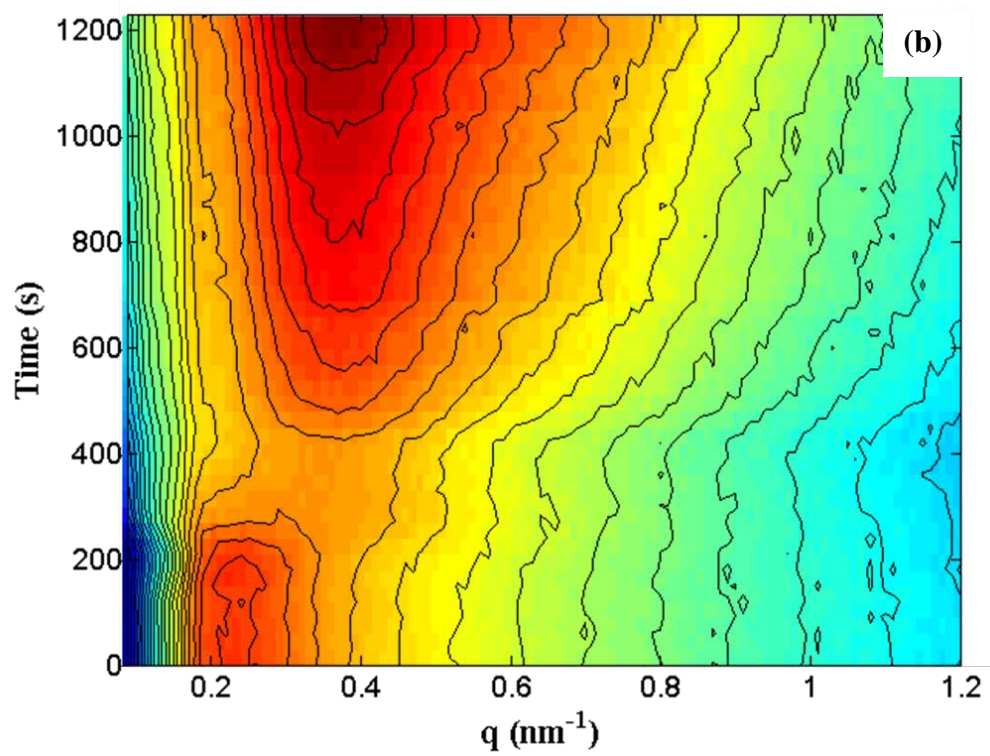
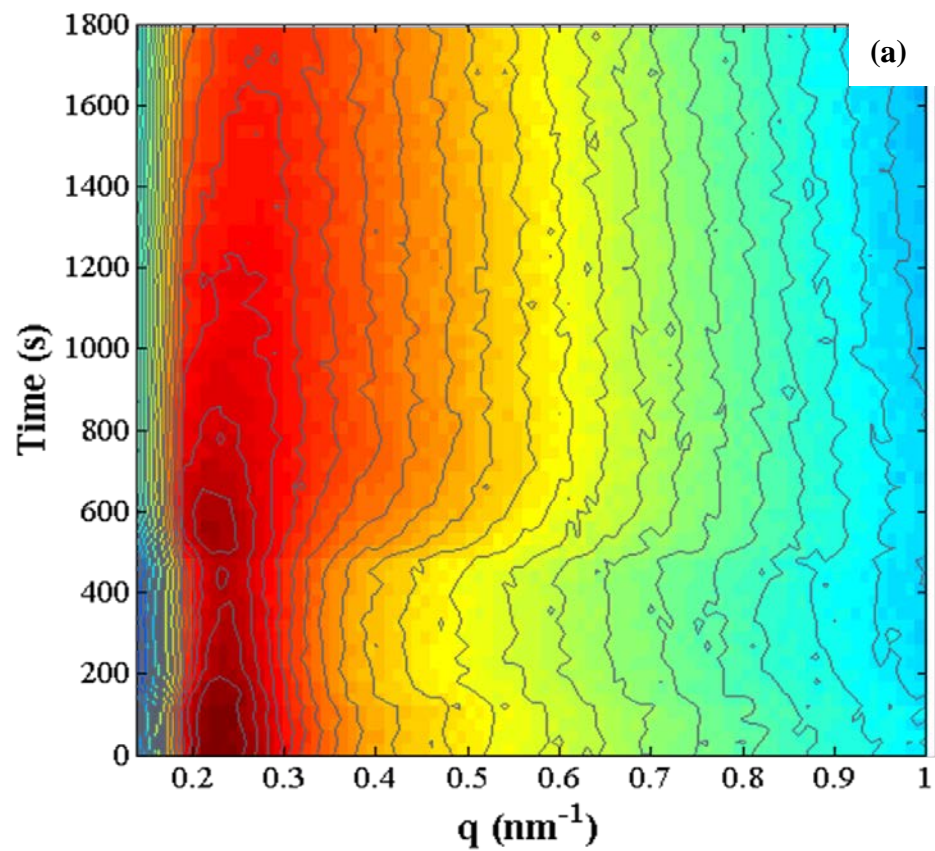


Figure 6.10 3D and 2D Lorentz corrected plots for time resolved UV-SAXS results.

All samples were formulated with 3.6wt% F127, 3wt% Laponite and 5mM of PAGs 1((a) and (b)), 2((c) and (d)) and 3((e) and (f)). The arrows in (b), (d) and (f) show the peak position before ($t=0s$) and after ($t=1800s$) UV exposure. UV irradiation was started after the first 60s in each case.



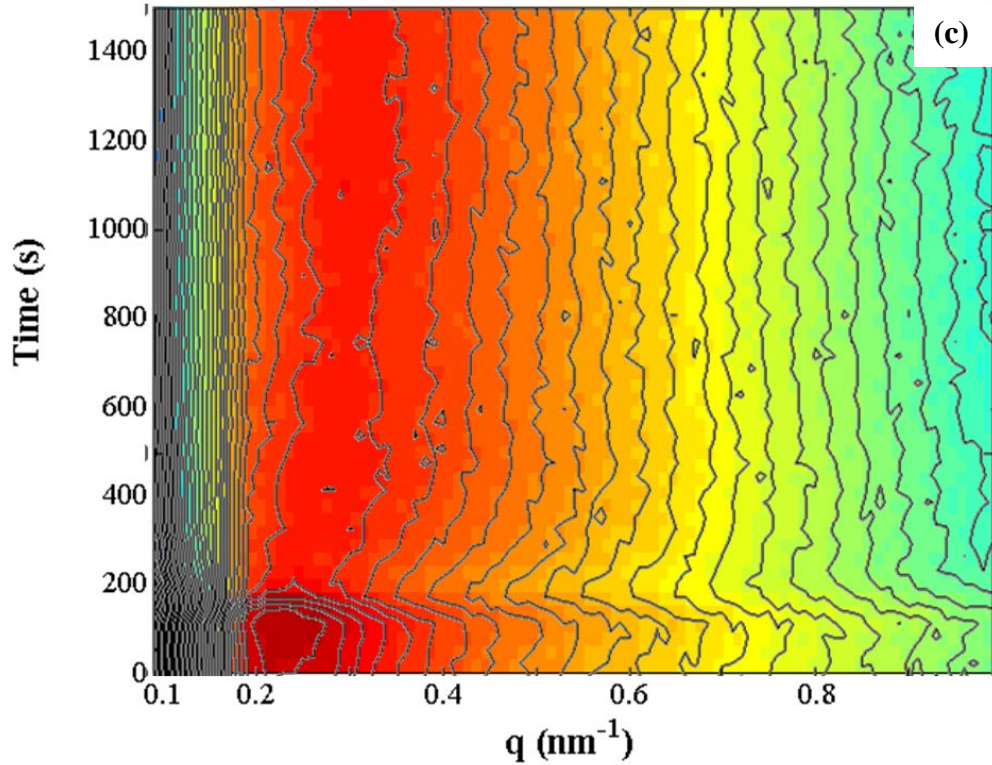


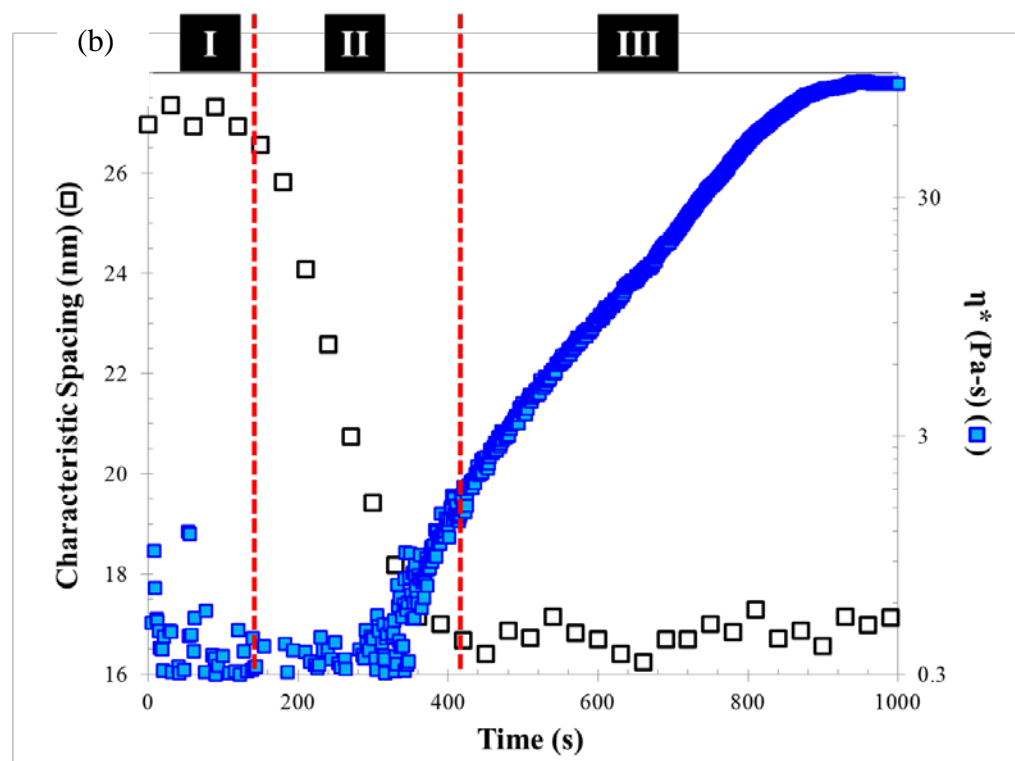
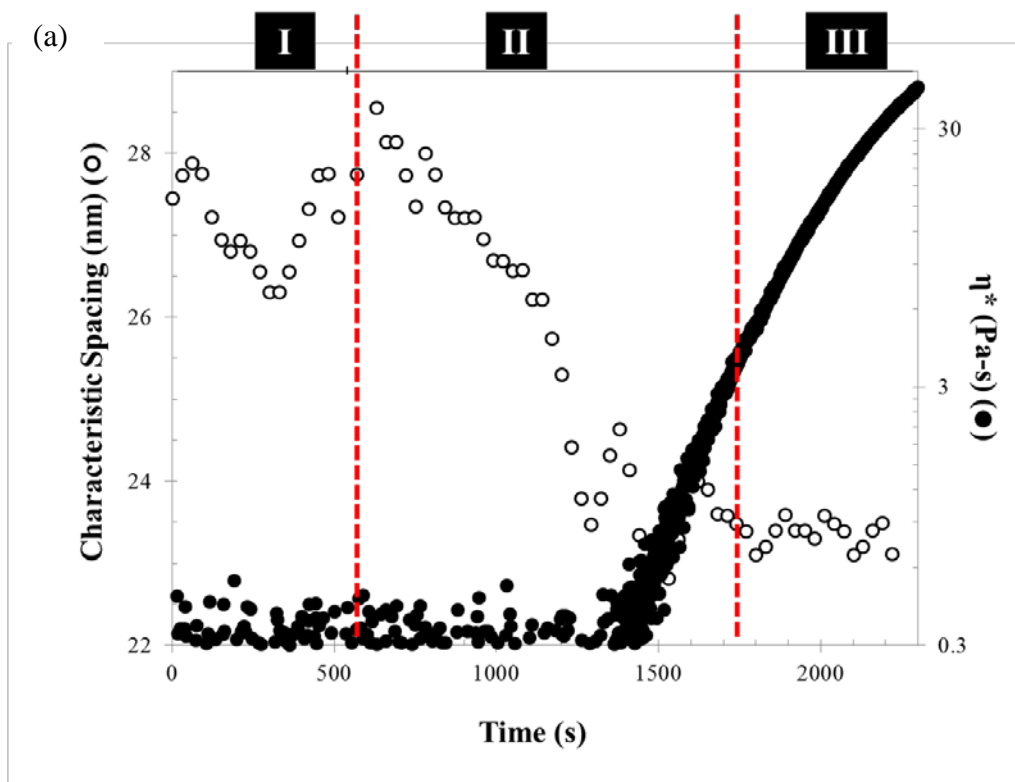
Figure 6.11 Contour plot illustrating time dependent changes in Lorentz corrected data.

Results were obtained for 5mM (a) PAG 1, (b) PAG 2 and (c) PAG 3. UV irradiation was initiated at 60s in each case.

The peak position, q_{peak} , in the Lorentz-corrected plot is related to the characteristic cluster spacing, D^* , by

$$D^* = \frac{2\pi}{q_{peak}} \quad (6.2)$$

Since the peak position varies with time of UV irradiation, the corresponding UV time-dependent D^* for each PAG can be calculated using a Gaussian fit to determine the value of q_{peak} for each SAXS spectrum. Finally, to relate the time dependent changes in D^* and complex viscosity were compared. Figure 6.12 compares the UV irradiation time dependent changes in characteristic spacing and complex viscosity for each of the three PAGs used.



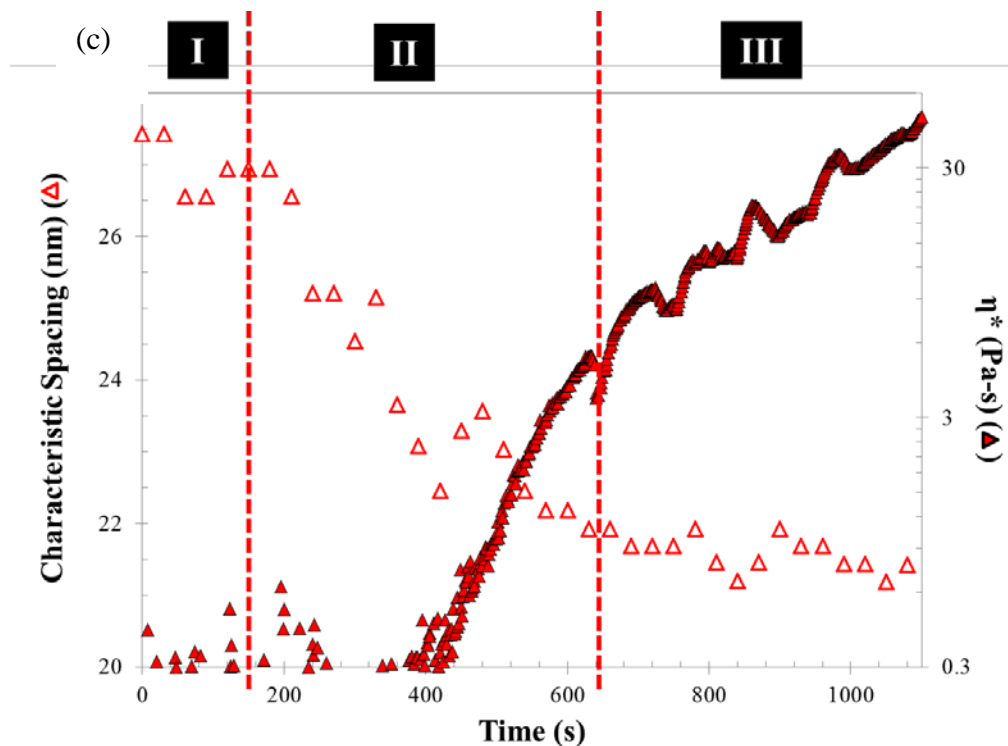


Figure 6.12 Time dependent variation in structural spacing and bulk complex viscosity

(a) PAG 1, (b) PAG 2 and (c) PAG 3. In each case, UV irradiation was initiated at $t = 60$ s.

For each type of PAG used, three distinct and different behavior regimes were noted and are described below:

- (a) **Regime I:** This regime represents the initial stage of the UV induced reaction and chemical due to photolysis induced changes in the PAGs. At this stage, the Laponite particles remain well-surrounded by the F127 shells. No re-structuring of the particles occurs at this stage and both D^* and η^* remain constant as the sample retains its liquid state.
- (b) **Regime II:** As the UV induced reaction progresses, desorption of the F127 polymer shell takes place. The particles are then able to interact with each other and can move into clusters/ aggregates closer together producing a decrease in D^* . As UV exposure continues, a corresponding rise in the complex bulk viscosity is also observed.

(c) **Regime III:** The interacting particles and clusters achieve a stable or arrested state where the spacing D^* remains fairly constant. In all cases, this final D^* value is less than the initial spacing with a decrease of 8-10nm in D^* occurring over the course of UV exposure. The viscosity continues to increase within this regime until a plateau is achieved for longer UV exposure times.

For all three PAGs used, a delay exists between the initial change in D^* and a corresponding bulk viscosity increase. Since SAXS measurements probe small scale rearrangement and clustering, we believe that the initial decrease in D^* corresponds to the nucleation of small clusters of particles. As UV exposure time increases, a larger number of clusters are formed. For the bulk properties to change, these clusters must be able to interact with each other within the material. Since the photorheology experiments typically uses a gap size on the order of 0.5mm, the delay between changes in D^* and bulk viscosity changes is then caused by the time it takes for clusters to be able to interact in the volume between the parallel plates.

6.5 Conclusions

The work presented in this chapter shows that the kinetics of gel formation depends strongly on the type of PAG used and can be easily controlled choosing a suitable molecule. The data presented clearly indicates that PAG chemistry affects gelation rates, bulk microstructure and nanoscale cluster arrangement. We also show that simultaneous UV-SAXS provides a reliable method to probe the rearrangement of clusters during UV-induced photogelation in Laponite nanoparticle gels.

Comparing the nanostructure rearrangement kinetics with the bulk UV induced gelation results, we show that there is very good agreement between the time scales for nanostructure changes and bulk complex viscosity changes. The results show 3 distinct regimes occurring during the gel formation starting with UV-induced chemical reaction during which structure does not change. This is followed by a decrease in the characteristic cluster spacing to a stable value and these changes are reflected in an

increase in the complex viscosity indicating bulk gel formation. A delay is observed between the time at which cluster spacing starts to decrease and the initial increase in complex viscosity for all three PAGs used. This decrease is consistent with the initial formation of non-interacting clusters during which viscosity remains constant. As clusters begin interacting, the viscosity starts to rise until frozen or arrested clusters lead to a bulk gel network.

This approach of combining multi-scale characterization methods to obtain new insight and understand how structure relates to bulk properties in dispersions can be applied to other systems where bulk changes depend on structural organization. These experiments provide a unique way of correlating the changes occurring at two very different scales.

6.6 References

- (1) Whitesides, G. M.; Grzybowski, B. *Science* **2002**, *295*, 2418-2421.
- (2) Nie, Z.; Petukhova, A.; Kumacheva, E. *Nat. Nanotechnol.* **2009**, *5*, 15-25.
- (3) Liu, K.; Zhao, N.; Kumacheva, E. *Chem. Soc. Rev.* **2011**, *40*, 656-671.
- (4) Glotzer, S. C.; Solomon, M. J. *Nat. Mater.* **2007**, *6*, 557-562.
- (5) Grzelczak, M.; Vermant, J.; Furst, E. M.; Liz-Marzán, L. M. *ACS Nano* **2010**, *4*, 3591-3605.
- (6) Ruzicka, B.; Zaccarelli, E.; Zulian, L.; Angelini, R.; Sztucki, M.; Narayanan, T.; Sciortino, F.; Ruocco, G. *Nat. Materials*, **2011**, *10*, 56-60
- (7) Ruzicka, B.; Zulian, L.; Zaccarelli, E.; Angelini, R.; Sztucki, M.; Moussaïd, A.; Ruocco, G. *Phys. Rev. Lett.* **2010**, *104*.
- (8) Li, L.; Harnau, L.; Rosenfeldt, S.; Ballauff, M. *Phys. Rev.* **2005**, *72*.
- (9) Cavallaro, G.; Lazzara, G.; Milioto, S. *Soft Matter* **2012**, *8*, 3627-3633.
- (10) Shikinaka, K.; Aizawa, K.; Murakami, Y.; Osada, Y.; Tokita, M.; Watanabe, J.; Shigehara, K. *J. Colloid Interface Sci.* **2012**, *369*, 470-476.
- (11) Cummins, H. Z. *J. Non-Crystalline Solids* **2007**, *353*, 3891-3905.
- (12) Mourchid, A.; Levitz, P. *Phys. Rev.* 1998, *57*.
- (13) Tang, X.; Alavi, S. Structure and Physical Properties of Starch/Poly Vinyl Alcohol/Laponite RD Nanocomposite Films. *J. Agric. Food Chem.* **2012**, *60*.
- (14) Loiseau, A.; Tassin, J.-F. *Macromolecules* **2006**, *39*.
- (15) Cousin, F.; Cabuil, V.; Levitz, P. Magnetic Colloidal Particles as Probes for the Determination of the Structure of Laponite Suspensions. *Langmuir* **2002**, *18*.
- (16) Sun, K.; Raghavan, S. R. *Langmuir* **2010**, *26*, 8015-8020.
- (17) Shan, D.; Han, E.; Xue, H.; Cosnier, S. *Biomacromolecules* **2007**, *8*.
- (18) Tanaka, H.; Jabbari-Farouji, S.; Meunier, J.; Bonn, D. *Phys. Rev.* **2005**, *71*.
- (19) Tanaka, H.; Meunier, J.; Bonn, D. *Phys. Rev.* **2004**, *69*.
- (20) Bonn, D.; Kellay, H.; Tanaka, H.; Wegdam, G.; Meunier, J. *Langmuir* **1999**, *15*.
- (21) Ruzicka, B.; Zaccarelli, E. *Soft Matter* **2011**, *7*, 1268-1286.
- (22) Labanda, J.; SabatÃ©, J.; Llorens, J. *Colloids Surfaces A: Physicochem. Eng. Asp.* **2007**, *301*, 8-15.
- (23) King Jr, H. E.; Milner, S. T.; Lin, M. Y.; Singh, J. P.; Mason, T. G. *Phys. Rev. E.* **2007**, *75*.
- (24) Durmus, A.; Kasgoz, A.; Macosko, C. W. *Polymer* **2007**, *48*, 4492-4502.
- (25) Bhatia, S.; Barker, J.; Mourchid, A. *Langmuir* **2003**, *19*, 532-535.
- (26) Mourchid, A.; Delville, A.; Lambard, J.; LeColier, E.; Levitz, P. *Langmuir* **1995**, *11*.
- (27) Nelson, A.; Cosgrove, T. *Langmuir* **2005**, *21*, 9176-82.
- (28) Nelson, A.; Cosgrove, T. *Langmuir* **2004**, *20*, 10382-8.
- (29) Nelson, A.; Cosgrove, T. *Langmuir* **2004**, *20*, 2298-304.
- (30) Schmidt, G.; Nakatani, A. I.; Butler, P. D.; Karim, A.; Han, C. C. *Macromolecules* **2000**, *33*, 7219-7222.
- (31) Baghdadi, H. A.; Jensen, E. C.; Easwar, N.; Bhatia, S. R. *Rheol. Acta* **2008**, *47*, 121-127.
- (32) Majumdar, D.; Blanton, T. N.; Schwark, D. W. *Appl. Clay Sci.* **2003**, *23*, 265-273.

- (33) Sun, K.; Kumar, R.; Falvey, D. E.; Raghavan, S. R. *J. Am. Chem. Soc.* **2009**, *131*, 7135-7141.
- (34) Ruzicka, B.; Zaccarelli, E.; Zulian, L.; Angelini, R.; Sztucki, M.; Moussaïd, A.; Narayanan, T.; Sciortino, F. *Nat. Mater.* **2010**, *10*, 56-60.
- (35) Ichimura, K. *J. Mater. Chem.* **2007**, *17*, 632-641.
- (36) Shirai, M.; Tsunooka, M. *Bull. Chem. Soc. Jpn.* **1998**, *71*, 2483-2507.
- (37) Devoe, R. J.; Sahyun, M. R. V.; Serpone, N.; Sharma, D. K. *Can. J. Chem.* **1987**, *65*, 2342-2349.
- (38) Günter, H. N. M. *R.nmR Spectrosc. Basic Princ. concepts, Appl. Chem.* **1995**.
- (39) Boucenna, I.; Guedeau-Boudeville, M.-A.; Lapp, A.; Colinart, P.; Proag, A.; Royon, L.; Mourchid, A. *Soft Matter* **2013**, *9*, 170-176.
- (40) Ramsay, J. D. F.; Wing, G. J. *Colloid Interface Sci.* **1991**, *141*, 475-485.
- (41) Jabbari-Farouji, S.; Wegdam, G. H.; Bonn, D. *Phys. Rev. Lett.* **2007**, *99*.
- (42) Nicolai, T.; Cocard, S. *Eur. Phys. J. E: Soft Matter Biol. Phys.* **2001**, *5*, 221-227.
- (43) Loizou, E.; Butler, P.; Porcar, L.; Kesselman, E.; Talmon, Y.; Dundigalla, A.; Schmidt, G. *Macromolecules* **2005**, *38*, 2047-2049.
- (44) Ruzicka, B.; Zulian, L.; Ruocco, G. *Phys. Rev. Lett.* **2004**, *93*.
- (45) Paineau, E.; Bihannic, I.; Baravian, C.; Philippe, A.-M.; Davidson, P.; Levitz, P.; Funari, S. S.; Rochas, C.; Michot, L. J. *Langmuir* **2011**, *27*.

CHAPTER 7

7. Summary and Future Work

7.1. Thesis Summary

In this work, I have presented a detailed study of aqueous dispersions of Laponite and the effect of adding a triblock thermoresponsive surfactant, Pluronic F127, to these dispersions. I have demonstrated that the presence of even small amounts of F127 can have a significant effect on the gel forming ability of these Laponite dispersions. From the initial work conducted at room temperature, the thermal response of the dispersions was also measured and the results presented clearly show the ability of F127 to induce gel formation with increasing temperature. Finally, by simply adding a chemically reactive component to the Laponite/F127 dispersions, the results presented clearly show light induced sol-gel transitions.

A large portion of the work presented has demonstrated the use of SAXS to quantify particle-polymer interactions and particle structure despite the lack of long range order and Bragg peaks in the scattering spectra of Laponite containing samples. While the inability to contrast match scattering contributions in SAXS, the analysis methods described here have demonstrated by designing the experiments such that the scattering contributions from one of the components can be removed or neglected, a detailed analysis of the changes occurring can be conducted. In particular, this is the first demonstration and quantification of the temperature induced changes in the F127 shell adsorbed on the surface of Laponite particles as discussed in Chapter 4.

The last portion of this work is the only simultaneous UV-SAXS work that we are aware of probing structural re-arrangement and kinetics as a result UV induced chemical reactions and subsequent self-assembly. This work demonstrates that SAXS is an ideal

method to determine structure and organization kinetics in nanoparticle suspensions when the appropriate data treatment methods are used. The results of these time resolved experiments have finally allowed us to quantify and relate the structural changes with the macroscale behavior and gelation kinetics determined by UV-rheology.

7.2. Future Directions

As a pioneering study into the dynamic restructuring in Laponite gels and correlation to macroscopic properties, this work opens the door to a new design space and analysis that is yet to be studied in the areas of colloids and self-assembly particularly in responsive systems. Obvious steps moving forward include probing the behavior or other commercially relevant dispersions particular those that are known to exhibit additional functionalities. Easy systems to study induced structuring with include magnetic nanoparticles and platelets while other UV active particles include a variety of other oxide materials (ZnO, TiO₂, Ceria to name a few).

In the case of the current Laponite / F127 aqueous dispersion, the changes in the 3D lyophilized microstructure as well as the drop cast films merit further investigation. The potential ability to tune these structures show promise for applications as active films or coatings as well as 3D scaffolds or templates for future applications.

Finally, the new insight into the structural organization and kinetics also yields a framework for probing possible applications including potential use of these Laponite/F127 gels in applications where tunable viscosity is desirable. These include targeted drug delivery systems where the sol can be delivered to the desired location. This could then be followed by UV irradiation to form a gel that stays at the desired spot slowly releasing a particular drug incorporated in the formulation.